Applying KPFM on all solid-state battery interfaces research

Dissertation

zur Erlangung des Grades
„Doktor der Naturwissenschaften“
im Promotionsfach Chemie

am Fachbereich Chemie, Pharmazie, Geographie und Geowissenschaften
der Johannes Gutenberg-Universität Mainz

von
Chao Zhu
geboren in Jiangsu, China
Mainz, March 2023

Die vorliegende Arbeit wurde in der Zeit von Oktober 2018 bis März 2023 am

Max Planck Institut fur Polymerforschung angefertigt.

Mainz, März 2023

Erster Berichterstatter:

Zweiter Berichterstatter:

Tag der mündlichen Prüfung:

Declaration

I hereby declare that I wrote the dissertation submitted without any unauthorized external assistance and used only sources acknowledged in the work. All textual passages which are appropriated verbatim or paraphrased from published and unpublished texts as well as all information obtained from oral sources are duly indicated and listed in accordance with bibliographical rules. In carrying out this research, I complied with the rules of standard scientific practice as formulated in the statutes of the Johannes Gutenberg University Mainz to ensure standard scientific practice.

Chao Zhu, Mainz

Acknowledgements

Abstract

All-solid-state batteries as potential next generation batteries are attracting increasingly more attention. Compared to liquid electrolyte-based lithium-ion batteries, all-solid-state batteries have obvious advantages, including non-flammability and higher energy density. However, the complex interfacial problems in all-solid-state batteries limit their further applications. Among different kinds of interfacial problems, the most challenging ones are lithium dendrites originating from anode lithium electrode – solid electrolyte interface, grain boundaries in solid electrolytes, and space charge layers at electrode – solid electrolyte interfaces. The former leads to short-circuiting of batteries while the latter adds interfacial resistance. More importantly, compared to other interfacial problems, those two problems are less studied because of a lack of suitable methods. In recent years, the development of Kelvin probe force microscopy (KPFM), which is a non-destructive technology with high spatial resolution, has provided us with new possibilities to study those interfacial problems. Using KPFM, I compare changes in measured contact potential difference (CPD) in batteries under different working condition. In my PhD thesis, I apply advanced operando KPFM to track the origin of those interfacial problems in all-solid-state batteries.

For metals and semiconductors, the CPD signal measured by KPFM and its change are known to be related to the work function and to changes in the work function of the sample locally. However, for mixed-ionic-electronic conductor (MIEC) such as solid electrolyte in all-solid-state batteries, the measured CPD signal and its changes require deeper understanding because of the existence of mobile ions and a poor electron conductivity. In Chapter 3, I theoretically outline that the measured CPD change on MIEC in a non-equilibrium state results from Galvanic (electrical) potential change. I verify this conclusion by KPFM measurements on a Hebb-Wagner cell under different polarization states.

In Chapter 4, I explore the origin of the formation of lithium dendrites at $Li_{6.25}Al_{0.25}La_3Zr_2O_{12}$ (LLZO) grain boundaries. LLZO is a solid electrolyte with a high lithium ionic conductivity. Operando KPFM reveals a drop of electrical potential at grain boundaries close to the lithium anode (negative) electrode under working conditions. I further use time-resolved

electrostatic force microscopy (tr-EFM) and electron beam irradiation on LLZO solid electrolyte. Those results reveal that the electrical potential drop at grain boundaries results from electrons being trapped at grain boundaries. The different electric conduction property at LLZO grain boundaries compared with LLZO bulk explains the preferential lithium dendrites formation at LLZO grain boundaries.

In Chapter 5, I quantitatively reveal the role of a space charge layer on the all-solid-state battery interfacial resistance. Space charge layer can only be investigated for thin film battery with well-defined interfaces. The thin film battery consists of metallic lithium as the anode, Li_3PO_4 (LPO) as the solid electrolyte and $LiCoO_2$ (LCO) as the cathode. Operando KPFM measurements on the thin film battery cross-section show that a space charge layer only exists at the LPO|LCO interface, which changes with battery voltage. With the help of operando nuclear analysis reaction (NRA), I prove that the space charge layer evolution at LPO|LCO interface results from lithium ion gradually accumulating on the LCO side while lithium ion gradually depletes on the LPO side, with an increase in battery voltage. Finally, based on those findings and in-situ electrochemical impedance spectroscopy (EIS), I calculate that space charge layer resistance at the LPO|LCO interface has a maximum value around 33.82 – 38.29 Ω cm^2 when the battery voltage is 4.3 V, in the working voltage window of 3.0 V to 4.3 V. That accounts for approximately 80% of the whole battery interfacial resistance.

Zusammenfassung

All-Solid-State-Batterien als potenzielle Batterien der nächsten Generation finden immer mehr Beachtung. Im Vergleich zu Lithium-Ionen-Batterien auf der Basis von Flüssigelektrolyten haben Festkörperbatterien offensichtliche Vorteile, darunter die Nichtentflammbarkeit und die höhere Energiedichte. Die komplexen Grenzflächenprobleme in Festkörperbatterien schränken jedoch ihre weitere Anwendung ein. Unter den verschiedenen Arten von Grenzflächenproblemen sind die schwierigsten Lithiumdendriten, die von einer negativen Elektroden/Festelektrolyt-Grenzfläche ausgehen, Korngrenzen in Festelektrolyten und Raumladungsschichten an Elektroden/Festelektrolyt-Grenzflächen. Erstere führen zu einem leichten Kurzschluss der Batterien, während letztere einen zusätzlichen Grenzflächenwiderstand verursachen. Noch wichtiger ist, dass diese beiden Probleme im Vergleich zu anderen Grenzflächenproblemen weniger erforscht sind, weil es an geeigneten Methoden mangelt. In den letzten Jahren hat uns die Entwicklung der Kelvinsonden-Kraftmikroskopie (KPFM), einer zerstörungsfreien Technologie mit hoher räumlicher Auflösung, neue Möglichkeiten zur Untersuchung dieser Grenzflächenprobleme eröffnet. Mit Hilfe der KPFM kann ich Änderungen der gemessenen Kontaktpotenzialdifferenz (CPD) in Batterien unter verschiedenen Betriebsbedingungen vergleichen. In meiner Doktorarbeit habe ich die fortschrittliche operando KPFM angewandt, um den Ursprung dieser Grenzflächenprobleme in Festkörperbatterien zu ermitteln.

Bei Metallen und Halbleitern sind das gemessene CPD-Signal und seine Änderung durch KPFM bekanntlich mit der Arbeitsfunktion und der Änderung der Arbeitsfunktion der Probe verbunden. Bei gemischt-ionisch-elektronischen Leitern (MIEC), wie z. B. Festelektrolyten in Festkörperbatterien, bedürfen das gemessene CPD-Signal und seine Veränderung jedoch weiterer Erklärungen, da es mobile Ionen und eine schlechte elektronische Leitfähigkeit gibt. In Kapitel 3 habe ich zunächst analysiert, dass die von KPFM gemessene CPD-Änderung an MIEC in einem Nicht-Gleichgewichtszustand im Vergleich zu einem Gleichgewichtszustand zu einer Veränderung des galvanischen (elektrischen) Potenzials gegenüber der Theorie führt.

Mit KPFM-Messungen an einer Hebb-Wagner-Zelle in verschiedenen Polarisationszuständen habe ich diese Schlussfolgerung dann verifiziert.

In Kapitel 4 untersuchte ich den Ursprung der Bildung von Lithiumdendriten an $Li_{6.25}Al_{0.25}La_3Zr_2O_{12}$ (LLZO) Korngrenzen. LLZO ist eine Art Festelektrolyt mit hoher Lithium-Ionenleitfähigkeit. Mit Hilfe von operando KPFM habe ich einen Abfall des elektrischen Potenzials an Korngrenzen in der Nähe der negativen Lithiumelektrode unter Arbeitsbedingungen festgestellt. Darüber hinaus habe ich die zeitaufgelöste elektrostatische Kraftmikroskopie (tr-EFM) und Elektronenstrahlbestrahlung eingesetzt, um die Lithium-Keimbildung auf LLZO-Oberflächen zu fördern, und dabei festgestellt, dass der Abfall des elektrischen Potenzials an den Korngrenzen auf den Einschluss von Elektronen an den Korngrenzen zurückzuführen ist. Diese unterschiedliche elektrische Leitungseigenschaft an LLZO-Korngrenzen im Vergleich zum LLZO-Volumen erklärt auch die leichte Bildung von Lithiumdendriten an LLZO-Korngrenzen.

In Kapitel 5 ermittle ich quantitativ den Einfluss der Raumladungszone auf den Grenzflächenwiderstand der Festkörperbatterie. Die Raumladungszone kann nur bei Dünnschichtbatterien mit wohldefinierten Grenzflächen untersucht werden. Die von mir untersuchte Dünnschichtbatterie besteht aus metallischem Lithium als Anode, Li_3PO_4 (LPO) als Feststoffelektrolyt und $LiCoO_2$ (LCO) als Kathode. Operando-KPFM-Messungen am Querschnitt der Dünnschichtbatterie zeigten, dass eine Raumladungsschicht nur an der LPO|LCO-Grenzfläche existiert, die sich mit der Batteriespannung ändert. Mit Hilfe der Operando-Kernanalysereaktion (NRA) beweise ich, dass die Entwicklung der Raumladungsschicht an der LPO|LCO-Grenzfläche darauf zurückzuführen ist, dass sich Lithium allmählich auf der LCO-Seite anreichert, während es sich auf der LPO-Seite allmählich abbaut, wenn die Batteriespannung steigt. Auf der Grundlage dieser Erkenntnisse und der elektrochemischen Impedanzspektroskopie (EIS) vor Ort habe ich schließlich berechnet, dass der Widerstand der Raumladungsschicht an der LPO|LCO-Grenzfläche bei einer Batteriespannung von 4,3 V im Arbeitsspannungsfenster von 3,0 V bis 4,3 V einen Maximalwert von etwa 33,82 - 38,29 Ω cm2 hat, was etwa 80 % des gesamten Grenzflächenwiderstands der Batterie ausmacht.

Chapter 1 Introduction

1.1 Importance of Li-ion batteries

Rapid development of human society in the last 300 years was built on the use of large amounts of fossil and coal. On the negative side, extraction and use of fossil and coal has brought serious pollution and produced huge amounts of CO_2, which exceed the Earth's self-purification ability. As a result, many plants and animals have become extinct or are endangered. More seriously, the emitted CO_2 enhances the "greenhouse" effect, increasing the average temperature of the earth[1]. The increased temperature is melting Antarctic and Arctic glaciers, which results in an increasing sea level and eventually leads to devastating disasters for human society.

People have already realized the urgency of protecting the environment and realizing the sustainable development of human society from the end of the last century. Developing clean energy and related technologies to replace traditional fossil and coal is one of the most important topics in the whole world in the first 20 years of this century. Solar, wind and water are ideal clean energy resource[2]. However, compared with fossil and coal with high energy density, clean energy needs to be collected and then transferred into or stored as electrical energy. In this process, the large-scale storage of electricity is one of the key parts, where the industry for high energy density secondary batteries has made huge progress in the last 10 years[3-5]. The market share of electric vehicles is gradually increasing, meaning there is a trend to replace traditional vehicles. To further encourage the popularization and promotion of electric vehicles, many countries plan to forbid the production and sale of conventional vehicles in the next 10 - 20 years[6]. Now, the biggest obstacle on the promotion of electric vehicles is "range anxiety" because of the limited battery energy density, even though battery technologies have made huge progress in the last 20 years already. In summary, the development of battery-related technology is very important for sustainable development.

1.2 Development historical of Li-ion battery

The concept of the Li-ion battery was born in the 1960 – 1970's when the oil crisis forced people to look for new alternative energy sources[7]. In the year 1975, M. Stanley Whittingham in Exxon first developed the lithium (Li) battery with TiS_2 as the positive electrode and metallic Li as the negative electrode[8]. It is the first secondary Li battery in the true sense with an energy density around 2 - 3 times larger than a lead-acid battery[8,9]. However, this battery has a very poor cycling performance because of the easy formation of Li dendrites that cause internal short circuits. TiS_2 is not a suitable cathode material due to its low working voltage. In the 1980's, John B. Goodenough developed a new kind of cathode material[10]. The layer structure of $LiCoO_2$ allows Li ions to be reversibly inserted and extracted to a certain degree while keeping their structure. More importantly, $LiCoO_2$ has a much higher working voltage (> 4 V)[11]. Furthermore, John B. Goodenough found another cathode material, $LiMnO_2$[12]. Compared with $LiCoO_2$, $LiMnO_2$ is cheaper, has higher decomposition temperature, and low oxidation degree, which can effectively decrease the possibility of burning or explosion. In the year 1986, Akira Yoshino, who worked at Asahi Kasei in Japan, combined $LiCoO_2$ (cathode material), coke (anode material), and $LiClO_4$ in PC solution (electrolyte) for the first time, creating the first Li-ion secondary battery, in the modern sense. It is the cornerstone of modern Li battery[13]. The first commercial battery was launched by Sony in 1991. Since then, the concept of Li-ion batteries has been generally accepted. In 1996, John B. Goodenough and his colleague found that phosphates with an olivine structure, such as lithium iron phosphate ($LiFePO_4$), are safer than traditional cathode materials. Their resistance to high temperatures, and overcharge resistance far exceed traditional Li-ion battery cathode materials, which further promotes Li-ion battery development. From that, the foundation for the development of Li-ion batteries has been laid[14].

1.3 The current situation and future of Li-ion battery

Now batteries are used in our daily life. From smart phone to electrical vehicles, all developments based on break-through developments of battery technology in the last 30 years. From the energy density evolution of batteries in Figure 1.1, we find that the

commercial Li-ion batteries have the highest energy density of battery until now, which have volumetric energy density around 500 Wh L^{-1} and Gravimetric energy density around 250 Wh kg^{-1} [15].

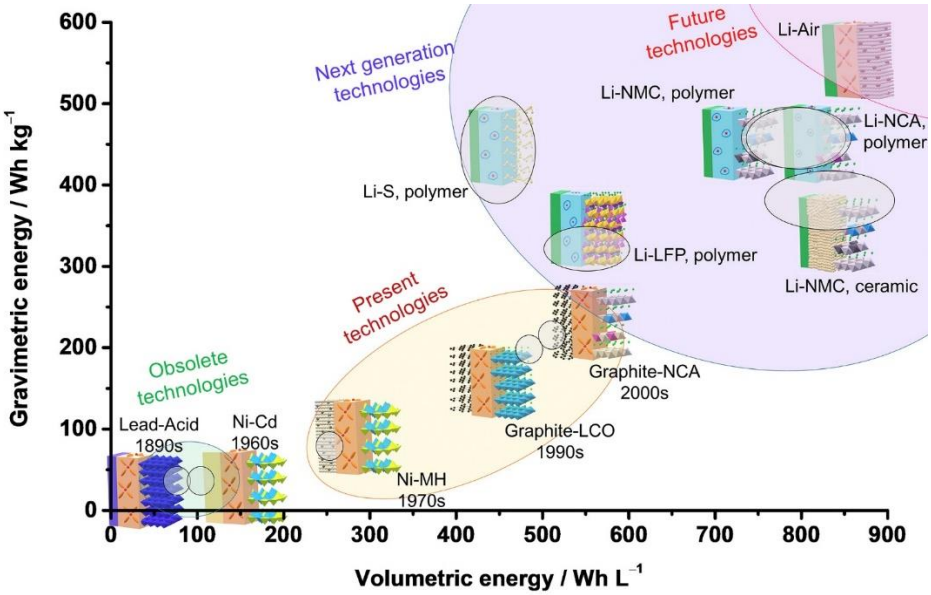

Figure 1.1 Overview of the evolution of battery energy density. Reproduced with permission. Copyright 2018, Cell Press.[15]

However, Li-ion batteries still cannot meet people's requirements because the energy density is still not high enough. Nowadays, we still need to charge our smartphone every day. Range anxiety still exists when consumers consider purchasing an electric vehicle. To mitigate that anxiety, many government-led programs have been implemented to advance battery development and increase battery energy density to around 500 Wh kg^{-1} in the next 10 years[16]. Another requirement for next-generation Li-ion batteries is safety. Today, commercial Li-ion batteries are based on organic liquid electrolytes, which can easily cause fire or explosions when over charged or due to an internal short circuit[17]. To further generalize Li-ion batteries application, safety properties must be improved.

Among the many next-generation battery candidates, all-solid-state batteries are considered the strongest contenders. On one hand, all-solid-state batteries are calculated with higher theoretical volumetric energy density and gravimetric energy density. Some kinds of all-solid-state batteries have theoretical volumetric energy density even around 900 Wh L^{-1} and the

gravimetric energy density can reach to 500 Wh kg^{-1} [15]. In general, the application of all-solid-state battery can greatly improve energy density compared with commercial Li-ion batteries we are using now. On the other hand, using solid electrolytes instead of organic solvent based liquid electrolytes can effectively improve battery safety. Compared with liquid electrolytes, solid electrolytes will not spontaneously ignite even in the event of a short circuit in the battery. Therefore, developing and commercialization all-solid-state batteries is one of the keys for next generation batteries development.

1.4 Structure of all-solid-state battery

A commercial Li-ion battery currently in use mainly contains a Cu current collector, an anode electrode (graphite), a separator, a cathode electrode and an Al current collector. Liquid electrolyte is filled in the whole battery cell. Both anode electrode and cathode electrode are porous electrodes consisting of active materials, binder, and electrically conductive additives[18]. The porous electrode leaves space for liquid electrolyte flowing in to increase the contact area between the two. However, this also decreases volume specific energy density of the battery[19]. The biggest difference between all-solid-state batteries and commercial Li-ion batteries is the use of a solid electrolyte instead of an organic solvent-based electrolyte. The presence of a solid electrolyte physically separates cathode and anode to avoid their direct contact. Therefore, a separator is no longer needed[20]. More importantly, the usage of solid electrolyte makes it possible to use metallic Li as anode directly to replace carbon based materials, such as graphite that is widely used for commercial Li-ion batteries anode. Compared with graphite anode having theoretical specific capacity 372 mAh g^{-1}, metallic Li used as anode has theoretical specific capacity of 3680 mAh g^{-1}, which is around 10 times larger than graphite anode. Therefore, metallic Li can greatly increase battery energy density[21]. The structure comparison of commercial liquid electrolyte-based Li ion battery and all-solid-state battery is shown in Figure 1.2.

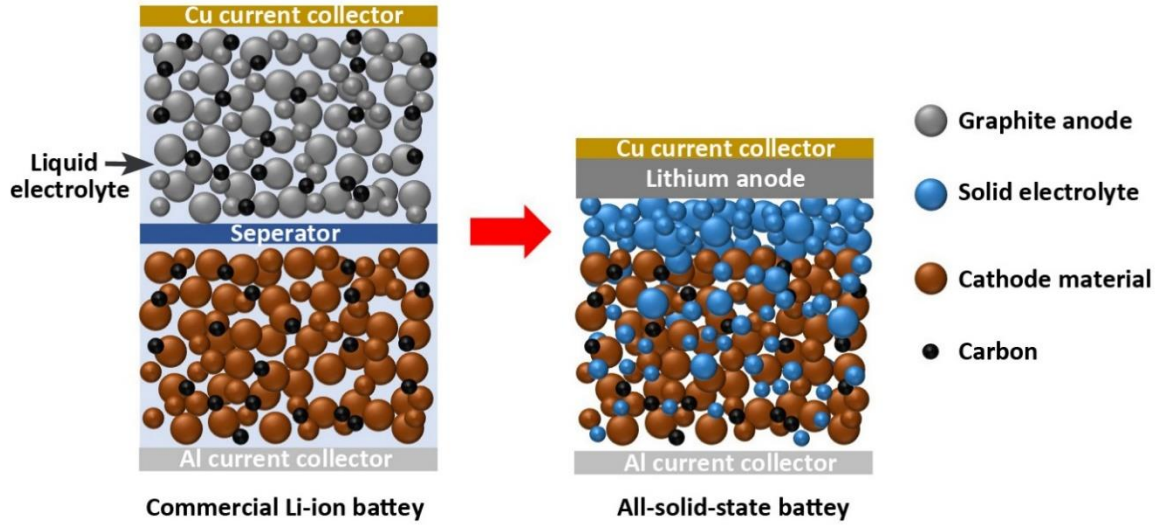

Figure 1.2 Schematic illustration of commercial Li-ion battery and all-solid-state battery.

When an all-solid-state battery is charged, Li ions are extracted from the cathode materials, and move across the interface between cathode electrode and solid electrolyte to enter the solid electrolyte. Then Li ions move toward the anode side in solid electrolytes. At the solid electrolyte and anodic metallic Li electrode interface, Li ions are reduced into metallic Li on the anode electrode surface. During the charging process, electrical energy transforms into chemical energy for storage in the battery. When an all-solid-state battery is discharged, Li on the metallic Li anode surface is oxidized into Li ions. The electrochemical potential difference between cathode and anode drives Li ions to the cathode side along the solid electrolyte. Finally, Li ions are embedded into the cathode to complete the conversion from chemical energy to electrical energy.

1.5 The advantages of all solid state batteries

Generally, all-solid-state batteries have four outstanding advantages over liquid electrolyte-based Li-ion batteries, which are the reasons why all-solid-state batteries are considered as next-generation batteries[20].

1) High energy density:

   Metallic Li has the highest specific capacity and lowest de-lithiation/lithiation potential vs. Li/Li^+. Also, solid electrolytes have wider electrochemical stability voltage window, which allows the battery to be charged to higher a voltage. All-solid-state

batteries could have up to 2.5 times larger energy density than current commercial Li-ion batteries.

2) High power density:

   All-solid-state batteries are expected to have higher power density. As solid electrolyte exhibit larger thermal conductivity than liquid electrolytes, heat can be quickly released in all-solid-batteries under fast charge-discharge process. This rapid cooling can effectively prevent the formation of "hot spots", which tend to slow ion movement dynamics. Thus, all-solid-state batteries are allowed to charge-discharging under high current.

3) Safety:

   Compared with flammable organic solvents used as liquid electrolytes, solid electrolytes used in all-solid-state batteries are normally non-flammable. Therefore, all-solid-state batteries are less prone to catch fire even in the event of a short circuit or violent impact.

4) Environmentally friendly:

   There are no volatile elements or toxic organic compounds in all-solid-state batteries, making them environmentally friendly.

1.6 The challenges on developing all solid state batteries

Even though there are many advantages of all-solid-state batteries as next-generation batteries, there are also many challenges that need to be overcome before commercialization.

1.6.1 Low ionic conductivity of solid electrolyte

Solid electrolytes have obvious advantages compared to liquid electrolytes, as mentioned above. However, solid electrolytes also have shortcomings that limit its application. The most obvious one is the lower ionic conductivity compared to organic solvent-based liquid electrolytes[22]. Even though more and more efforts have been devoted on improving the ionic conductivity of solid electrolytes – some kinds of solid electrolytes are reported with the ionic conductivity reaching to 10^{-2} S/cm – the ionic conductivity of solid electrolytes is still overall

lower than liquid electrolytes.

1.6.2 Interfacial challenges

In addition to solid electrolyte bulk ionic conductivity limitations, interfacial problems are also significant challenges for all-solid-state battery development. There are many interfaces in all-solid electrolytes, as shown in Figure 1.3, including: the interface between solid electrolyte and cathode/anode active material, the interface between cathode active material and the current collector, the interface between the cathode material and electrically conductive additives, the grain boundaries in oxide solid electrolytes, and more[23-25]. The presence of interfaces cause complex and challenging problems. I divide the interfacial problems into four main types: physical contact losses, interfacial side reactions, space charge layer resistance, and Li dendrites growth, which I will discuss in the next paragraphs.

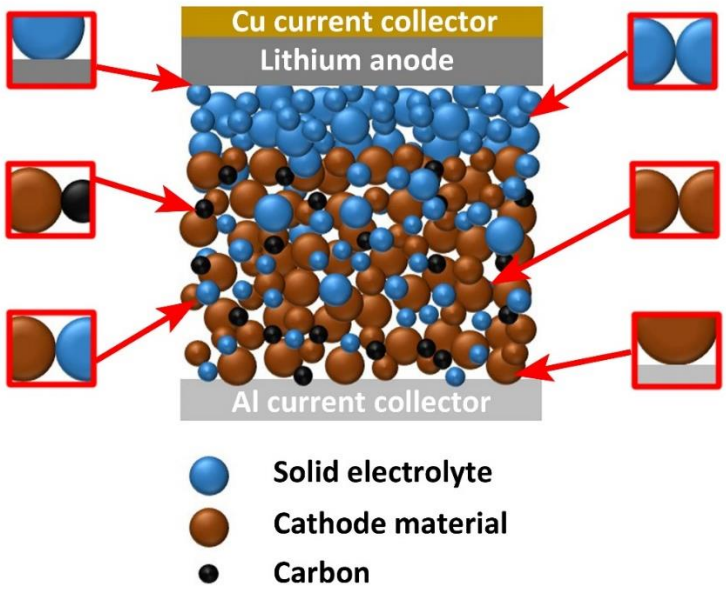

Figure 1.3 Different kinds of interfaces in all-solid-state battery.

1.6.2.1 Physical contact lose

Liquid electrolyte could flow into all the voids in electrodes or on electrode surfaces, creating close contact with electrodes. On the other hand, solid electrolytes always face the problem of having poor contact with both cathode and anode electrodes, which leaves interfacial defects and voids, and increases interfacial resistance. Also, due to poor flexibility and

deformability, solid electrolytes cannot adapt to electrode deformation or volume changes[26]. This means that the contact problem between the solid electrolyte and the cathode/anode electrode becomes worse with the number of charging/discharging cycles[27], as shown in Figure 1.4. As a result, the worsened interfacial physical contact affects battery performance[28].

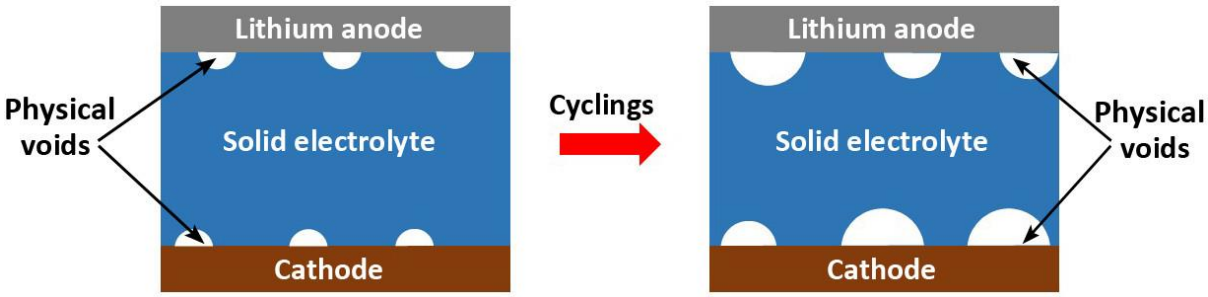

Figure 1.4 Schematic diagram of voids formation at electrodes and solid electrolyte interface.

1.6.2.2 Interfacial side reaction

The chemical instability of solid electrolytes in contact with electrode active materials, especially with a metallic Li anode, is another challenge slowing the improvement of all-solid-state battery performance. Because of the different chemical properties of different solid electrolytes, there are three types of interfacial reactions between solid electrolytes and electrode:

1) Kinetically stable interface,
2) Continuously reactive or unstable interface, and
3) The interface with an interlayer forms by a self-limiting reaction.

The first situation is the most ideal one, where the solid electrolyte is thermodynamically stable with the electrode (especially with metallic Li anode). This kind of interface, without interphase formation, only allows Li ions move across but not electrons, as shown in Figure 1.5a. However, this kind of interface only can be observed in some certain solid electrolytes that match with certain electrodes, such as the Li|$Li_7La_3Zr_2O_{12}$ interface[29]. The second situation is where the solid electrolyte is reactive or chemical unstable with the electrode (mostly with a metallic Li anode) to form interphase at the interface. Depending on the conduction property, the formed interphase can be further divided into two kinds. One is the

mixed conducting interphase, which can conduct both electrons and Li ions. For this kind of interphase, the interfacial reaction cannot be self-controlled and the thickness would continuously increase with number of cycles (Figure 1.5b) [30,31]. The other one is ionic conducting interphase with ignorable electronic conductivity. This kind of interphase in more stable because of self-limiting reaction (Figure 1.5c) [32]. In general, interfacial side reaction is an important factor that needs to be taken seriously. Especially the formation of mixed conducting interphase need to be avoided.

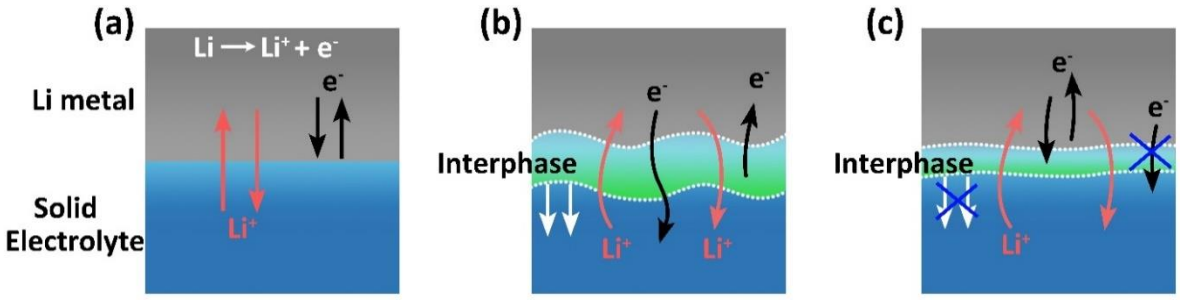

Figure 1.5 Three kinds of interphase/interface between Li electrode and solid electrolyte. **a** Thermodynamically stable interface, **b** mixed-ionic/electronic conduction interphase, **c** ionic conduction but electrically insulating interphase.

1.6.2.3 Space charge layer

Unlike interfacial physical defects and interfacial side reactions, which are being intensively studied, space charge layer resistance is more mysterious but cannot be ignored when discussing interfacial problems. In all-solid-state batteries, space charge layers form from the redistribution of Li ions at interface because of the chemical potential difference between Li in solid electrolytes and electrode active materials[33]. The existence of a space charge layer, particularly in the cathode|solid electrolyte interface, are thought to affect Li ions transport across the interface[34]. Even though the existence of a space charge layer may enhance the ionic conduction in solid-solid dispersions with poor bulk Li ionic conduction ability, a space charge layer is widely thought to be an additional barrier for Li-ion transport because solid electrolytes already have been be designed with high ionic conductivity (Figure 1.6) [35]. Until now, the role of space charge layer in all-solid-state batteries is still not clear. In Chapter 4,

with the help of advanced operando characterization techniques, we track space charge layer evolution in all-solid-state batteries and quantify space charge layer resistance.

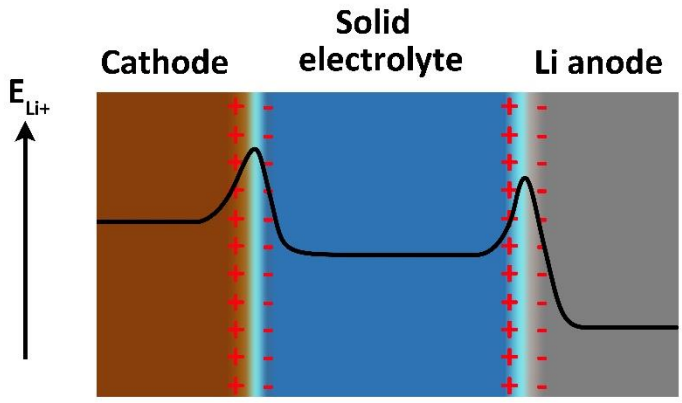

Figure 1.6 Schematic diagram of space charge layers in all solid state batteries.

1.6.2.4 Li dendrites growth

Li dendrites formation and growth in grain boundaries of polycrystalline solid electrolyte is also a problem needs to be carefully treated. It was previously considered that as opposed to liquid electrolytes, solid electrolytes higher strength and stiffness, and can therefore prevent the growth, or even penetration, of Li dendrites, which is the main limitation of the usage of metallic Li as anode in liquid electrolyte-based batteries. However, experiments show that even the oxide solid electrolytes with the large stiffness and strength still cannot fully prevent the formation of and penetration into Li dendrites[36-38]. As a result, all-solid-state batteries also face the problem of potential short circuit under high current or cyclic aging, because Li dendrites can penetrate the solid electrolyte to reach cathode electrode side. Until now, there is controversy on the origin of dendrite formation at grain boundaries in polycrystalline solid electrolytes. Some hold the view that Li dendrites originate from Li anode and solid electrolyte interface. Because of the weak mechanical properties at grain boundaries, Li dendrites can penetration into grain boundaries until reaching to cathode electrode (model 1 in Figure 1.7). However, some hold different view that Li dendrites originate grain boundaries because of different grain boundaries conduction properties under battery working condition. As a results, those independently formed Li dendrites at grain boundaries forms a network to fail

batteries (model 2 in Figure 1.7). In Chapter 3, we clarify the origin of Li dendrites in grain boundaries via operando microscopy techniques.

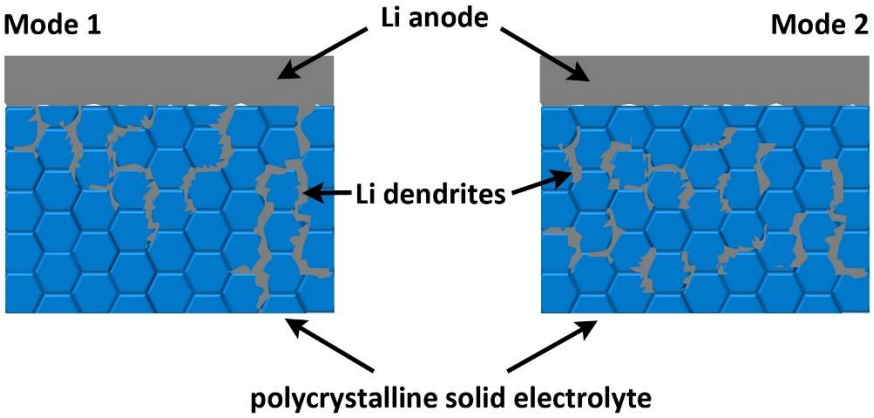

Figure 1.7 Two models on revealing Li dendrites formation in grain boundaries in polycrystalline solid electrolytes.

1.7 Motivation

1.7.1 Challenges on interfaces need more studies in the future

After recognizing the challenges mentioned above related to all-solid-state battery interfaces, many efforts have been made by researchers to overcome them and improve all-solid-state battery practical performance. For example, to further improve solid electrolytes performance and lift the limitations of solid electrolytes' shortcomings, hybrid solid electrolytes were developed. They consist of polymer electrolytes as matrices and oxide solid electrolytes as additives[39-41]. On one hand, flexible polymer solid electrolyte matrices can improve physical contact with electrodes and adapt to electrode deformation during battery cycling. On the other hand, oxide solid electrolytes can improve the whole hybrid electrolyte ionic conductivity. To improve the interfacial physical contact between the Li|$Li_7La_3Zr_2O_{12}$ interface, an atomic Al_2O_3 layer was deposited on an LLZO surface. Because of the higher binding of Li with lithiated alumina, a conformal Li|$Li_7La_3Zr_2O_{12}$ interface with only 1 Ω cm^2 resistance was prepared[42].

However, until now, research on space charge layers at all-solid-state battery interfaces and the origin of Li dendrites easily penetrating a solid electrolyte, especially along grain

boundaries, are still limited. Compared to interfacial physical contact problems and interfacial side reactions, those two kinds of interfacial problems are more challenging to characterize. As a result, fewer effective methods are applied to eliminate their negative effects. Therefore, new methods are needed to further battery internal interface characterization.

1.7.2 Possibility of KPFM being used on all solid-state batteries' internal interfaces research

Kelvin probe force microscopy (KPFM) is a technology based on scanning force microscopy (SFM), which can be used to detect surface contact potential difference (CPD) between a sample and an SFM tip by measuring electrostatic force between sample and tip[43,44]. With this function, KPFM recently began to be used to characterize the potential distribution in perovskite solar cells and cathode electrodes in batteries[45-47].

Space charge layers and Li dendrites' easy penetration along grain boundaries in solid electrolytes are both believed to be possibly related to charge redistribution at internal interfaces or grain boundaries in solid electrolytes. It is this existence of redistributed charges that could change the potential distribution at internal interfaces in all-solid-state batteries or grain boundaries in solid electrolytes. Therefore, applying KPFM techniques to all-solid-state battery internal potential can provides us with a novel chance to track the origin of space charge layer formations and Li dendrites' easy penetration along grain boundaries in all-solid-state batteries.

1.8 Reference

1 Lukatskaya, M. R., Dunn, B. & Gogotsi, Y. Multidimensional materials and device architectures for future hybrid energy storage. *Nat. Commun.* **7**, 12647 (2016).

2 Kittner, N., Lill, F. & Kammen, D. M. Energy storage deployment and innovation for the clean energy transition. *Nat. Energy* **2**, 1-6 (2017).

3 Reddy, M. V., Mauger, A., Julien, C. M., Paolella, A. & Zaghib, K. Brief history of early lithium-battery development. *Materials* **13**, 1884 (2020).

4 Cao, W., Zhang, J. & Li, H. Batteries with high theoretical energy densities. *Energy Stor. Mater.* **26**, 46-55 (2020).

5 Grey, C. P. & Hall, D. S. Prospects for lithium-ion batteries and beyond—a 2030 vision. *Nat. Commun.* **11**, 6279 (2020).

6 Sanguesa, J. A., Torres-Sanz, V., Garrido, P., Martinez, F. J. & Marquez-Barja, J. M. A review on electric vehicles: Technologies and challenges. *J. Smart Cities* **4**, 372-404 (2021).

7 Pimentel, D. *et al.* Food production and the energy crisis. *Science* **182**, 443-449 (1973).

8 Whittingham, M. S. Electrical energy storage and intercalation chemistry. *Science* **192**, 1126-1127 (1976).

9 Whittingham, M. S. Lithium batteries and cathode materials. *Chem. Rev.* **104**, 4271-4302 (2004).

10 Mizushima, K., Jones, P., Wiseman, P. & Goodenough, J. B. Li$_x$CoO$_2$ (0<x<-1): A new cathode material for batteries of high energy density. *Mater. Res. Bull.* **15**, 783-789 (1980).

11 Li, M., Lu, J., Chen, Z. & Amine, K. 30 years of lithium-ion batteries. *Adv. Mater.* **30**, 1800561 (2018).

12 Thackeray, M. M., David, W. I., Bruce, P. G. & Goodenough, J. B. Lithium insertion into manganese spinels. *Mater. Res. Bull.* **18**, 461-472 (1983).

13 Crabtree, G., Kócs, E. & Trahey, L. The energy-storage frontier: Lithium-ion batteries and beyond. *MRS Bull.* **40**, 1067-1078 (2015).

14 Padhi, A. K., Nanjundaswamy, K. S. & Goodenough, J. B. Phospho-olivines as positive-electrode materials for rechargeable lithium batteries. *J. Electrochem. Soc.* **144**, 1188 (1997).

15 Judez, X. *et al.* Opportunities for rechargeable solid-state batteries based on Li-intercalation cathodes. *Joule* **2**, 2208-2224 (2018).

16 Girishkumar, G., McCloskey, B., Luntz, A. C., Swanson, S. & Wilcke, W. Lithium–air battery: promise and challenges. *J. Phys. Chem. Lett.* **1**, 2193-2203 (2010).

17 Liu, K., Liu, Y., Lin, D., Pei, A. & Cui, Y. Materials for lithium-ion battery safety. *Sci. Adv.* **4**, eaas9820 (2018).

18 Yao, X.-Y., Saxena, S., Su, L. & Pecht, M. G. The explosive nature of tab burrs in Li-ion batteries. *IEEE Access* **7**, 45978-45982 (2019).

19 Vu, A., Qian, Y. & Stein, A. Porous electrode materials for lithium-ion batteries–how to prepare them and what makes them special. *Adv. Energy Mater.* **2**, 1056-1085 (2012).

20 Janek, J. & Zeier, W. G. A solid future for battery development. *Nature Energy* **1**, 1-4 (2016).

21 Li, J. *et al.* Strategies to anode protection in lithium metal battery: A review. *InfoMat* **3**, 1333-1363 (2021).

22 Zhu, L. *et al.* Enhancing ionic conductivity in solid electrolyte by relocating diffusion ions to under-coordination sites. *Sci. Adv.* **8**, eabj7698 (2022).

23 Krauskopf, T., Richter, F. H., Zeier, W. G. & Janek, J. r. Physicochemical concepts of the lithium metal anode in solid-state batteries. *Chem. Rev.* **120**, 7745-7794 (2020).

24 Tian, Y. *et al.* Promises and challenges of next-generation "beyond Li-ion" batteries for electric vehicles and grid decarbonization. *Chem. Rev.* **121**, 1623-1669 (2020).

25 Banerjee, A., Wang, X., Fang, C., Wu, E. A. & Meng, Y. S. Interfaces and interphases in all-solid-state batteries with inorganic solid electrolytes. *Chem. Rev.* **120**, 6878-6933 (2020).

26 Sun, N. *et al.* Anisotropically Electrochemical–Mechanical Evolution in Solid-State Batteries and Interfacial Tailored Strategy. *Angew. Chem.* **131**, 18820-18826 (2019).

27 Kasemchainan, J. *et al.* Critical stripping current leads to dendrite formation on plating in lithium anode solid electrolyte cells. *Nat. Mater.* **18**, 1105-1111 (2019).

28 Lou, S. *et al.* Multi-scale imaging of solid-state battery interfaces: from atomic scale to macroscopic scale. *Chem* **6**, 2199-2218 (2020).

29 Duan, H., Zheng, H., Zhou, Y., Xu, B. & Liu, H. Stability of garnet-type Li ion conductors: An overview. *Solid State Ion.* **318**, 45-53 (2018).

30 Wenzel, S. *et al.* Direct observation of the interfacial instability of the fast ionic conductor $Li_{10}GeP_2S_{12}$ at the lithium metal anode. *Chem. Mater.* **28**, 2400-2407 (2016).

31 Hartmann, P. *et al.* Degradation of NASICON-type materials in contact with lithium metal: formation of mixed conducting interphases (MCI) on solid electrolytes. *J. Phys. Chem. C.* **117**, 21064-21074 (2013).

32 Wenzel, S. *et al.* Interphase formation and degradation of charge transfer kinetics between a lithium metal anode and highly crystalline $Li_7P_3S_{11}$ solid electrolyte. *Solid State Ion.* **286**, 24-33 (2016).

33 Shen, Y. *et al.* Unlocking the energy capabilities of lithium metal electrode with solid-state electrolytes. *Joule* **2**, 1674-1689 (2018).

34 Wang, L. *et al.* In-situ visualization of the space-charge-layer effect on interfacial lithium-ion transport in all-solid-state batteries. *Nat. Commun.* **11**, 5889 (2020).

35 Cheng, Z. *et al.* Revealing the impact of space-charge layers on the Li-ion transport in all-solid-state batteries. *Joule* **4**, 1311-1323 (2020).

36 Shen, F., Dixit, M. B., Xiao, X. & Hatzell, K. B. Effect of pore connectivity on Li dendrite propagation within LLZO electrolytes observed with synchrotron X-ray tomography. *ACS Energy Lett.* **3**, 1056-1061 (2018).

37 Cheng, E. J., Sharafi, A. & Sakamoto, J. Intergranular Li metal propagation through polycrystalline $Li_{6.25}Al_{0.25}La_3Zr_2O_{12}$ ceramic electrolyte. *Electrochim. Acta* **223**, 85-91 (2017).

38 Liu, X. *et al.* Local electronic structure variation resulting in Li 'filament'formation within solid electrolytes. *Nat. Mater.* **20**, 1485-1490 (2021).

39 Pan, K. *et al.* A flexible ceramic/polymer hybrid solid electrolyte for solid-state lithium metal batteries. *Adv. Mater.* **32**, 2000399 (2020).

40 Kim, J.-K., Lim, Y. J., Kim, H., Cho, G.-B. & Kim, Y. A hybrid solid electrolyte for flexible solid-state sodium batteries. *Energy Environ. Sci.* **8**, 3589-3596 (2015).

41 Feng, J. *et al.* PEO based polymer-ceramic hybrid solid electrolytes: a review. *Nano Converg.* **8**, 1-12 (2021).

42 Han, X. *et al.* Negating interfacial impedance in garnet-based solid-state Li metal batteries. *Nat. Mater.* **16**, 572-579 (2017).

43 Melitz, W., Shen, J., Kummel, A. C. & Lee, S. Kelvin probe force microscopy and its application. *Surf. Sci. Rep.* **66**, 1-27 (2011).

44 Axt, A., Hermes, I. M., Bergmann, V. W., Tausendpfund, N. & Weber, S. A. Know your full potential: Quantitative Kelvin probe force microscopy on nanoscale electrical devices. *Beilstein J. Nanotechnol.* **9**, 1809-1819 (2018).

45 Weber, S. A. *et al.* How the formation of interfacial charge causes hysteresis in perovskite solar cells. *Energy Environ. Sci.* **11**, 2404-2413 (2018).

46 Masuda, H., Ishida, N., Ogata, Y., Ito, D. & Fujita, D. Internal potential mapping of charged solid-state-lithium ion batteries using in situ Kelvin probe force microscopy. *Nanoscale* **9**, 893-898 (2017).

47 Fuller, E. J. *et al.* Spatially resolved potential and li-ion distributions reveal performance-limiting regions in solid-state batteries. *ACS Energy Lett.* **6**, 3944-3951 (2021).

Chapter 2 Revealing origin of measured CPD signal change on mixed-ions-electrons conductor under non-equilibrium state with KPFM

2.1 Introduction

Kelvin probe force microscopy (KPFM) is a technique based on scanning force microscopy (SFM), which is widely recognized for measuring local contact potential difference (CPD) value between sample and SFM tip[1]. KPFM now is mainly used for characterizing surface corrosion and coatings of metal/semiconductor with high spatial resolution[2,3]. In normal KPFM measurement, sample is electrically connected with SFM tip under equilibrium state. For example, Sharma et al. used KPFM to detect that nano-roughened, sol-gel derived polycrystalline ZnO thin film, which exhibits two different work function values on a sub-micrometer scale[4].

Different with KPFM being used to characterize electronic conductive metal/semiconductor under equilibrium state (Figure 2.1a), recent years, KPFM is tried to be used for characterizing mixed-ionic-electronic conductors (MIEC), which conduct both electrons and ions, under non-equilibrium state such as an additional lateral bias being applied (Figure 2.1b). In those system, KPFM is thought can be used to obtain information about electric field redistribution, local charge carrier redistribution and work function changes for perovskite solar cells, lithium (Li) ion batteries and so on according to comparing measured CPD change between equilibrium and non-equilibrium state[5-8].

However, it is the existence of mobile ions in mixed conductor, the role of ions in KPFM measurements is still not clear for us until now, which easily leads us misinterpret the origin of measured KPFM signal change under non-equilibrium state. Additionally, due to the difference of research area, different nomenclatures are used to interpret KPFM signal and its change. This terminological inconsistency between physicists and electrochemists was also noted by Erich Lange[9] for the general case and highlighted by Örnek *et al.* [10] for the specific

case of KPFM. This unintended language barrier can be confusing and even controversial on KPFM signal interpretation for people with different background. For those above reasons, we aim to pave the way towards a common understanding of the signal interpretation of KPFM on both pure electronic conductor and mixed conductor under both equilibrium and non-equilibrium state.

In this work, firstly we clarify the relation of work function and Volta (outer) potential, surface potential, Galvani (inner) potential, electron's electrochemical potential from the view of electrochemistry. Then based on this terminology we outline the theoretical basis of KPFM. Further, we theoretically analyze different potentials known from electrochemistry contribute to the KPFM signal. Last, we verify our theoretical explanation by using KPFM to measure Hebb-Wagner-cell (HWC) under additional external polarization.

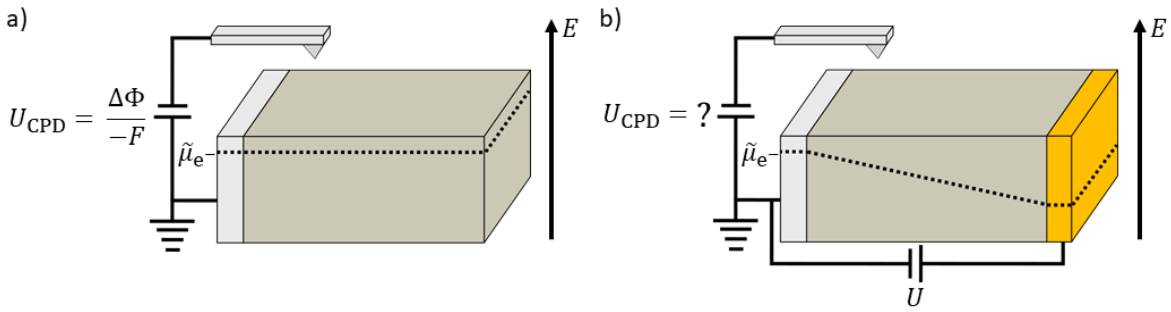

Figure 2.1 Schematic diagram of **a** KFPM measurement on metal/semiconductor sample under equilibrium state, where there is no electron electrochemical potential gradient in sample and **b** KPFM measurement on ionic/mixed conductivity sample under non-equilibrium state, where is there is electron electrochemical potential gradient in sample because of external potential being applied on sample.

2.2 Clarification the relation of different potentials

Considering this situation, an electronic conductor is surrounded by a vacuum. A test charge of one electron locates at an infinite distance from the conductor. Then the test charge is to be inserted into the sample. The total amount of energy to complete this task is now discussed.

The starting point of the explanation is given by the test charge at infinite distance from all other charges and is defined as the reference point **R**. By this definition, the test charge at **R** has a potential energy of zero. The **Volta potential** Ψ is defined as the electrostatic potential

difference between this reference point **R** and a point **S** "just above" the surface (~ 10 nm) of the target sample, which has excess charges, in the isolated system(Figure 2.2a). This electrostatic potential difference equals to the work applied to move the test charge from **R** to **S** because of the existence of Coulomb force between test charge and sample[10,11]. At shorter distances to the surface, dispersion interactions occur of which the interaction with induced image charges has the longest range. Therefore, at distances < 10 nm, the test charge gives rise to an additional potential contribution, which needs to be considered as surface potential. For this reason, the Volta potential is defined specifically to a point **S** "just above" the surface[12,13].

More work is required to move the charge from point **R** to point **I** within the sample (Figure 2.2b). This work is defined as the **surface potential** χ and stems from the existing electrical double layer at the surface of sample. For an electrically conductive sample, the electrostatic potential at any given point inside the material will be uniform. Therefore, it is not necessary to further specify the location of point **I**.

The sum of the aforementioned two potentials – which are both based on electrostatic interactions – is defined as the **Galvani potential** φ**:**[14]

$$\varphi = \Psi + \chi \tag{1}$$

Finally, inside the sample there is an energy contribution related to the chemical interactions which the electron takes part in. After the test charge being moved into sample, additional work needs to be applied to let the test charge occupy certain electronic states such as bands or orbitals in the sample. This work is named **chemical potential of electrons** μ_{e^-}[11].

The total amount of energy that is needed for the insertion of an electron from **R** to point **I** is the **electrochemical potential of electrons** $\tilde{\mu}_{e^-}$ and is described by equation 2 with $j = e^-$.

$$\tilde{\mu}_j = \mu_j + z_j e N_A \varphi = \mu_j + z_j F(\chi + \Psi) \tag{2}$$

Here $z_j e$ denotes the charge of the particle j of interest as an integral multiple z_j of the elementary charge e and N_A is the Avogadro constant. For the mentioned example of an

electron z_j equals -1. F is the Faraday constant. The electrochemical potential of electrons is identical to the Fermi level E_F which is much more common in physics[12].

We note that the separation of energies, which are required to move an electron from point **S** to point **I**, is only conceptually. In practice, the chemical potential of electrons μ_{e^-} and the surface potential χ cannot be measured separately. Instead, one only can measure the total energy required to remove an electron from the sample (point **I**) to a point just above the surface (point **S**). This energy is called work function Φ[15].

$$\Phi = -\mu_{e^-} - zF\chi \tag{3}$$

The negative sign originates from the reverse direction of movement of the electron with respect to the definition of μ_{e^-} and χ.

Based on the above discussion, the relationship of different kinds of potential are shown in Figure 2.2c[16].

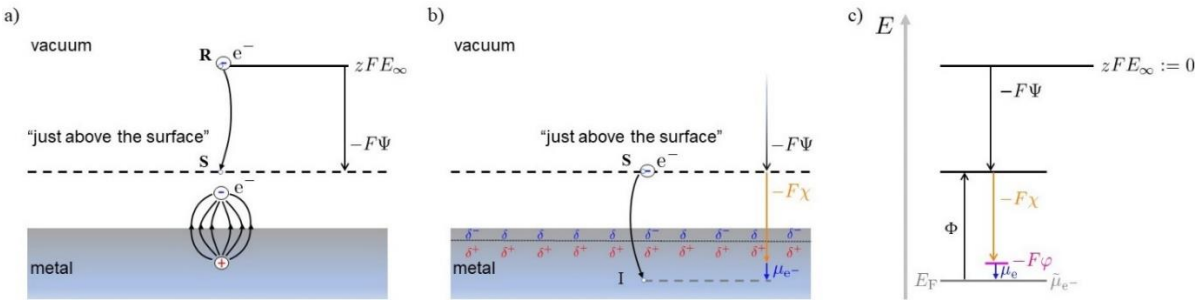

Figure 2.2 a Schematic diagram of Volta potential, which is the work applied to move a test charge from infinite distance to "just above" the surface of a target sample. **b** Schematic diagram of surface potential and chemical potential of bringing a test charge from "just above" the surface of a target sample into the inner part of the sample. **c** Schematic representation of the potentials known from electrochemistry.

2.3 KPFM measurements theory

The CPD between SFM tip and sample can be measured by KPFM because of the existence of electrostatic force between SFM tip and sample. This electrostatic force forms from Volta potential difference between SFM tip and sample[10].

Before KPFM measurement, SFM tip is not electrical connected with sample. And the electrochemical potentials of electrons will only equilibrate within the probe and sample respectively, i.e. $\tilde{\mu}_{e^-,t}$ for the probe and $\tilde{\mu}_{e^-,s}$ for the sample, respectively (Figure 2.3a). Consequently, the tip of the probe has a certain Volta potential Ψ_t and the surface of the sample has another Volta potential Ψ_s. Once an electronic connection between the probe and the sample is established, electrons in the part having a higher electrochemical potential flow into the part with lower electrochemical potential until the electrochemical potential of electrons (or Fermi energy) is equilibrated everywhere (Figure 2.3b). At this situation, the difference in Ψ_t and Ψ_s is the negative of the difference in work function of tip Φ_t and sample Φ_s. The latter is the CPD between SFM tip and sample surface named as U_{CPD}. Therefore, the electrostatic force between SFM tip and sample F_{el} can be calculated the following equation 4[1,17]:

$$F_{el} = \frac{1}{2}\frac{dC}{dz}(\Delta\Psi)^2 = \frac{1}{2}\frac{dC}{dz}(U_{CPD})^2 \quad (4)$$

To further decide the value of U_{CPD}, an additional DC voltage U_{DC} is applied on SFM tip to compensate U_{CPD} with the help of SFM feedback system. As a result, electrostatic force F_{el} changes to 0 because the Volta potential of SFM probe and sample equal with each other (Figure 2.3c). And U_{CPD} is decided by U_{DC} applied:

$$U_{CPD} = U_{DC} = \Psi_t - \Psi_s = -\frac{\Phi_t - \Phi_s}{F} \quad (5)$$

Except the above discussion on sample under equilibrium state, KPFM is also needed to be used to measure sample under non-equilibrium or polarization state. As Figure 2.3d shows, an additional external potential φ_{ap} is applied on sample after SFM probe is electrically connected to sample. In this situation, the electrochemical potential of electrons (or Fermi energy) in sample changes to $\tilde{\mu}'_{e^-,s}$, which does not equal to SFM probe's anymore. The CPD between SFM tip and sample surface changed to U'_{CPD}:

$$U'_{CPD} = \Psi_t - \Psi'_s + \varphi_{ap} = -\frac{\Phi_t - \Phi'_s}{F} + \frac{\tilde{\mu}'_{e^-,s} - \tilde{\mu}_{e^-,s}}{F} \quad (6)$$

To decide the value of U'_{CPD}, an additional DC voltage is also applied on SFM tip to compensate the electrostatic force results from Volta potential difference between tip and sample. The applied DC voltage numerically equals to U'_{CPD} (Figure 2.3e).

Therefore, the CPD change of measured sample from equilibrium state to non-equilibrium state can be described as:

$$\Delta U_{CPD} = U'_{CPD} - U_{CPD} = \frac{\Phi'_s - \Phi_s}{F} + \frac{\tilde{\mu}'_{e^-,s} - \tilde{\mu}_{e^-,s}}{F} \quad (7)$$

If we bring equation 1 and equation 3 into equation 7,

$$\Delta U_{CPD} = (\chi_s - \chi'_s) + (\varphi'_s - \varphi_s) \quad (8)$$

Therefore, CPD change of measured sample in non-equilibrium state is related with surface potential change and Galvani potential change.

For metal and semiconductor, surface potential, which is related with surface polarization, does not change even under non-equilibrium state since the composition of metal and semiconductor do not change. Thus, CPD change in non-equilibrium state compared with equilibrium state is only related with Galvani potential change. For MIEC with very low or even neglible electronic conductivity, surface potential change is also negliable even under non-equilibrium state or polarization since ion concentration almost does not change. Thus, CPD change is also mainly related with Galvani potential change.

From above theoretical analysis, we know that CPD change detected by KPFM on both metal/semiconductor and MIEC is mainly only related with Galvani potential change. To verify our explanation on CPD change, we did KPFM measurements on HWC under different non-equilibrium state.

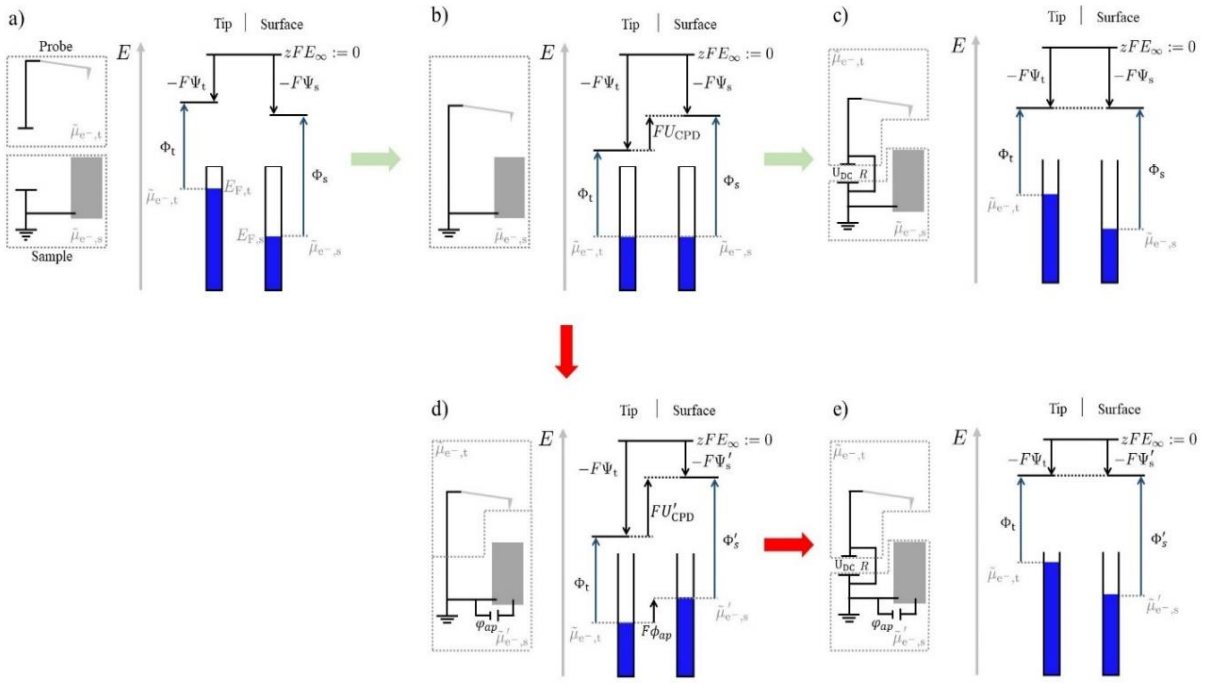

Figure 2.3 Schematic representation of the operating principle of KPFM. **a** Theoretical state with no electric connection. **b** Established electric connection between probe and sample. **c** A DC voltage is applied on SFM probe to compensate potential difference between probe and sample. **d** An additional external potential applied on sample to shift sample into non-equilibrium state after electric connection between probe and sample being established. **e** A DC voltage is applied on SFM probe to compensate potential difference between probe and sample after sample in non-equilibrium.

2.4 Hebb-Wagner-Cell under polarization state

HWC is a cell with the structure of reversible electrode|MIEC|irreversible electrode. The usage of HWC can separate electron current in MIEC from all kinds charge current by applying positive potential on irreversible electrode. The separated electron flow results from electron chemical potential difference in MIEC from the side close to reversible electrode to the side close to irreversible electrode[18,19]. With this special property, we have the chance to experimentally verify whether CPD change measured by KFPM on MIEC is related with electron chemical potential change or not.

Here, we choose the MIEC - Li_3PO_4 with lithium (Li) ion and electron are the only two kinds of movable charges in the cell as model system. Reversible electrode is metal Li and irreversible

electrode is gold (Au). In the HWC, when a positive potential is applied on irreversible electrode. The current density in MIEC quickly decreases from over 1 μA to tens of nA in 100 s polarization. Finally the current density in MIEC keeps stable at around 2 - 3 nA after 200 s polarization (Figure 2.4a). We generally divide polarization process into two parts. The first part is the first 100 s polarization after external potential being applied on irreversible electrode to generate an electric field in Li_3PO_4. It is the electric field creates MIEC internal Galvani potential gradient, which promotes ions in Li_3PO_4 move towards the reversible electrode and electrons move towards to irreversible electrode (Figure 2.4b). The second part is after 100 s polarization. Since irreversible electrode in HWC is ion—blocking electrode, it does not provide continuous ions for Li_3PO_4, Thus, vacancies of ions will gradually form in the Li_3PO_4 adjacent to the ion-blocking electrode with time increasing, which shields the external electric field and leads to a diminishing gradient in the Galvani potential in Li_3PO_4. This results in a decreasing ionic current until it vanishes (Figure 2.4b). The changes in the Li ions concentration required to shield the external field are limited compared with the large concentration of ions in Li_3PO_4, the chemical potential of Li ions can be seen not altered. Thus, the chemical potential of Li ions is also gradient-free within the Li_3PO_4. Then it can be speculated that the electrochemical potential of Li ions $\tilde{\mu}_{Li^+}$ is also gradient-free (Figure 2.4c) due to the both profiles of the Galvani and the chemical potential of Li ions in Li_3PO_4 are gradient-free.

However, different with ions current, electrons current still constantly exists in Li_3PO_4 even in the second polarization time scale. The vacancies of ions form in the Li_3PO_4 adjacent to the ion-blocking electrode after 100 s polarization creates local charge imbalance in Li_3PO_4, which leads redistribution of electrons/holes in Li_3PO_4. Since electrons/holes are minority charge carriers in Li_3PO_4, the resulting concentration changes are not negligible and thereby locally change the chemical potential of electrons. After taking the gradient-free of Galvani potential in Li_3PO_4 into consideration, we can decide that there is electron electrochemical potential gradient in Li_3PO_4, which gives rise to a finite constant electronic current[20].

Based on the special properties of HWC as intruded above, we have the chance to carry on operando KPFM measurements on the sample, which experiences different polarization state

because of different internal potential gradient. More importantly, we have chance to verify whether CPD signal change on Li_3PO_4 under non-equilibrium is related with Galvani potential change or other factors.

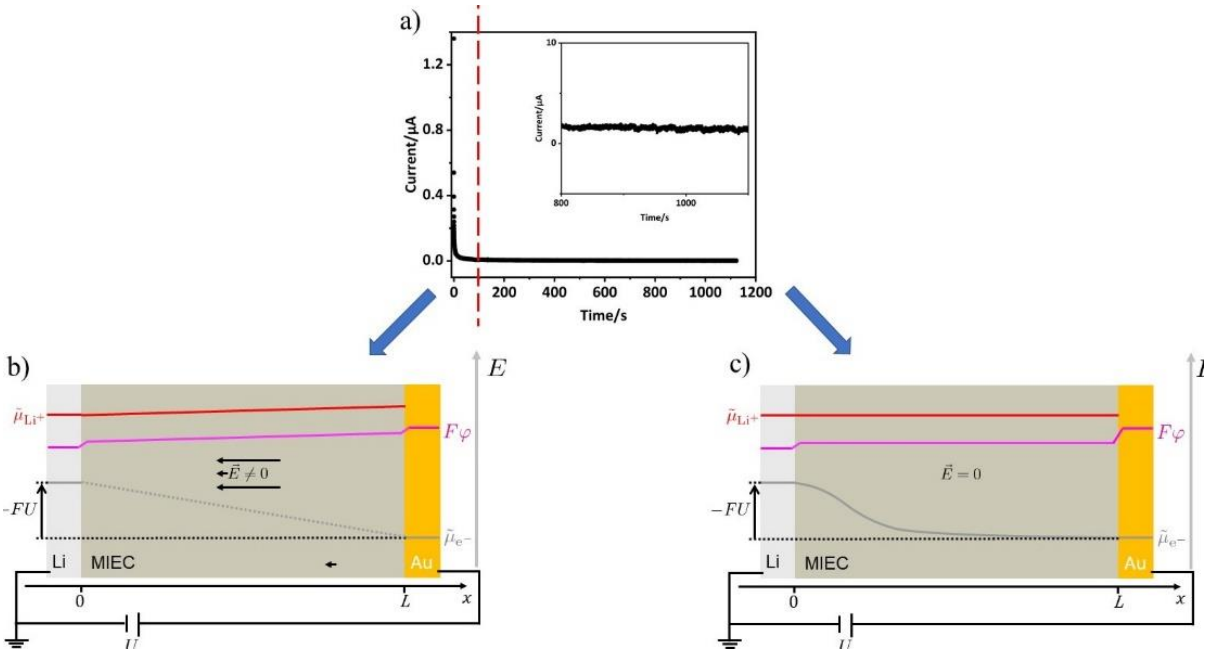

Figure 2.4 a Current change in MIEC with time after a positive potential is applied on irreversible electrode in HWC. **b** Schematic of different potentials across the whole HWC after the positive potential just being applied on irreversible electrode. **c** Schematic of different potentials across the whole HWC when the HWC reaches to stable state after the positive potential being applied on irreversible electrode.

2.5 KPFM measurements on Hebb Wagner cell

In our KPFM measurements on HWC, we choose HWC Li|Li_3PO_4|Au as a model system. Here Li is reversible electrode, Au is irreversible electrode and Li_3PO_4 is MIEC. For Li_3PO_4, it is a good Li ionic conductor with very low electronic conductivity[21,22]. Li electrode is connected to ground and electrically connected to KFPM tip.

Then external potential of 0.5V, 0.75V, 1.00V, 1.25V and 1.50V were applied on Au electrode in HWC. After the HWC reaching stable state – no ion current but only constant electron current in Li_3PO_4 under certain applied potential. This stable state of HWC is also a kind of non-equilibrium state because there is electron electrochemical potential gradient in Li_3PO_4

even though there is no Galvani potential gradient in Li_3PO_4. Further, the gradient of electron electrochemical potential increases with applied potential (Figure 2.5a). This means electrons/holes concentration gradient along Li_3PO_4 increases with applied potential thus surface potential gradient of Li_3PO_4 increases with applied potential.

After reaching to stable state, KPFM measurements were applied on HWC cross-section. For Li reversible electrode, the measured CPD value is constant because Li electrode is connected to ground and work function of Li is constant. For Au irreversible electrode, the measured CPD increases with applied external potential and the increased value almost equals to applied external potential (Figure 2.5b). For Au, the surface potential is constant because its composition does not change. Based on equation 8, we can decide that measured CPD change is only related with Galvani potential change. Also Galvani potential change in Au electrode equals to the change of electrochemical potential of electron. From the experimental results that the measured CPD changes on Au layer roughly equal to the corresponding applied external potentials on Au electrode, we can verify our explanation on metal or semiconductor that measured CPD by KPFM equals Galvani potential change.

For Li_3PO_4, the internal gradient of electrochemical potential/chemical potential of electrons increases with applied potential on Au electrode after reach to non-equilibrium stable state while the internal Galvani potential is constant and does not change with applied potential on Au electrode (Figure 2.5a). Our KPFM measurements on Li_3PO_4 layer show a constant CPD value across the whole Li_3PO_4 layer and CPD value does not change with applied external potential, which is the same as Li_3PO_4 Galvani potential that is constant across the whole Li_3PO_4 layer and does not change with applied external potential after reaching to steady state. This result confirms our speculation above from theoretical analysis that measured CPD signal change in MIEC under non-equilibrium state is mainly related with Galvani potential change. Furthermore, this result exclude the possibility that CPD change in MIEC layer is related with electrons electrochemical potential change.

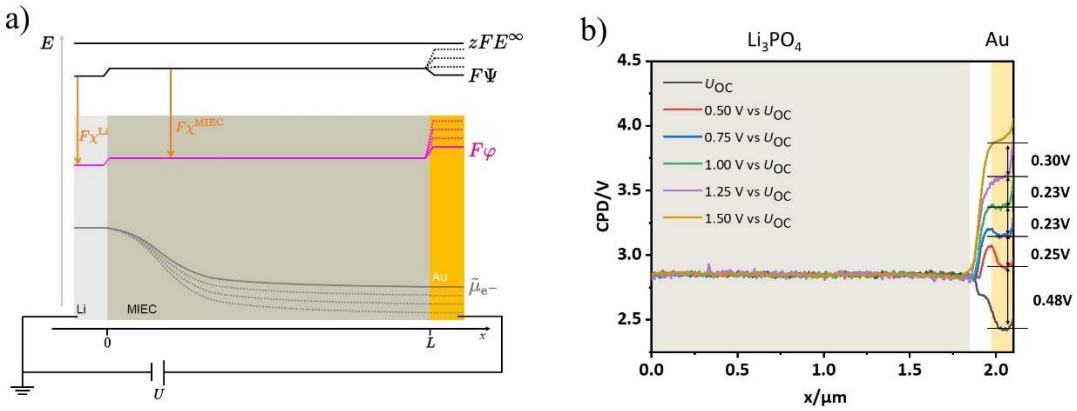

Figure 2.5 a Schematic of different potentials across the whole HWC when the HWC reaches to stable state after different positive potentials being applied on irreversible electrode Au electrode. **b** Measured CPD profiled across the whole HWC in steady state after different positive potentials being applied on irreversible Au electrode.

To further prove that measured CPD change on Li_3PO_4 in HWC is only related with Li_3PO_4 Galvani potential change, we switched the applied external positive potential from Au irreversible electrode to Li reversible electrode. Now Li ions can continuously move from Li electrode to Au electrode in Li_3PO_4 because Li electrode can provide continuous Li ions for Li_3PO_4. At Au electrode side, Li continuously reacts with Au to form Li_xAu alloy under the external potential. Under this situation, Galvani potential gradient in Li_3PO_4 layer is constant after reaching to steady state as Figure 2.6a shows. At the same time, electrons move from Li_xAu electrode to Li electrode because of the electrons electrochemical potential gradient in Li_3PO_4 layer (Figure 2.6a). Figure 2.6b shows the measured CPD profile along Li_3PO_4 surface under non-equilibrium state after 300mV external potential being applied on Li reversible electrode. We can observe that CPD profile in Li_3PO_4 layer shows linear decrease from Li electrode to Au electrode. The linear decrease of measured CPD in Li_3PO_4 from the side close to Li electrode to Au electrode is the same with Li_3PO_4 internal Galvani potential (Figure 2.6a). Both measured CPD and Galvani potential are constant everywhere respectively in Li_3PO_4 layer before external potential applied. The around 200mV measured CPD decrease in Li_3PO_4 from the side close Li electrode to Au electrode is smaller than applied external potential 300mV. This results from high interfacial resistance in Li| Li_3PO_4 and Li_3PO_4|LixAu interfaces, which share part of the applied potential.

Overall, this experiment further proves that measured CPD change on Li_3PO_4, a kind of MIEC, is related with internal Galvani potential change but not related with electrochemical potential change of electrons in Li_3PO_4.

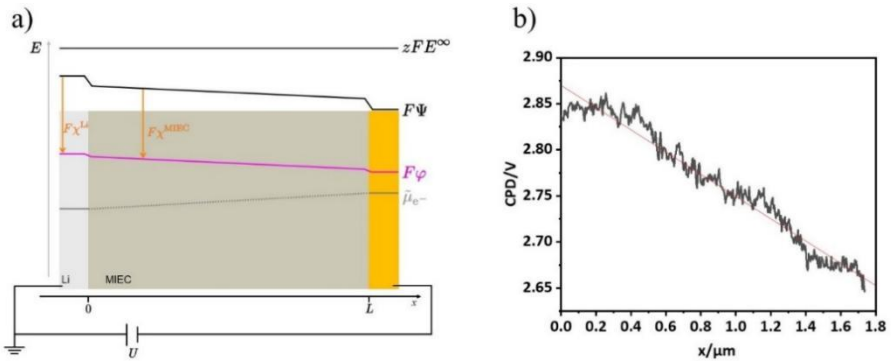

Figure 2.6 a Schematic of different potentials across the whole HWC when the HWC reaches to stable state after a positive potential being applied on reversible electrode Li electrode. **b** Measured CPD profiled across the LPO MIEC layer in steady state after a positive potential being applied on reversible Li electrode.

2.6 Conclusion

In this work, we firstly clarify different kinds of potential from electrochemist view, which are often confused for people with different background because of professional language barrier. This clarification is important and necessary on analyzing the origin of CPD signal change measured by KPFM. Then from the working theory explanation of KPFM on different kinds of sample, including metal/semiconductor and MIEC, we theoretically analyze that sample's Galvani potential change decides the CPD change of the sample measured sample with KPFM under non-equilibrium state compared with equilibrium state. To verify our conclusion, we choose HWC as a research target system. The results of operando KPFM carried on HWC cross-section with different external potential applied on HWC after reaching to steady state, we prove the correction of our conclusion CPD change on MIEC under non-equilibrium state in only related with MIEC internal Galvani potential change.

2.7 Experiment

2.7.1 Sample preparation of the WHC

For the assembly of the Li_3PO_4 Wagner-Hebb cell, an aluminum oxide single crystal with (0001) orientation was used. The gold electrode was fabricated by DC magnetron sputtering onto the substrate. It was performed with a power of 30 W and an argon partial pressure of 0.5 Pa. The resulting electrode had a thickness of ≈ 100 nm. Afterward, the sample was annealed at 600 °C in a vacuum ($< 10^{-5}$ Pa). After the sample being cooled to room temperature, the Li_3PO_4 layer was fabricated by radio frequency magnetron sputtering. It was conducted with a power of 100 W and an argon partial pressure of 0.15 Pa. The resulting Li_3PO_4 layer had a thickness of ≈ 1 µm. The Li electrode was obtained via thermal evaporation. The electrode had a thickness of ≈ 1 µm. The detailed sample preparation was described by Kobayashi *et al*.

2.7.2 HWC cross section preparation

Cross section of the thin-film samples were prepared using the argon-ion milling system IM4000 Plus from Hitachi with the air-protection unit to reduce topographical crosstalk. For polishing via argon-ion beam, a titanium mask was used to protect the sample from unintentional beam irradiation and to create a flat shadow from the ion beam. The acceleration voltage was set to ≈ 2 V. The discharge voltage was set to ≈ 1.5 kV with a discharge current of ≈ 450 µA. The gas flow was set to ≈ 0.1 cm^3/min. The tilt angle was set to ≈ 90°. During this program, the stage on which the sample holder was mounted rotated $\pm 30°$ clockwise and counterclockwise with 30 reciprocations per minute. The polishing time was ≈ 24 h. To prevent degradation of the sample, transportation between the glove box and the ion milling system was conducted via a transfer chamber under inert atmosphere.

2.7.3 HWC electrochemical measurements

The measurements were conducted in a glove box from GS-systems with a controlled atmosphere of argon (purity: 99.9999% from Air Liquide). Traces of oxygen and water were controlled continuously: < 0.5 ppm of O_2, < 0.4 ppm of H_2O. For monitoring the electronic current and applying a voltage to the sample the potentiostat SP-150 from BioLogic was used.

For the connection of the cells, the CE to ground configuration in the potentiostat was used. In this setup, the counter electrode (lithium electrode) was connected to the grounding and was therefore the reference electrode. A potential difference was applied to the working electrode (gold electrode).

2.7.4 KFPM measurements on HWC

KPFM measurements were conducted via the MFP 3D from Asylum Research. For the lock-in detection required for KPFM, the lock-in amplifier HF2 from Zurich was used. For each measurement, the n-doped (Sb) Silicon cantilevers plated with a platinum-iridium alloy for electric conductivity with the designation *SCM-PIP-V2* from *Bruker* were used. The nominal first resonance frequency was ω_0 = 75 kHz.

2.8 Statement of contribution

Rüdiger Berger, Jügen Janek and Chao Zhu conceived the idea. Franjo Weber and Chao Zhu performed argon ion milling polishing and KPFM measurements. Shigeru Kobayashi prepared Hebb Wagner cell. Franjo Weber performed data collection and analysis. Franjo Weber and Chao Zhu wrote the manuscript. Jügen Janek, Rüdiger Berger provided expertise, electrochemical input, feedback and revised the manuscript.

2.9 Reference

1 Melitz, W., Shen, J., Kummel, A. C. & Lee, S. Kelvin probe force microscopy and its application. *Surf. Sci. Rep.* **66**, 1-27 (2011).

2 Nonnenmacher, M., o'Boyle, M. & Wickramasinghe, H. K. Kelvin probe force microscopy. *Appl. Phys. Lett.* **58**, 2921-2923 (1991).

3 Böhmisch, M. *et al.* Atomic force microscope based Kelvin probe measurements: application to an electrochemical reaction. *J. Phys. Chem. B* **101**, 10162-10165 (1997).

4 Sharma, A. *et al.* Nanoscale heterogeniety and workfunction variations in ZnO thin films. *Appl. Surf. Sci.* **363**, 516-521 (2016).

5 Masuda, H., Ishida, N., Ogata, Y., Ito, D. & Fujita, D. Internal potential mapping of charged solid-state-lithium ion batteries using in situ Kelvin probe force microscopy. *Nanoscale* **9**, 893-898 (2017).

6 Weber, S. A. *et al.* How the formation of interfacial charge causes hysteresis in perovskite solar cells. *Energy Environ. Sci.* **11**, 2404-2413 (2018).

7 Masuda, H., Matsushita, K., Ito, D., Fujita, D. & Ishida, N. Dynamically visualizing battery reactions by operando Kelvin probe force microscopy. *Commun. Chem.* **2**, 140 (2019).

8 Fuller, E. J. *et al.* Spatially resolved potential and li-ion distributions reveal performance-limiting regions in solid-state batteries. *ACS Energy Lett.* **6**, 3944-3951 (2021).

9 Lange, E. Über elektrochemische Grundbegriffe, insbesondere der Elektrode Metall/Lösung. *Zeitschrift für Elektrochemie und angewandte physikalische Chemie* **55**, 76-92 (1951).

10 Örnek, C., Leygraf, C. & Pan, J. On the Volta potential measured by SKPFM–fundamental and practical aspects with relevance to corrosion science. *Corros. Eng. Sci. Technol.* **54**, 185-198 (2019).

11 Wurfel, P. The chemical potential of radiation. *J. Solid State Phys.* **15**, 3967 (1982).

12 Bockris, J. O. M., Reddy, A. K. & Gamboa-Aldeco, M. E. *Modern electrochemistry 2B: electrodics in chemistry, engineering, biology and environmental science*. Vol. 2 (Springer Science & Business Media, 1998).

13 Scholz, F. Books on fundamental electrochemistry and electroanalytical techniques. *Electroanalytical Methods: Guide to Experiments and Applications*, 343-345 (2010).

14 Gellings, P. J. *Handbook of solid state electrochemistry*. CRC Press (2019).

15 Bergveld, P., Hendrikse, J. & Olthuis, W. Theory and application of the material work function for chemical sensors based on the field effect principle. *Meas. Sci. Technol.* **9**, 1801 (1998).

16 Huggins, R. *Advanced batteries: materials science aspects*. Springer Science & Business Media (2008).

17 Axt, A., Hermes, I. M., Bergmann, V. W., Tausendpfund, N. & Weber, S. A. Know your full potential: Quantitative Kelvin probe force microscopy on nanoscale electrical devices. *Beilstein J. Nanotechnol.* **9**, 1809-1819 (2018).

18 Hebb, M. H. Electrical conductivity of silver sulfide. *J. Chem. Phys.* **20**, 185-190 (1952).

19 Janek, J. & Korte, C. Electrochemical blackening of yttria-stabilized zirconia–morphological instability of the moving reaction front. *Solid State Ion.* **116**, 181-195 (1999).

20 Riess, I. I− V relations in semiconductors with ionic motion. *J. Electroceramics* **17**, 247-253 (2006).

21 Kobayashi, S. *et al.* Drastic Reduction of the Solid Electrolyte–Electrode Interface Resistance via Annealing in Battery Form. *ACS Appl. Mater. Interfaces* **14**, 2703-2710 (2022).

22 Zhou, A. *et al.* Improved high-voltage and high-temperature electrochemical performances of $LiCoO_2$ cathode by electrode sputter-coating with Li3PO4. *J. Power Sources* **322**, 10-16 (2016).

Chapter 3 Understanding the evolution of lithium dendrites at $Li_{6.25}Al_{0.25}La_3Zr_2O_{12}$ grain boundaries via operando microscopy techniques

3.1 Introduction

Grain boundaries, which are the transition regions between different grains, often have different properties than the grains themselves[1,2]. Many researchers have observed that lithium dendrites tend to spread in grain boundaries of garnet-type solid electrolytes[3-6] such as $Li_7La_3Zr_2O_{12}$ based electrolyte. Garnet-type solid electrolytes are used in solid-state batteries, which are attractive next-generation energy storage devices[7-10]. In most cases, there are no obvious physical spaces or voids at grain boundaries available for lithium penetration[11-13], garnet-type solid electrolytes form a stable interface in contact with lithium metal[14], have a wider electrochemical stability window[15] and greater mechanical strength[16] than other types of solid electrolytes. However, the lithium dendrite penetration into garnet-type solid electrolytes limits further application. *Ex situ* observations[11], density functional theory (DFT) or physical field-based simulations[17-20] and microscopic electrochemical test methods[21,22] have been used to characterize lithium-ion transport, lithium-dendrite nucleation and lithium-dendrite growth at grain boundaries in garnet-type solid electrolytes. Unfortunately, the conclusions drawn from those experiments are contradictory, and the role played by grain boundaries in lithium-dendrite nucleation and growth is not yet clear[23,24]. Lu et al. concluded that grain boundaries have low lithium ion conductivity[25], which blocks ion transport and leads to the formation of “hot spots” for lithium-dendrite nucleation in LLZO due to a local variation of current density. In contrast, Cheng et al. reported that grain boundaries have a higher ionic conductivity than bulk grains[21]. Moreover, Song et al. reported that a higher electronic conductivity at grain boundaries compared to that of bulk grains is responsible for lithium dendrite nucleation at grain boundaries[26]. In summary, it is not evident whether high or low ionic conductivity or even the electronic properties at grain boundaries play the determining role in lithium nucleation. Furthermore it is unclear how subsequently dendritic

growth is promoted. In order to address both issues high spatial resolution methods are beneficial.

Recently, researchers tried to use high-resolution techniques to characterize grain boundaries. Liu et al. analyzed the electronic band structure of grain boundaries with electron energy loss spectroscopy using high-resolution transmission electron microscopy[27]. They found that half of the grain boundaries exhibited a smaller band gap, which may serve as channels for an electron leakage currents. This finding hints that electron leakage currents in devices might play role for dendritic growth. However, electron microscopy methods typically cannot be used to study nano-scale electrical processes in operating device, i.e. during battery charging or discharging. Here, techniques featuring high spatial resolution characterization in real-world battery operation conditions are beneficial for understanding the dynamics of preferential lithium nucleation and growth in grain boundaries. In order to trace the relevant processes in solid-state batteries, all electrical functions of the solid electrolyte must be preserved. In recent years, our group developed high-resolution Kelvin probe force microscopy (KPFM) and time-resolved electrostatic force microscopy (tr-EFM) based on scanning force microscopy (SFM), which enabled us to track potential changes with nanometer-scale lateral resolution and compare ion mobility with microsecond-scale temporal resolution[28-30]. Both techniques hold the key to understanding the dynamics of preferential lithium penetration in grain boundaries for measurements in an inert atmosphere.

To clarify the role of different ionic or electronic properties in lithium nucleation and the subsequent promotion of dendritic growth in grain boundaries, we used cubic phase $Li_{6.25}Al_{0.25}La_3Zr_2O_{12}$ (LLZO) as a model solid electrolyte while pure $Li_7La_3Zr_2O_{12}$ is typically not cubic and not well ion-conducting[31] $Li_{6.25}Al_{0.25}La_3Zr_2O_{12}$ is widely accepted as representative material for LLZO based garnet-type solid electrolyte. We then prepared symmetric Li|LLZO|Li cells to investigate their nanometer-scale local electronic properties. We found a local Volta potential drop at grain boundaries in LLZO near the lithium counter-electrode (Li-CE, plating side), which probably indicates that a Galvani potential drop formed there. With complementary measurements performed with tr-EFM and electron-beam injection, we associate this time-dependent potential drop to the preferential accumulation of electrons at

grain boundaries near the plating side, which allows lithium ions to be reduced locally. Based on these findings, our model explains the favored deposition of lithium metal in grain boundaries of garnet-type solid electrolytes and subsequent dendrite growth.

3.2 Operando KPFM measurements

X-ray diffraction was used to ensure cubic phase purity of LLZO(Figure 3.1a). Electrochemical impedance spectroscopy results show that grain boundaries in LLZO add resistance to the ceramic material (Figure 3.1b).

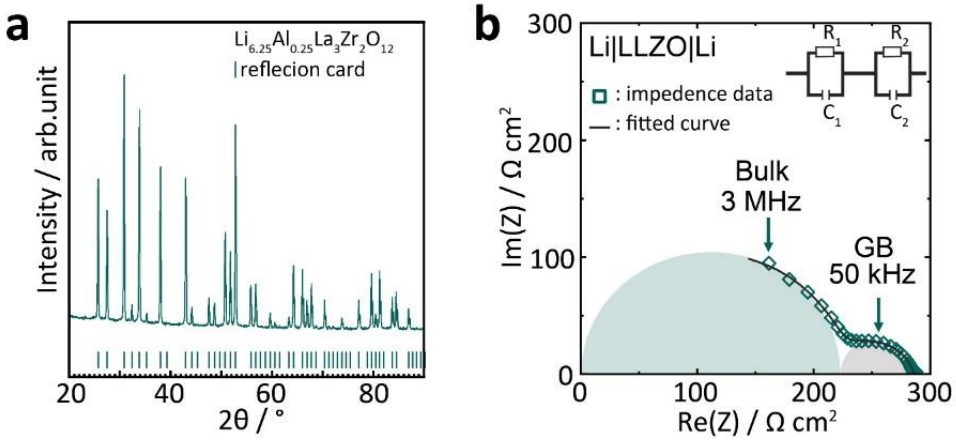

Figure 3.1 a X-ray diffractogram of the herein prepared LLZO displayed together with a reflection card of said phase[32]. No impurities or other crystalline phases are observed. **b** Nyquist-Plot of herein prepared Li|LLZO|Li cell showing only bulk and grain boundary contribution to the transport, as the interfacial resistance is negligible.

To probe variations of the local electric properties of LLZO, we performed *operando* KPFM measurements at different positions along the LLZO surface of a symmetric Li|LLZO|Li cell (P0 to P10 in Figure 3.2a). Our KPFM measurements were performed first at open circuit voltage (OCV) and then with a constant current density of 0.1 mA cm^{-2}, 0.25 mA cm^{-2} and 0.5 mA cm^{-2} applied to the cell, respectively. Lithium was then stripped from the lithium working electrode (Li-WE) and plated at the Li-CE. The corresponding potential applied to the Li-WE (ϕ_{applied}) relative to the grounded Li-CE was almost constant (Figure 3.2b).

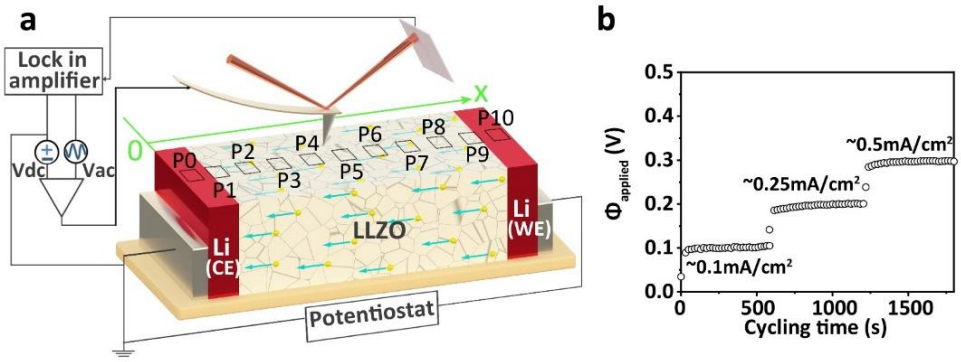

Figure 3.2 a Schematic of KPFM on the LLZO surface of a symmetric Li|LLZO|Li cell. The cell was cycled via a potentiostat. **b** Cycling performance of the symmetric Li|LLZO|Li cell with potentials of 100, 200 and 300 mV applied to the Li-WE at the set constant current densities of 0.1 mA/cm^2, 0.25 mA/cm^2 and 0.5 mA/cm^2.

Broken samples exhibited a rough surface thus causing a crosstalk with the measured contact potential difference (CPD) signal between SFM tip and sample by KPFM. The latter reduced the lateral resolution. Therefore, we polished the surfaces by argon-ion milling. The average CPD value of a freshly broken LLZO and an argon-ion milled surface did not change. Thus the surface properties of LLZO were not altered by polishing (Figure 3.3).

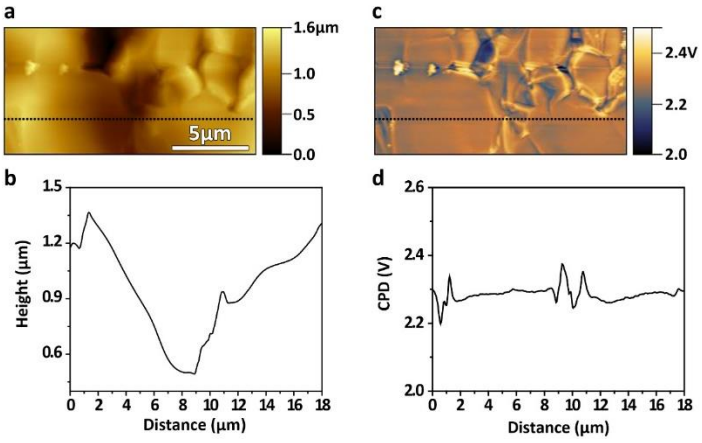

Figure 3.3 We obtained the LLZO sample by breaking the cell into two pieces in argon filled glovebox. Directly afterwards we did KPFM measurements on the cross section in the same argon filled glovebox. The KPFM measurement shown was taken 5 min after breaking the cell. **a** Topography of the LLZO cross section. **b** Topography line profile along the dotted line indicated in **a**. **c** Simultaneous obtained CPD map of the same area as shown in **a**. **d** CPD line profile along the dotted line indicated in **c.**

KPFM measurements at OCV conditions: At OCV the topography of the Li-CE|LLZO interface (P1 in Figure 3.2a) exhibits a contrast due to different etching rates during argon-ion polishing, which allows us to distinguish the Li-CE from the LLZO (Figure 3.4). Even more clearly, the two materials can be distinguished in the measured CPD image (Figure 3.4). The Li-CE features a lower CPD value (≈2.1 V) compared to LLZO (≈2.35 V).

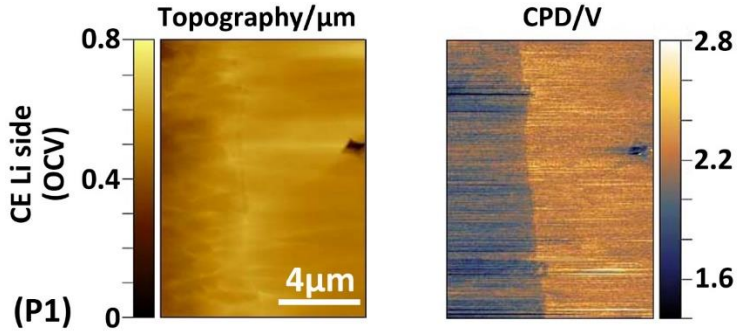

Figure 3.4 Topography images and the corresponding CPD maps at P1 in Figure 3.2a of OCV state of the symmetric Li|LLZO|Li cell.

KPFM measurements under current load – Plating side (CE): A constant current density of approximately 0.5 mA cm^{-2} applied to the symmetric Li|LLZO|Li cell leads to an increase of the voltage difference of 300 mV, which caused lithium stripping from the Li-WE and plating at the Li-CE. The volume of the Li-CE increased, manifested by a change in topography adjacent to the LLZO interface. On top of the Li-CE we measured protrusions with a height of 300 nm for a plating time of 30 minutes (Figure 3.5). Even though the Li-CE was grounded, the measured CPD value increased slightly by 50 – 80 mV. This increase in CPD scales with the magnitude of the applied potential and was observed only on the Li-CE surface near the Li-CE|LLZO interface. We attribute this slight increase to the presence of a thin lithium-ion conducting passivation layer on the lithium-metal cross section[33], which formed after breaking the Li|LLZO|Li cell and subsequently polishing it, owing to the high reactivity of lithium metal.

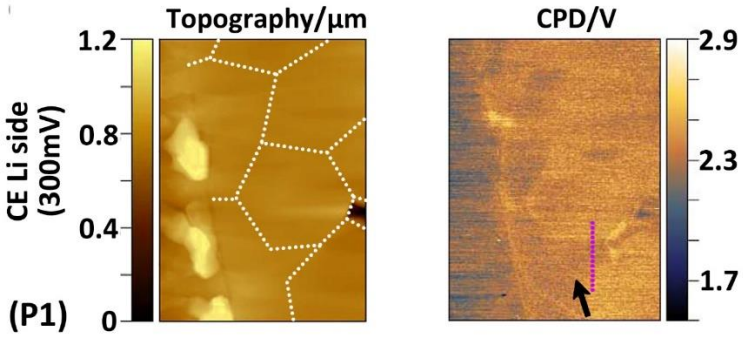

Figure 3.5 Topography images and the corresponding CPD maps at P1 in Figure 3.2a of lithium plating at the Li-CE with a potential difference of 300 mV between the two electrodes of the symmetric Li|LLZO|Li cell.

On the LLZO surface near the interface with the Li-CE, the measured CPD values are 80 – 100 mV lower in some areas than in neighboring regions after a plating time of 30 minutes (dark arrow in Figure 3.5). These areas are distributed unevenly and are located at the Li-CE|LLZO interface, but are also found a few micrometers away from the interface. Based on the shape of defects measured in topography and the CPD map of the same LLZO region in the OCV state, we attribute these low equipotential areas to originate from grain boundaries (dotted white line in Figure 3.5). We measured CPD difference $\Delta\mathrm{CPD} = \mathrm{CPD}_{\text{low CPD area}} - \mathrm{CPD}_{\text{high CPD area}}$ along the dotted purple line in Figure 3.5 decreases with plating time (Figure 3.6). In addition, the width of the low equipotential areas along grain boundaries in the CPD maps increases continuously (Figures 3.6).

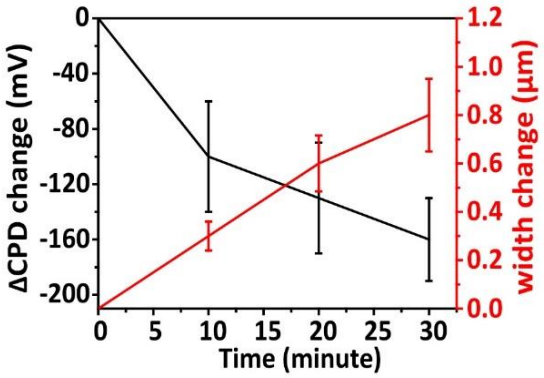

Figure 3.6 Measured ΔCPD and width change as a function of time under 300 mV for the region along dotted purple line in CPD maps in Figure 3.5.

In addition, we observe a very light bright contrast at very few grain boundaries in Figure 3.5b that can indicate locally a slightly lower work function. We hypothesize that a bipolar polarization effect leads to reversible chemical polarization at grain boundaries that are crossed by the ionic current. As proven first by Reitz et al[34] and later demonstrated for Li systems by Liu et al.[35], local electronically conducting regions can "shortcut" the ionic current and lead to chemical polarization. This is a local effect within the grain boundary, which explains only the local very light bright contrast. However, it does not explain the key observation, which is the step-like CPD signal on most grain boundaries close to Li-CE.

There are two possible explanations for the step-like decrease in CPD for some grains compared with other grains with increasing plating time. On the one hand, a lower CPD value for some grains may indicate their change of the work function due to an irreversible decomposition or a lithium reduction in those grains. In that case, $\Delta\mathrm{CPD}$ would persist after switching ϕ_{applied} back to 0. On the other hand, a lower CPD of those particular grains may indicate a drop of the local Galvani potential at grain boundaries to neighboring grains. In that case, $\Delta\mathrm{CPD}$ would be reversible and return to 0 after ϕ_{applied} is switched back to 0. To check whether these changes in CPD at grain boundaries were transient or permanent, we set the external current to 0 (ϕ_{applied} = 0). Now, the CPD map (Figure 3.7) again resembles the one measured initially at OCV (Figure 3.4). However, the lithium protrusions owing to plated lithium on top of the lithium electrode remained. Therefore, we attribute the $\Delta\mathrm{CPD}$ for ϕ_{applied} > 0 to a drop of the Galvani potential at grain boundaries near the Li-CE|LLZO interface.

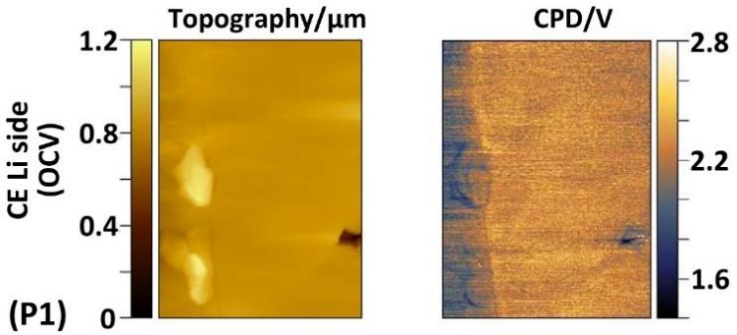

Figure 3.7 Topography images and the corresponding CPD maps at P1 in Figure 3.2a of relaxed and re-equilibrated state after removing external potential on the symmetric Li|LLZO|Li cell.

KPFM measurements under current load – stripping side (WE): To investigate the Li-WE side (P9 in Figure 3.2a), we kept the SFM tip at the same scan area but switched the connectors of the potentiostat. This turned the original Li-WE into the grounded Li-CE and the former Li-CE into the new Li-WE. Upon applying an external current equivalent to a cell applied potential of 300 mV, we found that the CPD on top of the Li-WE increased by 300 mV. Under this condition, lithium ions are now stripped from the new Li-WE. The CPD value of the LLZO near the Li-WE|LLZO interface increased by approximately 200 mV. This increase was less than the 300 mV equivalent external potential applied to the Li|LLZO|Li cell. We attribute the difference in potential to a high interface resistance of Li|LLZO due to a degrading physical contact for an extended cycling duration (Figure 3.8)[36,37]. More importantly, close to the Li-WE side, we observed no drop of Galvani potential at grain boundaries.

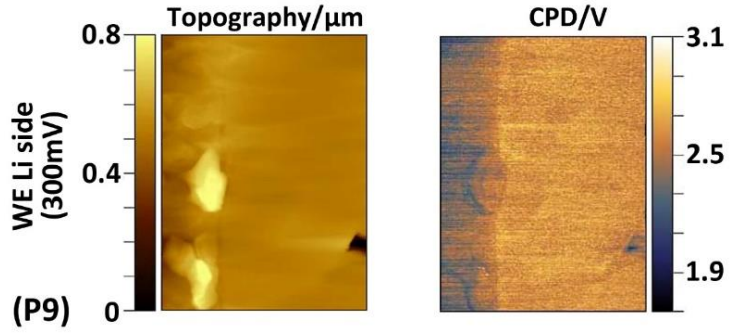

Figure 3.8 Topography images and the corresponding CPD maps at P9 in Figure 3.2a of lithium plating at the Li-CE with a potential difference of 300 mV between the two electrodes of the symmetric Li|LLZO|Li cell.

KPFM measurements under current load – Grain boundaries: If there is only a uniform LLZO bulk resistance, the gradient of the Galvani potential, $\partial\phi/\partial x$, in LLZO will be constant across the LLZO for ϕ_{applied} > 0. Thus, the measured CPD will decrease linearly in LLZO from the Li-WE to the Li-CE. Therefore, the measured CPD drop at grain boundaries close to Li-CE indicates the presence of a "space charge layer". Two scenarios could be the origin of a "space charge layer" at grain boundaries near the Li-CE at which lithium is being plated: The first scenario is that grain boundaries act as a potential barrier for lithium ions owing to different transport properties of lithium ions. The presence of a barrier causes lithium ions to accumulate close to grain boundaries. Local charge neutrality is then achieved by electrons at grain boundaries. In this case, lithium ions and electrons form a space charge layer, which then partially shields the external electric potential (Figure 3.9a). However, in this situation, Galvani potential drops at grain boundaries should be independent from the position of the grain boundary, and should not only be observed close to the Li-CE. The second scenario is that the formation of a space charge layer results from different electronic conduction properties at the grain boundaries compared to in-grain parts (Figure 3.9b). Even though we regard LLZO as a pure ionic conductor (≈10^{-4} S cm^{-1}), it also exhibits a low electronic conductivity of ≈10^{-7} – 10^{-11} S cm^{-1} [31,38].

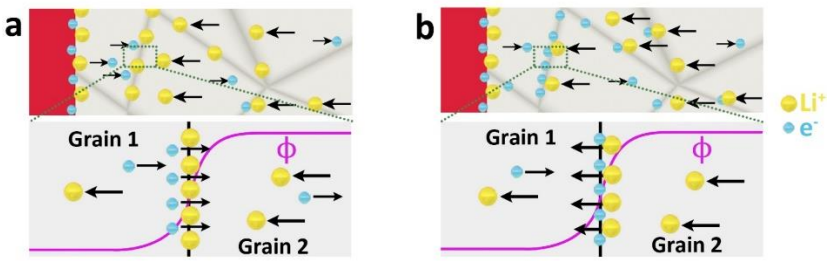

Figure 3.9 a and **b** are two hypothetical scenarios for the formation of a "space charge layer" at grain boundaries. Scenario **a** results from different conduction properties of lithium ions and scenario **b** results from different conduction properties of electrons at grain boundaries, respectively.

KPFM measurements under current load – LLZO surface far from lithium electrodes: To further prove which scenario can correctly explain the observed Galvani potential drop at grain

boundaries close to Li-CE, we performed KPFM measurements at other areas (P0, P2–P8, P10 in Figure 3.2a) under an applied potential of 300 mV to the WE in the symmetric cell Li|LLZO|Li. Then we plotted the factor k(x)

$$k(x) = \frac{CPD(x)_{\text{applied}} - CPD(x)_{\text{OCV}}}{\phi_{\text{applied}}} \quad (1)$$

where *x* is the distance between a LLZO surface point and the Li-CE, $CPD(x)_{\text{OCV}}$ is the CPD value of the LLZO surface point in the OCV state. $CPD(x)_{\text{applied}}$ is the CPD value of the LLZO surface point with an applied potential ϕ_{applied} on cell (Figure 3.10). The plot indicates distinct areas: the two interfaces of the lithium electrodes where k changes by 0.3 - 0.4. These step-like changes at both Li|LLZO interfaces indicate a higher interface resistance due to a poor physical contact[32,36,39,40]. The inner part of LLZO far from the interfaces exhibits a change of k from ≈0.3 to ≈0.6 at a constant slope of ≈0.15 mm^{-1}. The constant slope of k indicates that a constant electric field acts along the bulk LLZO. Interestingly, grain boundaries in bulk LLZO show a different behavior compared to grain boundaries close to Li-CE, where a significant electrical field change was detected.

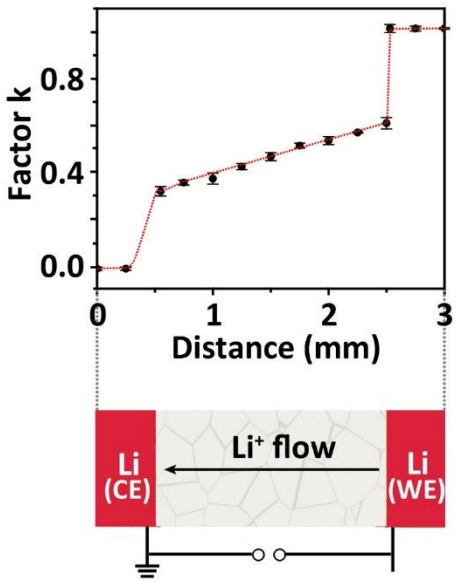

Figure 3.10 a Factor k evaluated at different points on Li|LLZO|Li surfaces at 300 mV potential difference between the two electrodes. The error bars corresponds to three independent experiments.

In order to study grain boundaries far from both Li-CE and Li-WE in more detail, we zoomed the KPFM measurement to position P3 (0.5 mm from the Li-CE and 1.5 mm from Li-WE, see Figure 3.11a), where the topography image showed no voids or defects (Figure 3.11b). The corresponding CPD mapping shows a difference between in-grain parts and grain boundaries (Figure 3.11c). Average line profiles in topography and CPD along the direction of the arrow in the two regions CP1 and CP2 (purple rectangular wireframe) show no correlation between the topography and the measured CPD (Figures 3.11d and 3.11e). Both CP1 and CP2 contain two different grains and one grain boundary, respectively. Different grains show CPD differences of several tens of millivolts. We attribute this difference to the different crystal orientation or local impurities[41,42]. Next, we applied different constant external current densities to the Li|LLZO|Li cell, resulting in different potential ϕ_{applied} applied to the WE. Now the average CPD surface profiles (CP1 and CP2), which are always recorded at the same position, shifted by approximately 50, 85 and 112 mV at a corresponding ϕ_{applied} of 100, 200 and 300 mV, respectively (Figures 3.11d and 3.11e). In particular, the CPD differences between two grains in CP1 are approximately 24, 22 and 25 mV at 100, 200 and 300 mV, respectively. Thus, the CPD difference between the two grains remains constant and unaffected by ϕ_{applied}. The second CPD line profile CP2 follows a profile that is almost perpendicular to CP1. Thus, a potential directional dependence is prevented in this way. Thus, there is no obvious drop of electric potential at grain boundaries in this region and consequently no ion-barrier.

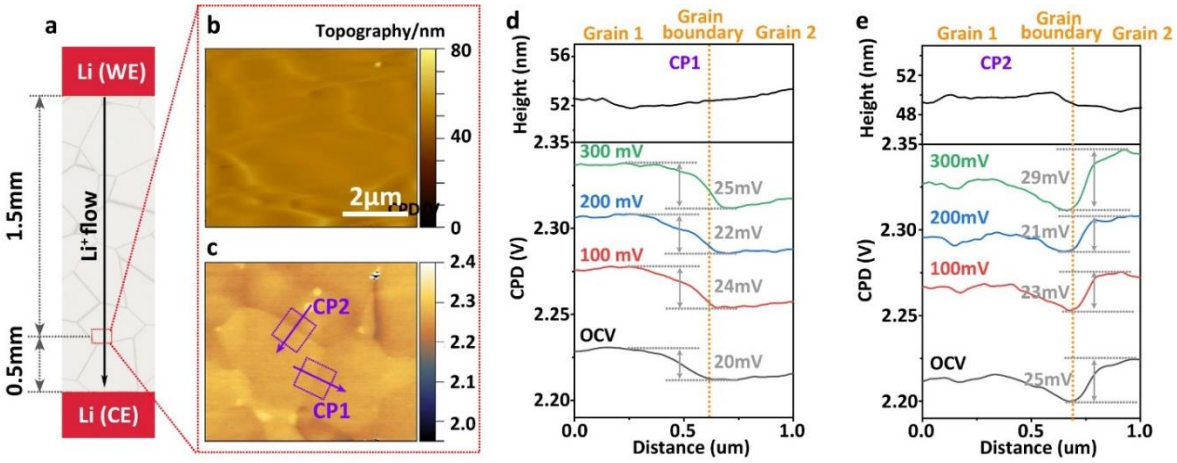

Figure 3.11 a Schematic diagram of the position of the KPFM measurement on the LLZO surface. **b** and **c** Topography and CPD maps (6 µm× 5 µm) of the regions within the dashed boxes in **a** in an OCV state. **d** and **e** Averaged line profiles of the topography and CPD extracted from areas CP1 and CP2 in the direction of the arrow under different potentials applied to the WE, respectively.

In summary, KPFM measurements show that drops in Galvani potential take place only at grain boundaries near the Li-CE, where lithium is being plated. Thus, the first possibility that grain boundaries might feature in general different ionic transport properties (Figure 3.9a) is unlikely. This conclusion is further supported by time-resolved electrostatic force microscopy (tr-EFM), which we will present in the next section. The latter finding indicates that we need to consider different electron transports properties in grain boundaries compared to the grain bulk (Figure 3.9b). The important role of electrons will be proven by additional electron beam injection measurements (elect-beam injection section).

3.3 Time-resolved EFM

In tr-EFM, lithium ions are moved by the electric field emanating from the SFM tip due to an additional DC voltage (Figure 3.12a). Once the DC voltage is switched off, the additional electric field of the tip is removed and the mobile ions return back into an equilibrium state (Figure 3.12b). The tr-EFM method has previously been used to investigate time-resolved ion dynamics in ion-conducting materials[43-45]. Here, we compare lithium ion relaxation processes between grain boundaries and in-grain parts[46,47].

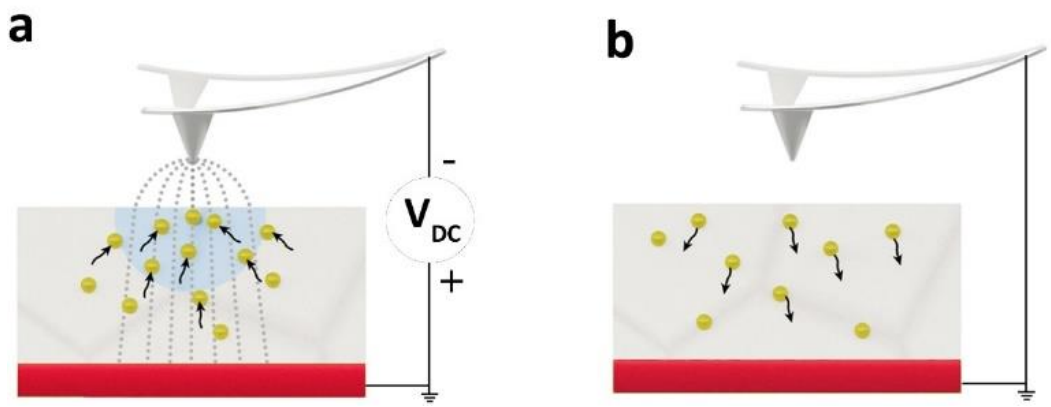

Figure 3.12 Schematic illustration of the principle of tr-EFM on LLZO. **a** DC voltage is applied on tip to attract lithium ions in LLZO. **b** DC voltage is removed and lithium ions in LLZO relax to equilibrium state.

For tr-EFM, we chose an area on the LLZO surface within 500 nm distance from the Li-CE that contains different grains, grain boundaries and voids (Figure 3.13a). KPFM results show that the grain boundary has an about 40 mV lower CPD value than in-grain areas (Figure 3.13b). The voids show CPD values some 100 to 200 mV lower than in-grain areas. We attribute these lower CPD values to a Li_2CO_3 layer that formed in voids during prolonged storage of LLZO samples or during the sintering.

The tr-EFM measurement was performed in an area of 400 nm × 200 nm marked by a purple rectangle in Figure 3.13c. This area was uniformly divided into 20 × 10 pixels. At each pixel, we fitted the curve of SFM tip amplitude change at secondary resonance frequency vs. time under lithium ions relaxation process with stretched-exponential function to obtain lithium ions relaxation time constant τ (Figure 3.13c) (more details in experiment section). The void corresponds to τ values of (296 ± 40) ms, and all other areas correspond to values of (166 ± 20) ms. In particular, there is no difference between the grain boundary and the in-grain area. For example, the amplitude shift vs time dependence of three points at the in-grain region P_1, the grain boundary P_2 and the defect/void P_3 are plotted in Figure 3.13d. The changes in measured amplitude as a function of time overlap at P_1 and P_2. Thus, we conclude that the grain boundary near Li-CE and the in-grain areas in LLZO have similar ion diffusivities as other grain boundaries in another part of LLZO. In other words, grain boundaries do not provide obvious faster or slower ion conduction channels in the LLZO solid electrolyte investigated

here. However, the amplitude vs time changes slower at voids, which are partly filled with Li_2CO_3 (e.g. P_3 in Figure 3.13d). A higher time constant at void regions is reasonable, owing to the presence of Li_2CO_3, which is known to have a lower ionic diffusivity than that of pure LLZO[12,48,49].

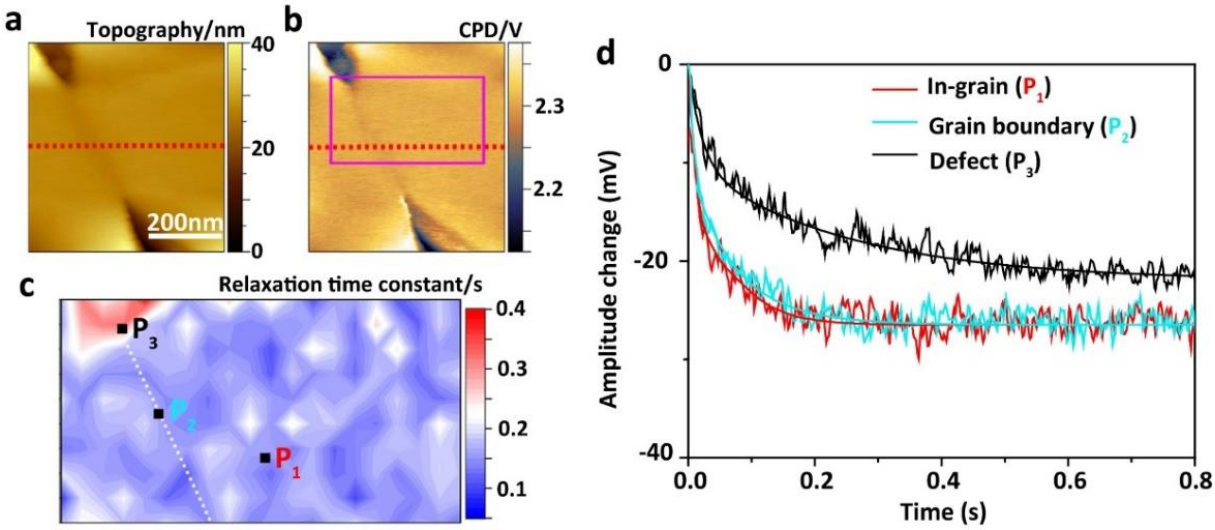

Figure 3.13 a SFM topography of LLZO including voids, grain boundaries and in-grain parts. The RMS roughness is 4.1 nm at 500 nm × 500 nm. **b** CPD map of the same place as in **a**. **c** Lithium ions relaxation time constant (τ) map of the purple wireframe area in **b**. **d** Amplitude change vs time curve of three points (in-grain, grain boundary and defect void) after removing the −3 V DC voltage from the SFM tip.

3.4 Electron-beam injection

The above tr-EFM experiments indicate that there is a negligible difference in ion mobility at grain boundaries compared to the in-grain parts even at the grain boundaries close to Li-CE. Thus, grain boundaries do not represent an additional barrier for lithium ions. Therefore, the electric potential drop at grain boundaries in KPFM measurements near the Li-CE interface might result from differences in electron transport properties in grain boundaries (Figure 3.9b). However, garnet-type electrolytes are ion conductors with a very poor electron conductivity of 10^{-8}–10^{-11} S cm^{-1} [31,38,50], which is about 10^4–10^7 times lower than their ionic conductivity. Therefore, it is not easy to quantify the electronic properties of LLZO using standard methods, i.e. by measuring the electronic conductivity in cells with an ion-blocking

electrode (Hebb-Wagner cell). Recently, an indirect method was reported, which was based on electron beam-induced alkali metal growth in different kinds of ionic conductors[51,52]. This method was used to infer properties of a garnet-type solid electrolyte induced by electrons[51].

With increasing electron irradiation time, the accumulation of electrons in/on LLZO creates enough nucleation overpotential to reduce lithium ions to lithium metal (Figure 3.14a). During electron-beam irradiation, the secondary electron (SE) or backscattered electron (BSE) signals are collected, allowing the morphology evolution to be recorded. Interestingly, the LLZO surface morphology changes with increasing electron-beam irradiation time (Figure 3.14b). After 40 seconds of electron-beam irradiation, three dark lines with bright particles appeared to meet at a tiny hole that was present also at 0 s. We attribute this hole to the intersection of three grain boundaries. Along these lines, we observed expulsions at regular intervals. These expulsions grow with longer electron exposure. After irradiation for around 320 s, there are no obvious additional changes in the morphology of the irradiated LLZO cross section. At grain boundaries, the expulsions have diameters of (160 ± 10) nm. However, expulsions of much smaller diameters, i.e. (30 ± 3) nm, also appear inside the grains. This proves that grain boundaries play a prominent role in lithium expulsion nucleation and growth of polycrystalline solid electrolytes. A Li_2CO_3 contamination layer and surface edges may favor nucleation[12]. However, we performed all our measurements on a freshly broken and polished LLZO cross section by strictly eliminating any possible contact with air. Therefore, Li_2CO_3 does not cover the LLZO surface.

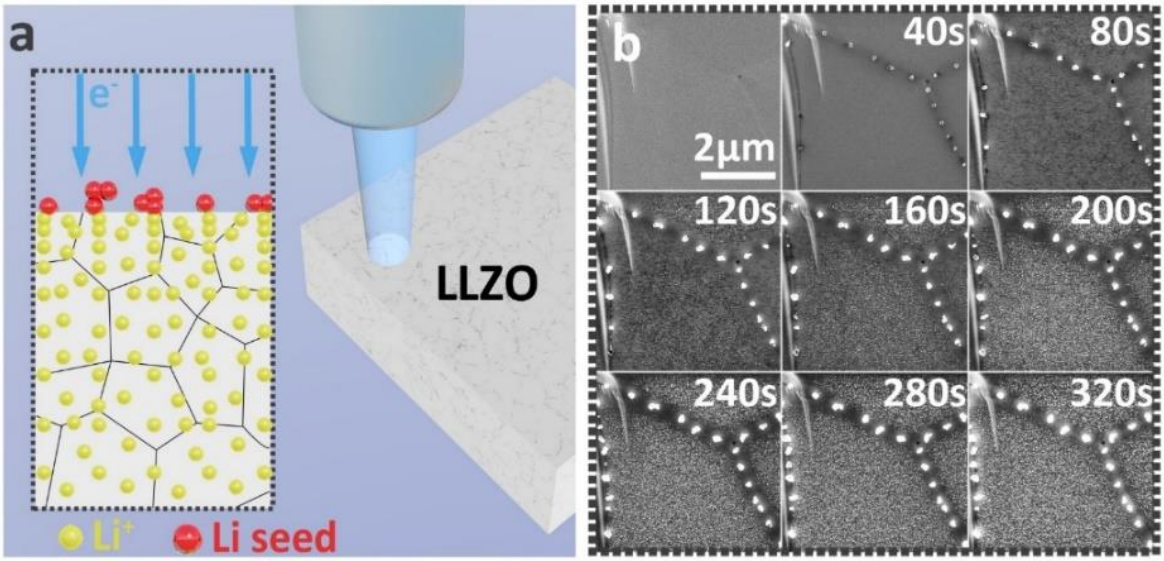

Figure 3.14 a Schematic diagram of electron injection causing a reduction of lithium ions in LLZO into lithium metal. **b** Morphological evolution of lithium particles with increasing duration under electron-beam irradiation on a LLZO cross section, including grain boundaries and in-grain areas.

To exclude effects arising from locally inhomogeneous chemical composition, we used an electron beam with the same acceleration voltage and probe current to irradiate samples at a different spot of the cross section on a much larger scale (Figure 3.15a). At this magnification, we observed 20 to 30 different grains. The diameter of each LLZO grain ranges from 5 to 10 µm. After electron-beam irradiation, the surface morphology at grain boundaries changed as described above (Figure 3.15b). To determine the composition of the expelled substance, we switched from the SE to the BSE detector and imaged the same area again (Figures 3.15c and 3.15d). In contrast to the SE signal, the BSE signal leads to a dark color at expulsions, whereas the substrate is white. Typically, for a BSE image, a darker color (i.e. a low number of BSE) is caused by lighter elements. Therefore, we attribute the expulsions to lithium, which is the lightest element in LLZO.

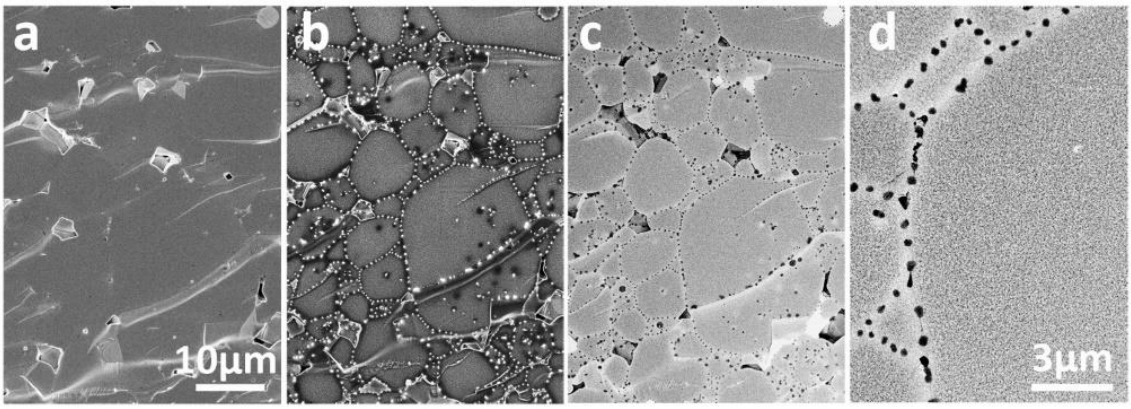

Figure 3.15 a Initial LLZO cross section morphology under electron-beam irradiation on large scale. **b** Morphology changes after electron-beam irradiation for 400 s under secondary electron detection mode. **c** Same area as in d, but electrons were collected with a backscattered electron detector. **d** Partial enlarged view of **c**.

This conclusion that expulsions are metallic lithium is supported by energy-dispersive X-ray (EDX) spectra of those expulsion particles before and after exposure to air for three minutes. The EDX spectra revealed a higher oxygen content of expulsions after being exposed to air, whereas other elements remained unchanged (Figure 3.16). This results from metallic lithium expulsions reacting with oxygen in air to form lithium oxide.

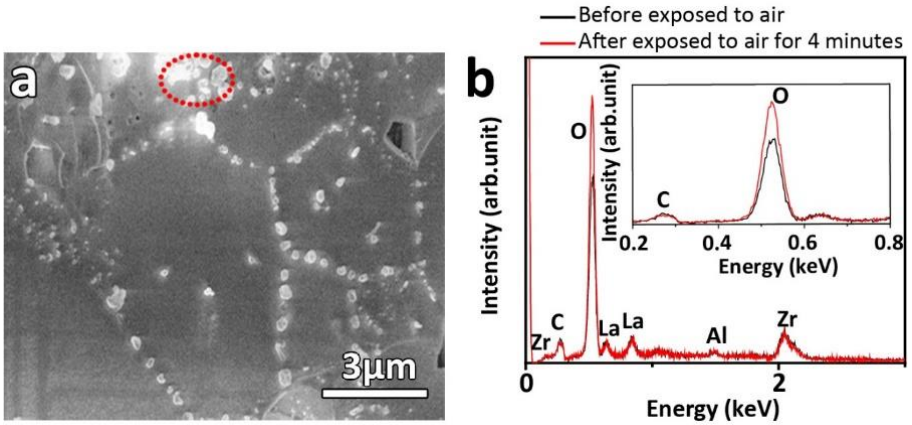

Figure 3.16 a SEM of a LLZO cross section after irradiation by electrons. Expulsions are visible on the surface. **b** EDX spectra recorded in the region marked by a red dotted circle in **a.** The black line corresponds to the spectrum of the sample before exposure to air and the red line to the one after exposure to air for 4 minutes. The inset shows a higher resolved spectrum around the signal corresponding to oxygen.

Next, we quantitatively analyzed the size and mass area density of expulsions at grain boundaries and in inner areas of grains. In particular, we observed a contrast in the SEM images near the grain boundaries (Figure 3.17a). This area is 300 to 400 nm wide and exhibits almost no extrusions, which is larger than LLZO grain boundaries with width below 10 nm[27]. We used this boundary to divide the surface into two kinds of areas: the inner-grain (IG) area with only tiny lithium expulsion particles, and the grain boundary (GB) area, including grain boundaries and their adjacent region with no expulsions (Figure 3.17b).

We analyzed the size changes of expulsions as a function of time and found that the diameter of expulsions increases with increasing electron dose, see Figure 3.17c. Interestingly, the first expulsions appeared in the GB area after 40 s. At this electron dose (~8140 e/nm^2), no features in the IG area could be detected. In general, grain boundaries are usually considered to be favorable sites for heterogeneous nucleation because of energetic reasons. After 360 s, expulsions with diameters of 166 ± 10 nm were observed at grain boundaries. For longer irradiation times, the diameter did not increase as much as before. For the lithium expulsions in the IG area, the average particle radius grew from 25.2 nm at 120 s to only 30.2 nm after 400 s. This analysis confirms that grain boundaries act as preferential sites for lithium metal nucleation. More importantly, the grain boundary structure appears to be beneficial for forming larger lithium expulsions.

Next, we compared the mass of expulsion per unit area at the GB area with respect to the IG area (Figure 3.17d). We calculated the areal mass density of the lithium expulsions θ by

$$\theta(t) = \frac{n(t) \cdot \frac{4}{3}\pi r(t)^3 \cdot \rho_{\mathrm{Li}}}{A} \tag{2}$$

where n is the total number of lithium expulsions, r is the average radius of lithium expulsions, ρ_{Li} is the density of lithium metal (0.534 g/cm³) and A is the surface area of the GB or IG. For the lithium expulsions at GB areas, θ_{GB} increases linearly as a function of time from 80 to 320 s. For an electron irradiation time of 320 s, we calculated a $\theta_{\mathrm{GB,320s}}$ of 13.53×10^{-15} µg nm^{-2}. For the IG area, we observed few expulsions for a duration of 40 s, meaning that θ is almost 0. For durations >40 s, θ_{IG} always stays below θ_{GB}. After 240 s, θ_{IG} stays constant at a value of approximately 3.4×10^{-15} µg nm^{-2}. To compare GB and IG areas,

we calculated a ratio of $\frac{\theta_{GB}}{\theta_{IG}}$ = 4.7 after electron-beam irradiation for 400 s. In other words, there are more lithium expulsions from the GB area than from the IG area.

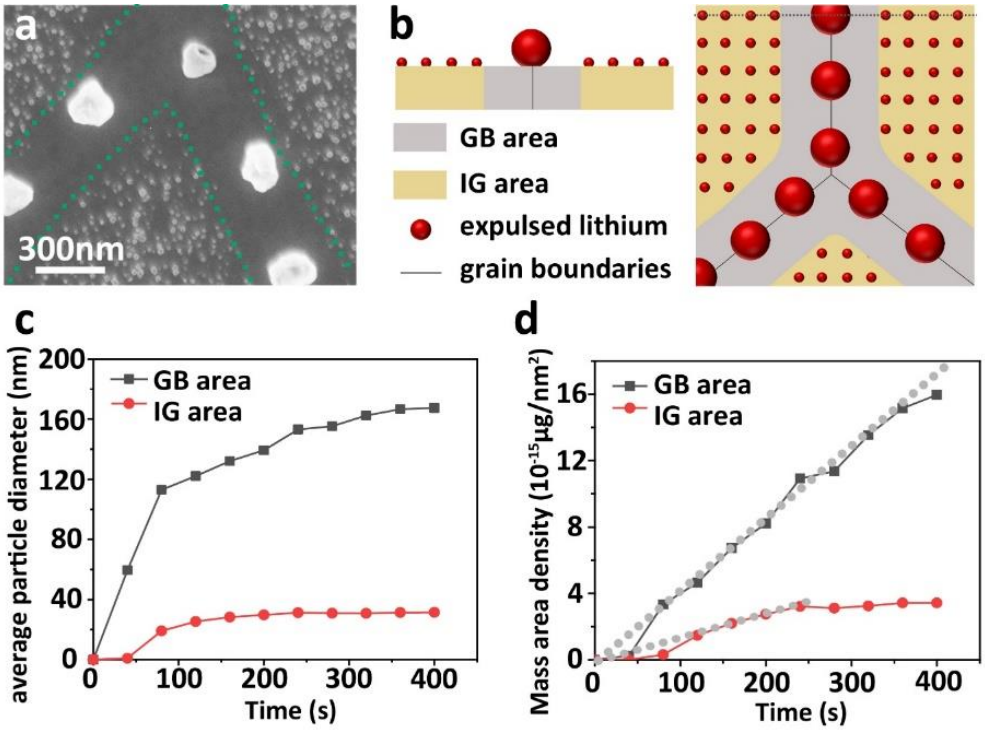

Figure 3.17 a Enlarged view of lithium expulsion at inner-grain (IG) area and grain boundary (GB) area. The IG area has only tiny lithium expulsion particles, whereas the GB area includes grain boundaries and their adjacent region with no expulsions. The green dashed lines are the boundaries of IG area and GB area. **b** Schematic of different lithium expulsions at IG area and GB area**. c** Average diameter and **d** Areal mass density evolution of expelled lithium particles with increasing duration of electron-beam irradiation at IG area and GB area. Dotted lines in **d** are the fitting results.

Time-of-flight–secondary ion mass spectrometry (ToF–SIMS) results showed that the lithium elemental concentration at grain boundaries is the same within the in-grain part (Figure 3.18). Therefore, a higher lithium-ion concentration at grain boundaries cannot be the reason for the ratio $\frac{\theta_{GB}}{\theta_{IG}}$ >1. Combining the fact that no lithium expulsions were observed in regions adjacent to grain boundaries, we conclude that more lithium expulsions at grain boundaries during electron-beam irradiation result from: (1) lithium ions in regions adjacent to grain boundaries move to the grain boundaries, and (2) lithium ions from the LLZO bulk move to

the LLZO surface preferably via grain boundaries. We have already shown before that there is no obvious difference in ionic conductivity between grain boundaries and in-grain parts. Thus, the movement of lithium ions to grain boundaries is enabled by additional electrons owing to irradiation, which create a stronger electric field at grain boundaries.

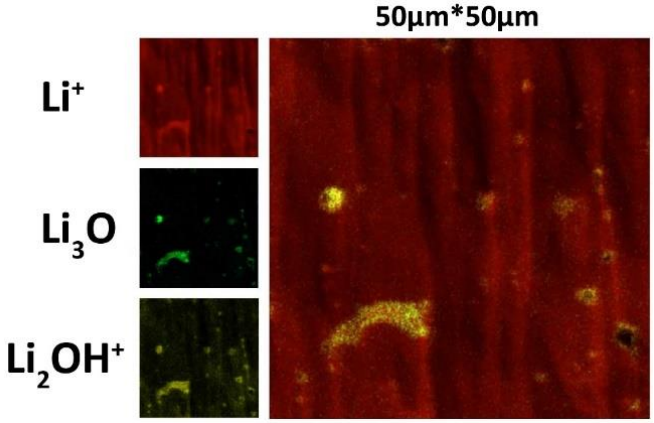

Figure 3.18 Ex-situ TOF-SIMS results of the lithium distribution in a LLZO cross section. Brighter colors indicate higher lithium-ion concentration.

Next, we quantified the expulsion rate based on a model proposed by Saito et al. for ionic conductors[53]:

$$\frac{d\theta}{dt} = r_1 \sigma E - r_2 \tag{3}$$

where σ is the ionic conductivity, E is the strength of the electric field created by injected electrons, r_1 is a constant related to the charge transfer resistance of lithium ions being reduced to metallic lithium and r_2 denotes a lithium metal evaporation coefficient. Our SEM measurements were performed in high vacuum (pressure 10^{-6} Pa). Under this condition, the evaporation coefficient r_2 of lithium metal can be ignored[57]. For the lithium expulsions at GB areas, we calculated lithium expulsion growth rate $(\frac{d\theta}{dt})_{\mathrm{GB}}$ of 0.0399 µg nm^{-2} s^{-1} (dotted lines in Figure 3.17d), which is 2.35 times greater than lithium expulsion growth rate at in-grain area $(\frac{d\theta}{dt})_{\mathrm{IG}}$ between 100 and 320 s. Therefore, $r_{1,\mathrm{GB}}\sigma_{\mathrm{GB}}E_{\mathrm{GB}}$ becomes 2.35 times greater than $r_{1,\mathrm{IG}}\sigma_{\mathrm{IG}}E_{\mathrm{IG}}$. Furthermore, as $\sigma_{\mathrm{GB}} = \sigma_{\mathrm{IG}}$, probably the larger E_{GB} is the possible factor that leads to a larger lithium expulsion rate in the GB region.

The presence of a stronger electric field at grain boundaries during electron-beam irradiation is also supported by the contrast at grains that developed during SEM imaging. We observed that, at the initial stage of electron-beam irradiation, there is almost no contrast between GB and IG areas in SE images, see Figure 3.19a. After electron-beam irradiation for 10, 20 and 30 s, the contrast develops as shown in Figure 3.19b-d, respectively. The grain boundaries gradually become darker than the in-grain parts. This means fewer secondary electrons are emitted from grain boundaries than from in-grain parts. We exclude an initially increased number of positive charges, i.e. lithium ions, at the GB area as there is no obvious difference in ionic conductivity between grain boundaries and in-grain parts. Thus, a locally higher electron concentration at grain boundaries prevents the generation of SE by deflecting primary electrons (PE)[54]. Electrons accumulate at the grain boundaries, which attract positive lithium ions from adjacent regions that move to grain boundaries. Also, those lithium ions attract a certain percentage of secondary electrons (Figure 3.19e). Changes in contrast could arise from irreversible reactions or changes in surface characteristics.

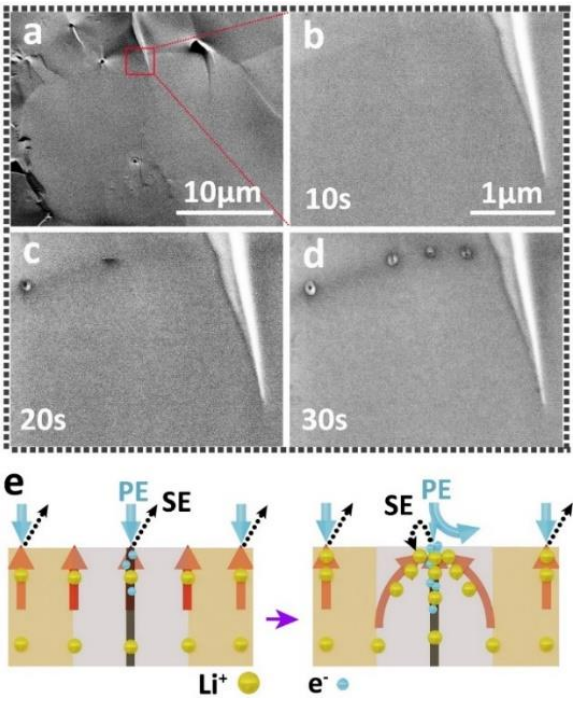

Figure 3.19 a SEM image of a cross-section of LLZO freshly prepared. **b–d** Changes of LLZO grain boundaries in the initial stage of electron-beam irradiation. **e** Schematic diagram of the negative charge effect in grain boundaries during electron-beam irradiation.

3.5 Model for electron-beam irradiation experiment

Using the findings presented above, we propose a model to explain how an electric field causes larger expulsions at grain boundaries. Our analysis of the electron-beam irradiation experiments reveals that electrons preferentially cause lithium nucleation and growth at grain boundaries. The higher electron concentration at grain boundaries leads to a higher electron concentration gradient from grain boundaries to their adjacent regions, which creates an electric field that attracts adjacent lithium ions (Figure 3.20b). The electric field increases with ongoing electron irradiation. Upon reaching a certain negative potential, lithium ions move towards the grain boundaries, where they are reduced to lithium nuclei as denoted by the red particles in Figure 3.20c. With an increasing amount of reduced lithium, mechanical strain builds up at grain boundaries. Such mechanical strain extrudes lithium from the surface of LLZO (Figure 3.20d). Such extrusions occur less frequently at the IG areas belonging to bulk LLZO. There, no distinctly greater electron accumulation takes place, and the lithium reduction occurs only at much higher electron-irradiation doses. In the IG area, the lithium expulsion rate is lower, and the diameters of the final expulsions are smaller und uniformly distributed. This model illustrates how the local electron-conduction properties facilitate lithium-metal nucleation and growth at grain boundaries.

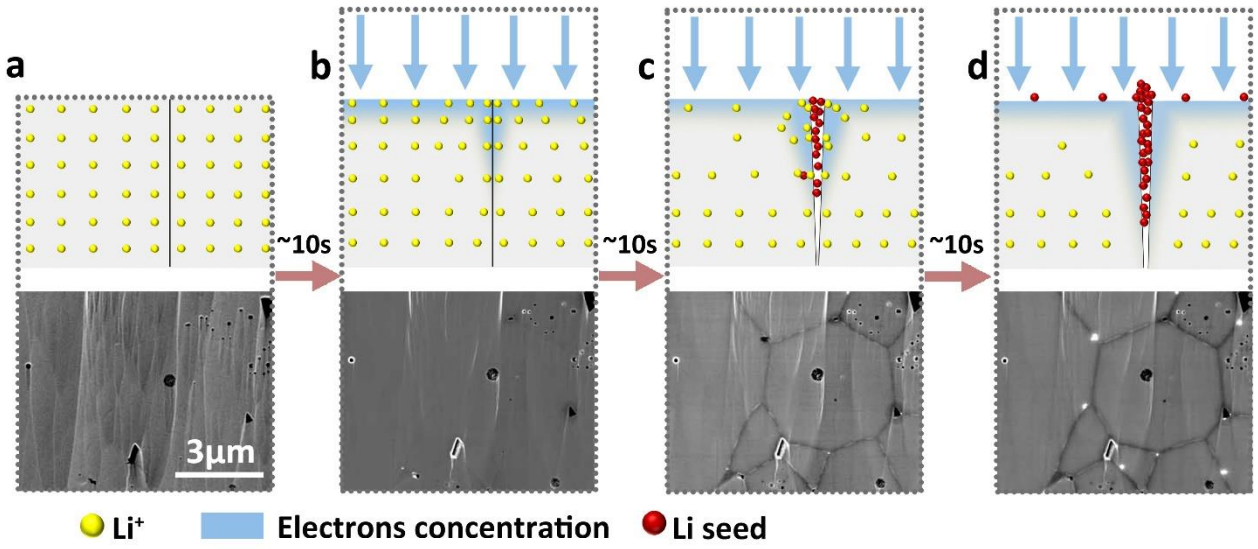

Figure 3.20 a-d Schematic diagram of the formation of metal-lithium particles on LLZO surface during electron-beam injection with a time step around 10 s.

3.6 Model for lithium-dendrite growth along grain boundaries

We have analyzed the electrical behavior of LLZO samples by *operando* KPFM, tr-EFM and SEM to understand the dynamics of preferential lithium nucleation and expulsion in and from grain boundaries. Local tr-EFM and KPFM measurements indicate that grain boundaries do not provide a preferential channel for lithium ion transport. Thus, we suggest that lithium ion transport is virtually homogeneous inside LLZO sintered in an oxygen atmosphere without pressure. However, our results also indicate that electron transport in LLZO is non-homogeneous near the lithium electrode. We conclude from our *operando* KPFM and electron-beam irradiation results that the grain boundaries near the (plating) lithium anode become more resistive for ions. The latter results from accumulation of electrons at grain boundaries causing a "space charge layer" like structure. This cannot be observed in amorphous solid electrolyte Li_3PO_4 without grain boundaries.

We elucidate that grain boundaries trap excess electrons from the plating electrode. DFT simulations suggest a smaller band gap in LLZO grain boundaries relative to the bulk, [18] which could be the origin of trapping excess electrons (in chemical terms: trapping excess Li^0). Those excess electrons could cause "space charge layer" formation at grain boundaries causing a step-like CPD signal. Further work is required to unravel the potential role of bipolarization effects at grain boundaries under current load. As a consequence of this space charge layer, lithium metal penetrates into LLZO. In fact, dendrites are often observed primarily at grain boundaries after cycling batteries with a LLZO solid electrolyte separator (Figure 3.21).

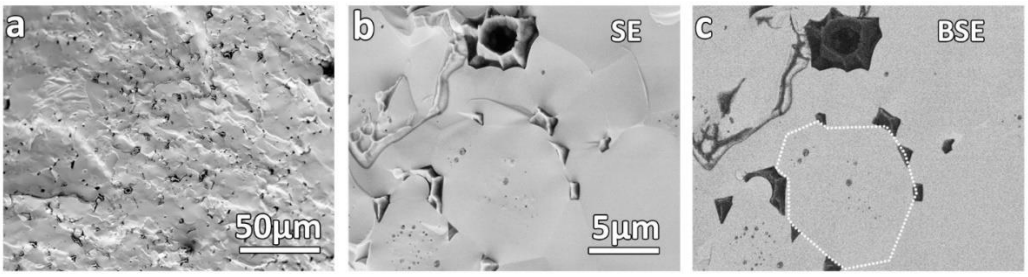

Figure 3.21 a SEM of a LLZO cross section after lithium dendrites have grown. **b** SE mode SEM of the LLZO cross section with lithium dendrites filing voids and penetrating grain boundaries. **c** BSE mode SEM of the LLZO in the same area with **b**.

During the charging process of a SSB cell with lithium metal anode, lithium ions are extracted from the cathode and move to the lithium anode (Figure 3.22). At the same time, the lithium anode provides electrons to the LLZO solid electrolyte surface, thus reducing lithium ions to lithium at the Li|LLZO interface. Near the anode Li|LLZO interface, lithium metal grows through voids and defects in the LLZO. When these primary lithium dendrites reach grain boundaries, they inject electrons preferentially to the grain boundaries owing to their different conductivity for electrons. With progressing duration or increasing current density, the electron concentration locally increases within grain. Thus, grain boundaries near the plating lithium anode areas reach the overpotential for lithium-ion reduction earlier than other parts in the entire LLZO. Then formed lithium dendrites continue to grow along other grain boundaries, again due to the high grain boundary electron trapping ability, leading to easier lithium ion reduction. Because of the limitation of KPFM scanning area and the randomness and uncertainty in lithium dendrite growth in LLZO, we can only observe the initial grain boundary effect on electron transport close to the plating Li-CE but not track the whole lithium growth process. In addition, the growth can be enhanced by internal strain in grain boundaries that opens additional voids and cracks. In those voids and cracks, lithium can further nucleate and grow, and dendritic growth continues. The lithium dendrites gradually fill voids, defects and grain boundaries. Finally, this process continues along grain boundaries until dendrites reach the cathode. As a result, the battery short-circuits.

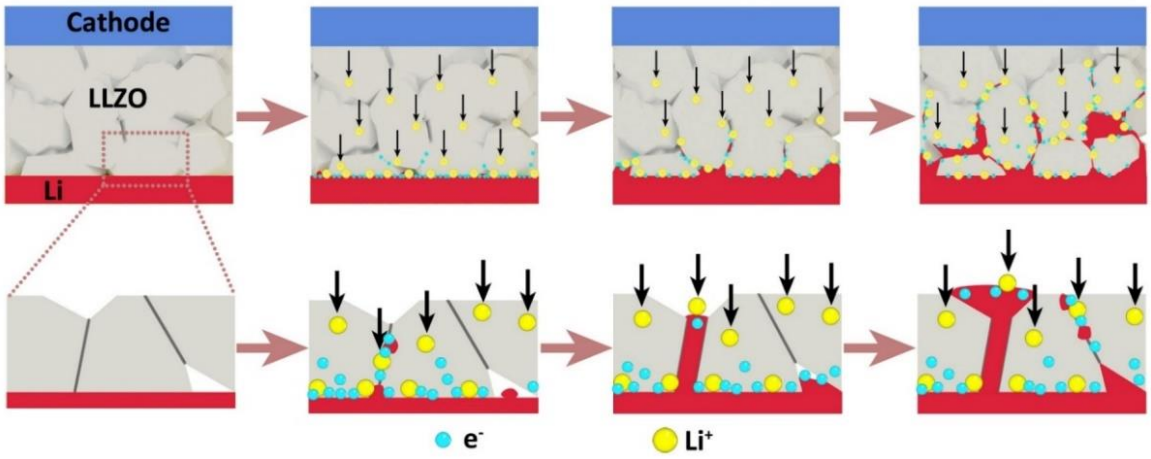

Figure 3.22 Lithium-dendrite growth along grain boundaries.

This growth mode is very similar to the one derived by phase field simulation results based on DFT calculation performed by Tian et al. [18] Cubic-$Li_7La_3Zr_2O_{12}$ grain surface and grain boundaries are prone to trap excess surface electrons. The phase field simulation shows that Li dendrites first form at grain boundaries close to Li-CE – as our KPFM measurements also suggest. With increasing Li plating time, Li dendrites growth faster along grain boundaries because the high electron concentration at grain boundaries promotes Li ion reduction[55-57].

Our model explains important aspects of the dynamic and preferential growth of lithium dendrites at grain boundaries. In particular, our *operando* analysis indicates that growth of lithium dendrites starts at LLZO grain boundaries near the lithium anode, and that the electronic conduction properties of grain boundaries play a major role in this process. Understanding lithium dendrite (or filamentary) growth is important to prevent failure of all-solid-state batteries. Our findings indicate that the interface to the lithium anode is of particular importance for suppressing dendritic growth. Adding a functional layer there could be the key to suppressing electron uptake along grain boundaries as well as dendritic growth. Our findings provide new prospects for further nanoscale research with high resolution on the interfaces of all-solid-state batteries and the inner parts of solid electrolyte materials.

3.7 Experiment

LLZO preparation

To synthesize garnet-type solid electrolyte $Li_{6.25}Al_{0.25}La_3Zr_2O_{12}$ (LLZO) Li_2CO_3 (>99.0%, Sigma-Aldrich), $La(OH)_3$ (99.9%, Sigma-Aldrich), Al_2O_3 (99.8%, abcr), and ZrO_2 nano-powder (<100 nm, Sigma-Aldrich) were mixed in a stoichiometric ratio. This mixture was then ball-milled for 12 h at 350 rpm under pure oxygen atmosphere. After milling, the homogenized powder was pressed into large pellets in MgO-crucibles and then calcined at 1000°C for 4 h under a 150-sccm oxygen flow. After ball-milling again for 20 hours at 350 rpm, small pellets with diameters of approximately 8.3 mm and thicknesses of 2 mm were isostatically pressed with 380 MPa and sintered at 1230°C in MgO crucibles with mother powder (calcined LLZO powder) under oxygen flow. The LLZO pellets have a porosity of approximately 94 ± 2%, their ionic conductivity is $(4.6\pm0.4)10^{-4}$ S cm^{-1}. The sintered LLZO was characterized with x-ray

diffraction by using a PANalytical Empyrean powder diffractometer in Bragg-Brentano θ-θ geometry with copper K_α radiation. More preparation details and properties of LLZO are provided by Krauskopf et al[35] and Fuchs et al[32,58]. A diffractogram of sintered LLZO in Figure S1 shows that only the cubic LLZO phase is present with neither impurities nor the tetragonal phase.

Cell fabrication

Li|LLZO|Li symmetric cells were prepared in a glove box filled with argon gas (purity 99.9999%, $p(H_2O)/p$ < 0.1 ppm and $p(O_2)/p$ < 0.1 ppm).

For a Li|LLZO|Li symmetric cell, first, the surface of LLZO with a diameter of 8.35 mm was polished with 1200-grit SiC sandpaper (Buehler, CarbiMet) to smooth the surface and remove the surface passivation layer. Then, the lithium electrodes were fabricated by pressing freshly prepared lithium metal sheets at an isostatic pressure of 400 MPa in an oil-press protected by three sealed polymer layers onto the two opposite, polished faces of the LLZO pellet. The used lithium sheets were prepared prior by removing the native passivation layer of a lithium metal chunk (100% lithium, TMAX) with a ceramic knife and subsequent pressing to a thin foil. The diameter and thickness of the lithium metal electrode were approximately 6 mm and 0.1 mm, respectively.

Electrochemical measurements

Electrochemical performance measurements were carried out in an Ar glove box ($p(H_2O)/p$ < 0.1 ppm and $p(O_2)/p$ < 0.1 ppm) with a potentiostat (SP150, Biologic) under room temperature 23 ± 2 °C. We applied an external current to one lithium electrode as the working electrode (WE). The other lithium electrode was connected to ground and acted as the counter electrode (CE). We did not apply external pressure on the cell during electrochemical measurements.

1) Electrochemical impedence spectroscopy (EIS): EIS was carried out within the frequency range of 3 MHz to 0.1 Hz with an amplitude of 10 mV and 6 data points per frequency decade. Fitting was performed using the software RelaxIS 3. We used an equivalent circuit of two

parallel R_i-C_i-elements in series, where R_i and C_i denote resistance and capacitance of the bulk and grain boundary transport processes. A 30 second OCV measurement was carried out prior to measuring to secure that the system is in a relaxed state.

2) Constant current/potential measurements: For the Li|LLZO|Li symmetric cells, the Li-WE was connected to the WE of the potentiostat. The Li-CE was connected to the CE of potentiostat are connected to ground. Then, different currents or potentials were applied on Li-WE to drive lithium ions move from Li-WE to Li-CE. At the same time, operando KPFM is carried on the surface of LLZO.

Argon ion milling

For SEM and SFM experiments, we prepared smooth cross sections by argon-ion milling (IM4000, Hitachi). First, we broke the cell into two pieces along the diameter of the sample. Then, half of the broken cell was fixed in a cross-section milling holder. Next, a 100-µm-thick stainless-steel mask was placed in front of the lithium electrode to define the position for argon-ion milling (Figure 3.23). Ion milling was performed at an acceleration voltage of 2 kV with a discharge current of approximately 450 µA. During argon-ion milling, the sample stage rotated at a speed of 30 rpm. The polishing process took approximately 14 hours. After ion milling, we used the air protection system of the argon-ion milling machine to transfer samples from the ion-milling chamber to the argon glove box. Typically, the surface root mean square (RMS) roughness after argon-ion milling was approximately 20 nm at an area of 5 × 5 μm^2 measured by means of SFM.

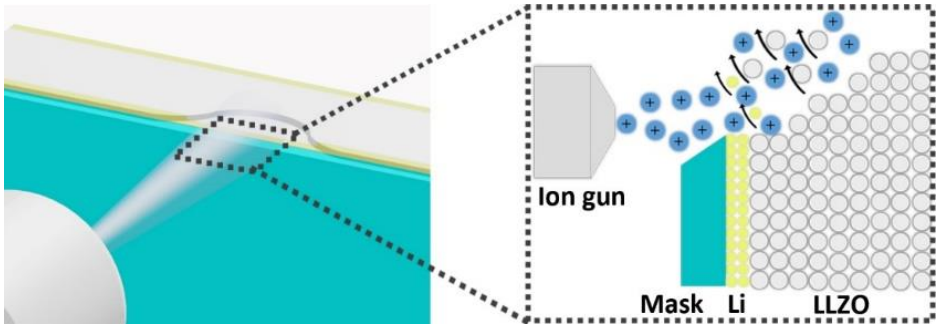

Figure 3.23 Schematic 3D representation of the argon ion milling direction and its atomistic process for the Li|LLZO|Li cell in side view.

Scanning Force Microscopy

All scanning force microscopy (SFM) measurements including operando KFPM and tr-EFM (MFP-3D Asylum Research, Oxford Instrument, USA)) were performed in a glove box (GS, Germany) filled with argon (purity 99.9999%). The inert argon gas environment prevents battery degradation, including LLZO and lithium electrodes reacting with O_2, N_2, CO_2, N_2 and H_2O. SFM measurements were taken with PtIr-coated cantilevers, having a nominal spring constant of 2 N/m and a nominal resonance frequency of 75 kHz (SCM-PIT-V2, Bruker, USA). A homemade holder was used to fix and connect the battery sample to the potentiostat. The potentiostat was operated outside the glove box with electrical connections through the glove box wall.

1) Operando KPFM:

KPFM measurements were done in heterodyne frequency modulation (FM) mode with an external lock-in amplifier (Zurich Instruments HF2LI-MOD).

We firstly performed KPFM measurements on the LLZO surface at position x in equilibrium, i.e. without any external potential applied to the Li-CE. The measured CPD value on the LLZO surface corresponds to Volta potential between SFM tip and LLZO[59]. Upon applying a constant external current or voltage to the symmetric Li|LLZO|Li cell, we measured a CPD change, $\Delta CPD(x)$, at a specific position x on LLZO surface, which is defined as:

$$\Delta CPD(x) = CPD(x)_{applied} - CPD(x)_{OCV} = k(x) \cdot \phi_{applied} + \Delta\Phi(x) \qquad (4)$$

Here, $CPD(x)_{\mathrm{OCV}}$ is the contact potential difference in the OCV state. $CPD(x)_{\mathrm{applied}}$ is the contact potential difference with an applied potential ϕ_{applied}. $\Delta\Phi(x)$ is work function change of the LLZO surface at position x, which changes with a material's composition change.

2) Tr-EFM:

Tr-EFM measurements were performed with the external lock-in amplifier (Zurich Instruments HF2LI-MOD) as well.

We performed tr-EFM measurements as follows. First, the cantilever was excited mechanically at its first resonance frequency, and the corresponding amplitude was used as signal for the topography feedback electronics. In addition, we applied an AC voltage at the second resonance frequency. Next, we engaged the tip to the surface and applied a DC bias voltage of −3 V for 1.5 s at the tip to induce ion displacements in LLZO. Then, we grounded the tip for 1.5 s to allow ion relaxation, after which we retracted the tip and repeated this sequence at the next position. During this sequence, we recorded the vibration amplitude of the cantilever at its second resonance frequency (ω) to track changes of the electrostatic force $F_{\mathrm{es(t,\omega)}}$. As lithium ions are the main mobile charges in LLZO, we attribute changes of the electrostatic force to lithium ion displacements. In solid ionic conductors, the ionic transport follows a stretched-exponential time response due to the electric field between sample and tip[60-63]

$$\Delta A_{(\mathrm{t},\omega)} = \Delta A_{\mathrm{slow}} \exp\left[-(\mathrm{t}/\tau)^{\beta}\right] + \Delta A_{\mathrm{fast}} \quad (5)$$

where $\Delta A_{(\mathrm{t},\omega)}$ is the total amplitude change at frequency ω, ΔA_{fast} is the amplitude change before ionic relaxation due to ultrafast vibrational and electronic polarization[43,64], ΔA_{slow} is the amplitude change until the system reaches a saturation state due to ionic relaxation, τ is a time constant and β is a stretch exponent representing ion diffusion properties.[43] For simplicity, we set β to 1 to fit the $\Delta A_{(\mathrm{t},\omega)}$ vs. time curve. Differences in ion diffusivity ($D \sim 1/\tau$) can be measured by calculating τ according to fitting equation 5 to measurements recorded at different positions on a freshly prepared LLZO surface.

In order to detect electrostatic forces induced by the AC potential, we recorded the amplitude of oscillation at a frequency corresponding to the second resonance frequency of the cantilever (amplitude 1) using a Zurich Lock-In amplifier. In addition, we plotted the amplitude of the cantilever oscillation at the first resonance frequency of the cantilever (amplitude 2). This amplitude is used for the topography feedback electronics and is excited by the piezoelectric actuator. In this case, the feedback electronics regulate the z-position of the piezoelectric element to keep an amplitude around 30 nm. Upon applying the DC voltage, the

electronic feedback loop regulates within 40-50 ms the z-position of the piezoelectric element and compensates for the electrostatic forces acting between the entire cantilever and the sample. The remaining slower changes of amplitude 1 arise from ion movement in LLZO (Figure 3.24a). We performed reference measurements on a pure gold sample, which is not ion conducting. Correspondingly, we did not observe a slow change of amplitude 1 (Figure 3.24b). The comparison of tr-EFM results on LLZO and Au shows that tr-EFM can effectively track ion diffusivity in ionic conductors.

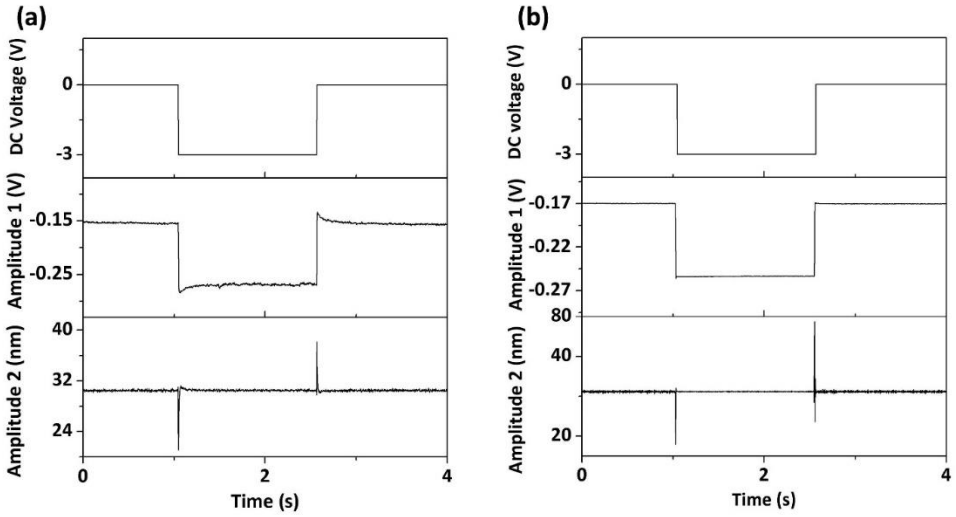

Figure 3.24 Tr-EFM comparison when applied on LLZO and Au. At each pixel of an image, we applied a DC-voltage for 1.5 seconds with an amplitude of -3 V to the SFM tip in respect to the sample. The corresponding time resolved EFM signals recorded at the first (amplitude 2) and second resonance frequency (amplitude 1) of the cantilever. **a** Measurement on the LLZO and **b** on a gold reference sample.

Electron beam irradiation and scanning electron spectroscopy (SEM)

Electron beam irradiation experiments and SEM measurements were performed in a field-emission SEM (Hitachi SU800). To avoid surface contamination or reaction with air of LLZO, a transport sealing box filled with argon gas (purity 99.9999%) was used to transfer samples from the glove box into the instrument. For transport we used a sealed box filled with argon gas. The LLZO pellet was fixed to an SEM sample holder, which allowed the investigation the cross section in vertical direction and electrically insulated LLZO pellet. A region on the LLZO

surface was selected by SEM standard imaging mode using the secondary electron detector which shall be irradiated with electrons. Then, this region was irradiated with the electron beam using an acceleration voltage of 5 kV, leading to a probe current of ~1 nA. At the same time, we followed changes in the surface by reading out the secondary electron detector or the backscattered electron detector.

Time-of-flight–secondary ion mass spectroscopy (ToF–SIMS)

We used ToF-SIMS (IONTOF TOF.SIMS NCS) to characterize the lithium element and related molecular information on the surface of LLZO, especially lithium and its related molecular species. Bi^{3+} ions with an energy of 30 keV served as the primary ion source. To reduce surface roughness, the LLZO cross section was first polished by argon-ion milling as described above. Then we used a transfer chamber filled with pure argon gas to protect the LLZO cross section during the transfer into the ToF-SIMS chamber. The LLZO sample was installed in the ToF-SIMS chamber and then the chamber was evacuated to high vacuum ($<10^{-5}$ mbar). The LLZO was exposed to air for less than one minute while the sample was being installed in the ToF-SIMS chamber.

3.8 Statement of contribution

Rüdiger Berger and Chao Zhu conceived the idea. Chao Zhu carried out the Ar ion milling polishing, KPFM and tr-EFM experiments. Till Fuchs prepared and characterized LLZO and Li|LLZO|Li symmetrical cell. Stefan A.L. Weber and Franjo Weber assisted in KPFM and tr-EFM experiments. Gunnar Glaßer and Chao Zhu performed SEM measurements. Chao Zhu performed all other data collection and analysis. Chao Zhu wrote the manuscript. Hans-Jürgen Butt, Rüdiger Berger, Jürgen Janek, Felix. H. Richter and Till Fuchs provided expertise, electrochemical input, feedback and revised the manuscript.

3.9 Reference

1 Xu, X. *et al.* Local Multimodal Electro-Chemical-Structural Characterization of Solid-Electrolyte Grain Boundaries. *Adv. Energy Mater.* **11**, 2003309 (2021).

2 Dawson, J. A. *et al.* Toward understanding the different influences of grain boundaries on ion transport in sulfide and oxide solid electrolytes. *Chem. Mater.* **31**, 5296-5304 (2019).

3 Wu, B. *et al.* The role of the solid electrolyte interphase layer in preventing Li dendrite growth in solid-state batteries. *Energy Environ. Sci.* **11**, 1803-1810 (2018).

4 Gao, J. *et al.* Rational Design of Mixed Electronic-Ionic Conducting Ti-Doping $Li_7La_3Zr_2O_{12}$ for Lithium Dendrites Suppression. *Adv. Funct. Mater.* **31**, 2001918 (2021).

5 Qi, Y., Ban, C. & Harris, S. J. A New General Paradigm for Understanding and Preventing Li Metal Penetration through Solid Electrolytes. *Joule* (2020).

6 Kazyak, E. *et al.* Li penetration in ceramic solid electrolytes: operando microscopy analysis of morphology, propagation, and reversibility. *Matter* **2**, 1025-1048 (2020).

7 Janek, J. & Zeier, W. G. A solid future for battery development. *Nature Energy* **1**, 1-4 (2016).

8 Lu, Y. & Chen, J. Prospects of organic electrode materials for practical lithium batteries. *Nat. Rev. Chem.* **4**, 127-142 (2020).

9 Xie, J. & Lu, Y.-C. A retrospective on lithium-ion batteries. *Nat. Commun.* **11**, 1-4 (2020).

10 Lee, Y.-G. *et al.* High-energy long-cycling all-solid-state lithium metal batteries enabled by silver–carbon composite anodes. *Nat. Energy* **5**, 299-308 (2020).

11 Cheng, E. J., Sharafi, A. & Sakamoto, J. Intergranular Li metal propagation through polycrystalline $Li_{6.25}Al_{0.25}La_3Zr_2O_{12}$ ceramic electrolyte. *Electrochim. Acta* **223**, 85-91 (2017).

12 Huo, H. *et al.* Li_2CO_3: a critical issue for developing solid garnet batteries. *ACS Energy Lett.* **5**, 252-262 (2019).

13 Famprikis, T., Canepa, P., Dawson, J. A., Islam, M. S. & Masquelier, C. Fundamentals of inorganic solid-state electrolytes for batteries. *Nat. Mater.* **18**, 1278-1291 (2019).

14 Connell, J. G. *et al.* Kinetic versus Thermodynamic Stability of LLZO in Contact with Lithium Metal. *Chem. Mater.* **32**, 10207-10215 (2020).

15 Meng, J., Zhang, Y., Zhou, X., Lei, M. & Li, C. Li_2CO_3-affiliative mechanism for air-accessible interface engineering of garnet electrolyte via facile liquid metal painting. *Nat. Commun.* **11**, 1-12 (2020).

16 Porz, L. *et al.* Mechanism of lithium metal penetration through inorganic solid electrolytes. *Adv. Energy Mater.***7**, 1701003 (2017).

17 Yu, S. & Siegel, D. J. Grain boundary contributions to Li-ion transport in the solid electrolyte $Li_7La_3Zr_2O_{12}$ (LLZO). *Chem. Mater.* **29**, 9639-9647 (2017).

18 Tian, H.-K., Liu, Z., Ji, Y., Chen, L.-Q. & Qi, Y. Interfacial electronic properties dictate Li dendrite growth in solid electrolytes. *Chem. Mater.* **31**, 7351-7359 (2019).

19 Tantratian, K., Yan, H., Ellwood, K., Harrison, E. T. & Chen, L. Unraveling the Li Penetration Mechanism in Polycrystalline Solid Electrolytes. *Adv. Energy Mater.* **11**, 2003417 (2021).

20 Gao, B., Jalem, R., Tian, H.-K. & Tateyama, Y. Revealing Atomic-Scale Ionic Stability and Transport around Grain Boundaries of Garnet $Li_7La_3Zr_2O_{12}$ Solid Electrolyte. Adv. Energy Mater. 12, 2102151 (2022).

21 Cheng, L. *et al.* Effect of surface microstructure on electrochemical performance of garnet solid electrolytes. *ACS Appl. Mater. interfaces* **7**, 2073-2081 (2015).

22 Pesci, F. M. *et al.* Establishing ultralow activation energies for lithium transport in garnet electrolytes. *ACS Appl. Mater. interfaces* **12**, 32806-32816 (2020).

23 Dawson, J. A., Canepa, P., Famprikis, T., Masquelier, C. & Islam, M. S. Atomic-scale influence of grain boundaries on Li-ion conduction in solid electrolytes for all-solid-state batteries. *J. Am. Chem. Soc.* **140**, 362-368 (2018).

24 Zhao, Q., Stalin, S., Zhao, C.-Z. & Archer, L. A. Designing solid-state electrolytes for safe, energy-dense batteries. *Nat. Rev. Mater.* **5**, 229-252 (2020).

25 Lu, Z. *et al.* Modulating Nanoinhomogeneity at Electrode–Solid Electrolyte Interfaces for Dendrite-Proof Solid-State Batteries and Long-Life Memristors. *Adv. Energy Mater.* **11**, 2003811 (2021).

26 Song, Y. *et al.* Probing into the origin of an electronic conductivity surge in a garnet solid-state electrolyte. *J. Mater. Chem. A* **7**, 22898-22902 (2019).

27 Liu, X. *et al.* Local electronic structure variation resulting in Li 'filament'formation within solid electrolytes. *Nat. Mater.* **20**, 1-6 (2021).

28 Weber, S. A. *et al.* How the formation of interfacial charge causes hysteresis in perovskite solar cells. *Energy Environ. Sci.* **11**, 2404-2413 (2018).

29 Bergmann, V. W. *et al.* Real-space observation of unbalanced charge distribution inside a perovskite-sensitized solar cell. *Nat. Commun.* **5**, 1-9 (2014).

30 Coffey, D. C. & Ginger, D. S. Time-resolved electrostatic force microscopy of polymer solar cells. *Nat. Mater.* **5**, 735-740 (2006).

31 Buschmann, H. *et al.* Structure and dynamics of the fast lithium ion conductor "$Li_7La_3Zr_2O_2$". *Phys. Chem. Chem. Phys.* **13**, 19378-19392 (2011).

32 Krauskopf, T., Hartmann, H., Zeier, W. G. & Janek, J. r. Toward a fundamental understanding of the lithium metal anode in solid-state batteries—an electrochemo-mechanical study on the garnet-type solid electrolyte $Li_{6.25}Al_{0.25}La_3Zr_2O_{12}$. *ACS Appl. Mater. interfaces* **11**, 14463-14477 (2019).

33 Otto, S.-K. *et al.* In-Depth Characterization of Lithium-Metal Surfaces with XPS and ToF-SIMS: Toward Better Understanding of the Passivation Layer. *Chemistry of Materials* **33**, 859-867 (2021).

34 Peppler, K., Reitz, C. & Janek, J. Field-driven migration of bipolar metal particles on solid electrolytes. *Appl. Phys. Lett.* **93**, 074104 (2008).

35 Liu, F. *et al.* Dynamic spatial progression of isolated lithium during battery operations. *Nature* **600**, 659-663 (2021).

36 Krauskopf, T., Richter, F. H., Zeier, W. G. & Janek, J. r. Physicochemical concepts of the lithium metal anode in solid-state batteries. *Chem. Rev.* **120**, 7745-7794 (2020).

37 Kim, K. J. & Rupp, J. L. All ceramic cathode composite design and manufacturing towards low interfacial resistance for garnet-based solid-state lithium batteries. *Energy Environ Sci.* **13**, 4930-4945 (2020).

38 Han, F. *et al.* High electronic conductivity as the origin of lithium dendrite formation within solid electrolytes. *Nat. Energy* **4**, 187-196 (2019).

39 Banerjee, A., Wang, X., Fang, C., Wu, E. A. & Meng, Y. S. Interfaces and interphases in All-Solid-State batteries with inorganic solid electrolytes. *Chem. Rev.* **120**, 6878-6933 (2020).

40 Wang, C. *et al.* Garnet-type solid-state electrolytes: materials, interfaces, and batteries. *Chem. Rev.* **120**, 4257-4300 (2020).

41 Sharafi, A., Haslam, C. G., Kerns, R. D., Wolfenstine, J. & Sakamoto, J. Controlling and correlating the effect of grain size with the mechanical and electrochemical properties of $Li_7La_3Zr_2O_{12}$ solid-state electrolyte. *J. Mater. chem. A* **5**, 21491-21504 (2017).

42 Sun, Y. *et al.* X-ray Nanoimaging of Crystal Defects in Single Grains of Solid-State Electrolyte $Li_{7-3x}Al_xLa_3Zr_2O_{12}$. *Nano Lett.* **21**, 4570-4576 (2021).

43 Schirmeisen, A. *et al.* Fast interfacial ionic conduction in nanostructured glass ceramics. *Phys. Rev. Lett.* **98**, 225901 (2007).

44 Schönenberger, C. & Alvarado, S. Observation of single charge carriers by force microscopy. *Phys. Rev. Lett.* **65**, 3162 (1990).

45 Mascaro, A., Miyahara, Y., Enright, T., Dagdeviren, O. E. & Grütter, P. Review of time-resolved non-contact electrostatic force microscopy techniques with applications to ionic transport measurements. *Beilstein J. Nanotechnol.* **10**, 617-633 (2019).

46 Lu, Y. *et al.* Electrostatic force microscopy on oriented graphite surfaces: coexistence of insulating and conducting behaviors. *Phys. Rev. Lett.* **97**, 076805 (2006).

47 Melitz, W., Shen, J., Kummel, A. C. & Lee, S. Kelvin probe force microscopy and its application. *Surf. Sci. Rep.* **66**, 1-27 (2011).

48 Dissanayake, M. & Mellander, B.-E. Phase diagram and electrical conductivity of the Li_2SO_4-Li_2CO_3 system. *Solid State Ion.* **21**, 279-285 (1986).

49 Ma, C. *et al.* Corrigendum: Excellent Stability of a Lithium-Ion-Conducting Solid Electrolyte upon Reversible Li^+/H^+ Exchange in Aqueous Solutions. *Angew. Chem. Int. Ed.* **54**, 1063-1063 (2015).

50 Philipp, M. *et al.* The Electronic Conductivity of Single Crystalline Ga-Stabilized Cubic $Li_7La_3Zr_2O_{12}$: A Technologically Relevant Parameter for All-Solid-State Batteries. *Adv. Mater. Interfaces* **7**, 2000450 (2020).

51 Xie, X. *et al.* Lithium expulsion from the solid-state electrolyte $Li_{6.4}La_3Zr_{1.4}Ta_{0.6}O_{12}$ by controlled electron injection in a SEM. *ACS Appl. Mater. interfaces* **10**, 5978-5983 (2018).

52 Krauskopf, T. *et al.* Lithium-metal growth kinetics on LLZO garnet-type solid electrolytes. *Joule* **3**, 2030-2049 (2019).

53 Saito, Y., Nakagawa, M., Yamada, M., Miyajima, Y. & Yamamoto, Y. Estimation of ionic mobility of sodium ion conductor by scanning electron microscopy observation of sodium metal deposition. *J. Mater. Sci. Lett.* **15**, 898-901 (1996).

54 Kim, K. H., Akase, Z., Suzuki, T. & Shindo, D. Charging effects on SEM/SIM contrast of metal/insulator system in various metallic coating conditions. *Mater. Trans.* 1005171076-1005171076 (2010).

55 Kinzer, B. *et al.* Operando analysis of the molten Li|LLZO interface: Understanding how the physical properties of Li affect the critical current density. *Matter* **4**, 1947–1961 (2021).

56 Albertus, P. Soft and liquid metals. *Nat. Energy* **6**, 225-226 (2021).

57 Huo, H. *et al.* Design of a mixed conductive garnet/Li interface for dendrite-free solid lithium metal batteries. *Energy Environ. Sci.* **13**, 127-134 (2020).

58 Fuchs, T. *et al.* Working Principle of an Ionic Liquid Interlayer During Pressureless Lithium Stripping on $Li_{6.25}Al_{0.25}La_3Zr_2O_{12}$ (LLZO) Garnet -Type Solid Electrolyte. *Batteries & Supercaps* **4**, 1145-1155 (2021).

59 Örnek, C., Leygraf, C. & Pan, J. On the Volta potential measured by SKPFM–fundamental and practical aspects with relevance to corrosion science. *Corros. Eng. Sci. Technol.* **54**, 185-198 (2019).

60 Mascaro, A. *et al.* Measuring spatially resolved collective ionic transport on lithium battery cathodes using atomic force microscopy. *Nano Lett.* **17**, 4489-4496 (2017).

61 Harrison, J. S. *et al.* Noncontact Imaging of Ion Dynamics in Polymer Electrolytes with Time-Resolved Electrostatic Force Microscopy. *ACS Nano* **13**, 536-543 (2018).

62 Giridharagopal, R. *et al.* Time-resolved electrical scanning probe microscopy of layered perovskites reveals spatial variations in photoinduced ionic and electronic carrier motion. *ACS Nano* **13**, 2812-2821 (2019).

63 Schirmeisen, A. *et al.* Probing ion transport at the nanoscale: Time-domain electrostatic force spectroscopy on glassy electrolytes. *Phys. Rev. Lett.* **85**, 2053-2055 (2004).

64 Kohn, P., Schröter, K. & Thurn-Albrecht, T. Interfacial polarization and field-induced orientation in nanostructured soft-ion conductors. *Phys. Rev. Lett.* **102**, 216101 (2009).

Chapter 4 Evolution of a Space Charge Layer in Solid State Batteries

4.1 Introduction

All-solid-state batteries (ASSBs) are potential candidates for next generation batteries. Compared with the commercial lithium (Li) ion batteries, ASSBs have a higher capacity and a wider working voltage window[1]. The usage of solid electrolyte instead of liquid electrolyte in ASSBs can prevent Li dendrites growth and improve battery safety[2]. However, switching from a liquid-solid to a solid-solid interface between the solid electrolyte and the electrodes in ASSBs poses additional interfacial challenges, which currently limit the product launch of ASSBs. The main interfacial limitations in ASSBs include 1) a poor physical contact, 2) interfacial side reactions upon cycling[3,4] and 3) the built-up of a space charge layer[5,6].

Both interfacial physical contacts and side reactions have been strongly investigated in recent years[7,8]. However, the presence, the evolution and the effect of space charge layers in ASSBs are still mysterious, even though different experimental and theoretical investigations have been performed. A space charge layer forms at the interface due to a redistribution of charge carriers near the interface arising from a different chemical potential of charge carriers in the electrode and the solid electrolyte after contact[9,10]. Electrochemical impedance spectroscopy (EIS) [11], density functional theory (DFT) calculation[12,13], in-situ differential phase contrast scanning transmission electron microscopy (DPC-STEM) [14], two-dimensional nuclear magnetic resonance (NMR) [10] and electron holography (EH) lead to contradictory conclusions[15]. For example, Jun Haruyam et al used density functional theory (DFT) + U calculation method to outline that a space charge layer at a $LiCoO_2$ (LCO)|Li_3PS_4 interface correspond to a higher Li-ion concentration at the Li_3PS_4 side[16]. In contrast, calculations based on Maier's classical space charge layer model suggest that a higher Li-ion concentration should be present in LCO side[17]. Quantitative electron holography (EH) exhibits a thickness of a space charge layer between a LCO positive electrode and a $Li_{1+x+y}Al_yTi_{2-y}Si_xP_{3-x}O_{12}$ solid electrolyte which spans over 1 µm[15]. This thickness is much higher than the nm-thickness of a space charge layer estimated by Poisson-Boltzmann equation based on the Gouy-Chapmann theory[18]. A nm-thick space

charge layer is also supported by some experimental results[19]. In addition to the debate on the structure and thickness of the space charge layer, the effect a space charge layers on the performance of ASSBs is debated. On one hand, a space charge layer in ASSBs may hamper Li ion transport significantly. Thus, materials and/or interfaces need to de designed to eliminate the additional space charge layer resistance[14,20,21]. On the other hand, Masakazu Haruta et al. and Ohnishi Tsuyoshi et al. mentioned that the resistance originating from a space charge layer is small compared with other battery internal resistances[22,23]. The above-sketched debates motivated us to investigate and clarify the evolution of a space charge layer quantitatively in ASSBs, which may be voltage dependent.

In our view, the main challenge for space charge layer investigation in ASSBs is the lack of a suitable high spatial resolution and non-destructive detection techniques. The technique needs to be used operando while charging or discharging the battery. Almost all presently applied methods have shortcomings. For example, traditional electrochemical characterization and some advanced NMR methods have a low spatial resolution and are unable to resolve the contribution of different interfaces. We overcome these limitations by two techniques: advanced, non-destructive high-spatial resolution operando Kelvin probe scanning microscopy (KPFM) and operando neutron reaction analysis (NRA). Combination both techniques enable observing and analyzing the origin and evolution of a space charge layer in ASSBs. We choose a Li| LPO (Li_3PO_4)|LCO thin film battery as model system because Li, LPO and LCO are the most representative negative electrode, solid electrolyte and positive electrode material, respectively. Furthermore, a thin film battery has well defined interfaces between electrodes and solid electrolytes[24]. In addition, interfaces in Li| LPO|LCO thin film battery are free from interfacial physical contact and side reaction problems[22,25,26], which are typically a major obstacle for space charge layer quantitatively characterization[27,28]. In summary, the combination of those characterization methods broaden the avenues for investigation of space charge layers in ASSBs.

Here, we report that a space charge layer only exists at the LPO|LCO interface in a Li|LPO|LCO battery. By increasing the battery voltage, the space charge layer evolves from Li ions gradually accumulation from the LCO side and depletion in the LPO side close to LCO|LPO

interface. At battery working voltages ranging from 3.85 V to 4.3 V, the magnitude of the space charge layer and the corresponding resistance in LPO|LCO monotonically increases. The maximum space charge layer resistance in Li|LPO|LCO thin film battery is around 35 Ω cm^2 at 4.3 V. The latter is of major significance and accounts for 70 - 80% of the entire interfacial resistance in a Li|LPO|LCO thin film battery.

4.2 Characterization of thin film battery

The structure of the model battery is Li|LPO|LCO|Au|Al_2O_3 (Figure 4.1). The Li layer is the negative electrode, the LPO layer is the solid electrolyte, LCO is the positive electrode, Au is the current collector and Al_2O_3 is the substrate. With this thin film model battery, we obtain two well-defined electrode|solid electrolyte interfaces, corresponding to the Li|LPO and the LPO|LCO. In particular, the Li|LPO and LPO|LCO interfaces are stable and cause only a negligible chemical side reaction, if at all[26,29]. In addition, our previous studies show both interfaces are free from physical defects owing to the applied vacuum deposition methods[22,23,25].

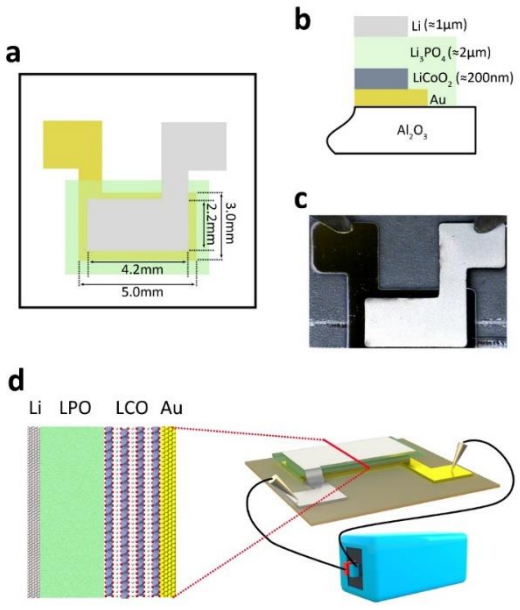

Figure 4.1 a Morphology and size of our Li|LPO|LCO|Au thin film model battery. **b** Schematic diagram of the thickness of different layers in our thin film battery. **c** Photo of the prepared thin film battery. **d** Schematic diagram of a Li|LPO|LCO model thin film battery device connected with a potentiostat.

In the beginning, we investigate if an initial space charge layer at the battery internal interfaces will be present before charging-discharging in the freshly prepared thin film battery. At this stage, the battery voltage is around 2 V vs Li/Li^+. We performed synchrotron X-ray photoemission spectroscopy (SXPS) at the LPO|LCO interface to compare energy band alignments of a pristine LCO surface and of LCO that was coated by a 20 nm thick LPO layer (Figure 4.2a). The SXPS spectra shows that both Co3p and $Co2p_{3/2}$ emissions shifted by about 300 meV towards higher binding energy for the LPO|LCO interface (Figure 4.2b-c). This shift is almost the same as reported for LCO after being coated with LiPON[20]. Such a shift to higher binding energies indicates a band bending of LCO at LPO|LCO interface towards lower energies (Figure 4.2d). Thus negative charges accumulate at the LCO side close to the LPO|LCO interface. At the same time, positive charges accumulates at LPO side close to interface to form a space charge layer (Figure 4.2d) [30].

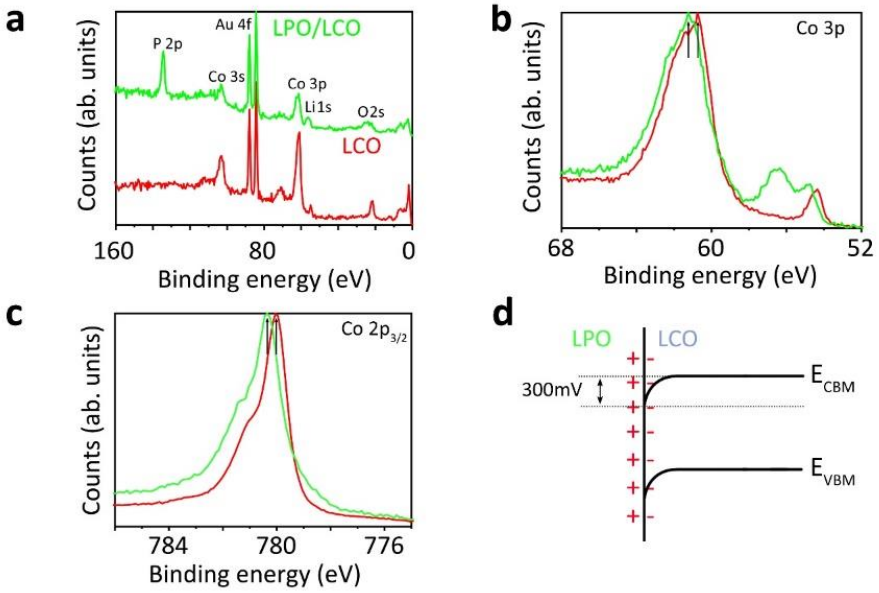

Figure 4.2 a SXPS spectra of pure LCO and LCO coated with a thin LPO film. More detailed SXPS spectra corresponding to the binding energies of **b** Co3p and **c** $Co2p_{3/2}$. **d** Energy band diagram of the LPO|LCO interface.

The formation of space charge layer results from chemical potential difference of Li in LPO layer and LCO layer. In Li|LPO|LCO battery, LPO and LCO with different Li content ($LiCoO_2$ and $Li_{0.5}CoO_2$) have valence band maximums (VBM) far away from each other, it is almost

impossible that electrons (or holes) transfer from one layer into the other layer after contact (Figure 4.3) [10,12,31]. This conclusion is also suitable for Li|LPO interface. Another evidence that electrons (or holes) cannot across LPO|LCO interface is that there is no new phase or interlayer forms after contact[4,26]. Thus, it is reasonable that we assume Li ion is the only kind of mobile charge could across both Li|LPO and LPO|LCO interface in battery. And the observed positive charges accumulate at LPO side in LPO|LCO is Li ions and negative charges accumulate at LCO side is Li vacancies.

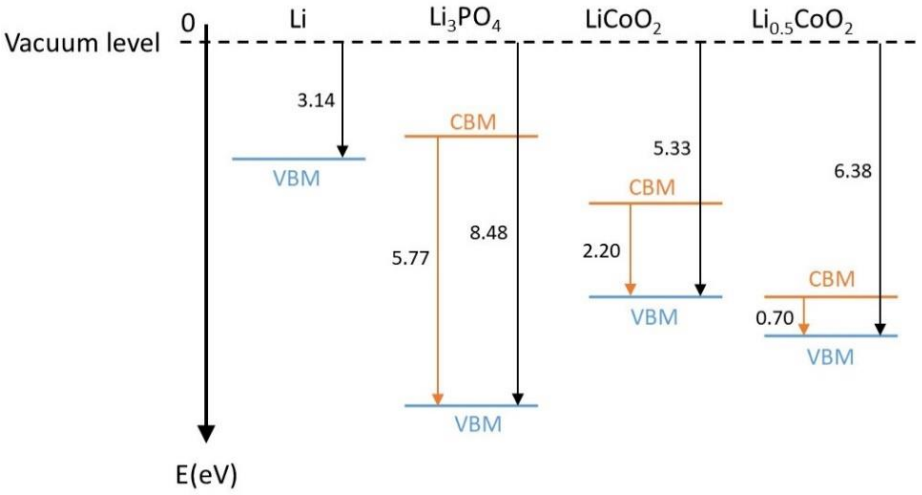

Figure 4.3 The vacuum-aligned of the electronic bands in metal Li, Li_3PO_4, $LiCoO_2$ and $Li_{0.5}CoO_2$ before contact. Blue lines are valence band maximum (VBM) and conduction band minimum (CBM) of different materials.

In order to investigate the Li|LPO interface, we prepared a Li|LPO|Li_xAu cell and performed EIS measurement. The result shows that there is only one semicircle in the high frequency range (>10^3 Hz) in the Nyquist plot, which corresponds to the bulk resistance of the solid electrolyte LPO[32]. Therefore, the interfacial resistance is negligible in the initial state (Figure 4.4). Consequently, the space charge layer resistance, the charge transfer resistance and the resistances arising from physical defects or side reaction are all so small that can be ignored.

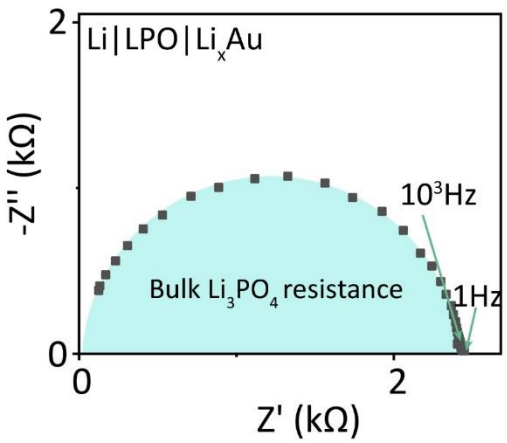

Figure 4.4 Nyquist plot of a Li|LPO|Li_xAu cell.

In order to explore the dynamic evolution of space charge layers, the thin film battery needs to be charged or discharged to different voltages. Charge-discharge curves (Figure 4.5a) and Cyclic voltammetry (CV) experiments (Figure 4.5b) of the Li|LPO|LCO thin film battery show the typical plateaus or peaks of Li ions extracting from (charging) and inserting into LCO (discharging), respectively. The thin film battery exhibits almost overlapping charge-discharge curves and CV curves even after the 80th cycle compared with the 1st cycle. Over 99.5% battery capacity remains (Figure 4.5c). Thus, the LCO and the internal interfaces are stable during cycling. This stability indicates that both interfaces in the thin film battery have negligible resistance comes from physical defects or do not undergo side reactions during battery cycling. Thus in the charged state, the interfacial resistance in our model thin film battery may only originate from three possible contributions: charge transfer resistance in LPO|LCO interface and possible space charge layer resistance in both LPO|LCO and Li|LPO interface.

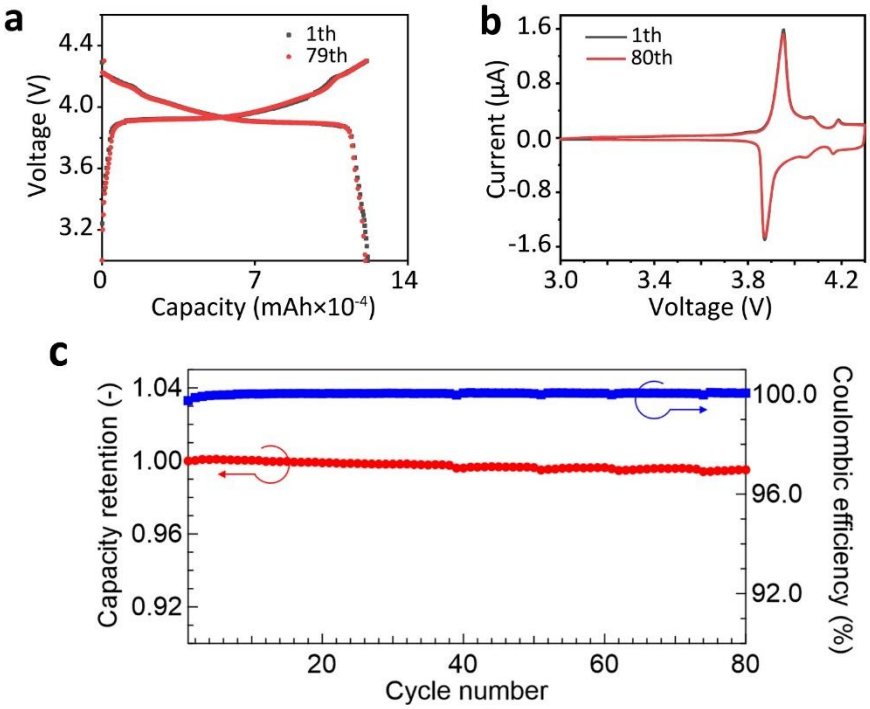

Figure 4.5 a Charging-discharging curves at 0.1 mA|cm^2 of a Li|LPO|LCO thin film battery at the 1st and the 80th cycle. **b** CV Measurement of a thin film battery at the 1st and the 80th cycle. **c** Cycling performance of a thin film battery.

In-situ EIS was then used to study the interfacial resistance evolution while the Li|LPO|LCO battery voltage increases (Figures 4.6a and 4.6b). In the high-frequency range (>10^3 Hz) of the Nyquist plots, we measured the same semicircle as for a Li|LPO|Li_xAu cell. The latter corresponds to the bulk resistance of the solid electrolyte LPO[32]. All those semicircles recorded at different battery voltages overlap, indicating a constant bulk conductivity of LPO. In the mid- and low-frequency range (< 10^3 Hz) and at voltages < 3.6 V, the battery behaves like a capacitor. At these voltages, almost no Li ions cross interfaces. When the battery is charged to > 3.6 V, another semicircle in mid- and low-frequency gradually develops, which turns to a fully semicircle at 3.85V. We attribute this semicircle to an interfacial resistance[22].

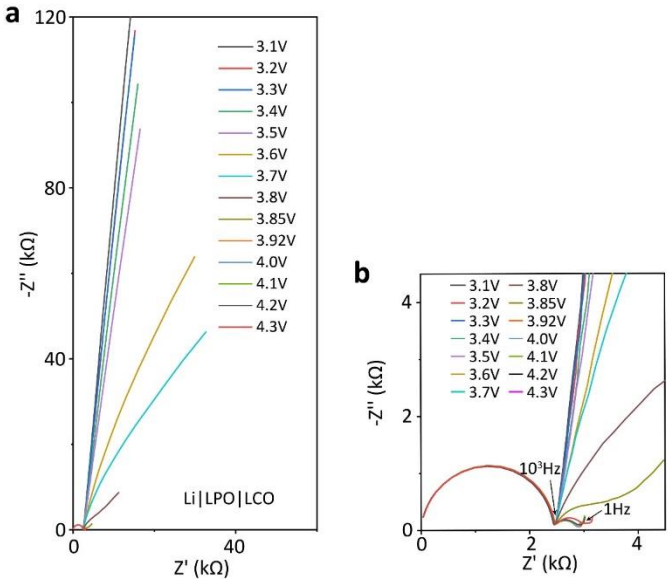

Figure 4.6 a Nyquist plots of a Li|LPO|LCO thin film battery at different battery voltages. **b** Magnification of the Nyquist plots in the high- and mid-frequency range in **a**.

We fitted the Nyquist plots from 3.6 V to 4.3 V with an equivalent circuit – a resistor in parallel with a capacitor in the high- and mid-low-frequency range separately. Fitting leads to a LPO bulk resistance of 2457 Ω +/- 25 Ω, which remains constant for all state of charge (SOC) (Figure 4.7). In addition, we calculated the average ionic conductivity of 8.8×10^{-7} S cm^{-1} for the LPO electrolyte with EIS results. This value matches well with reported values[33,34]. The interfacial resistance decreases from around 0.3 MΩ at 3.6 V to 403 Ω at 4.0 V and then slightly increases to around 508 Ω at 4.3 V. Thus, the lowest interfacial resistance per unit area is around 37 Ω cm^2 at 4.0 V, reaching almost the low values recently reported[23]. The voltage of 4.0 V corresponds to a lithiation degree x ≈ 0.665 in Li_xCoO_2 (Figure 4.7), which is calculated from charge-discharge curves in Figure 1g and the conclusion that x is around 0.55 in Li_xCoO_2 at 4.2 V vs. Li/Li$^+$[34,35]. Then the interfacial resistance increases again slightly with battery voltage.

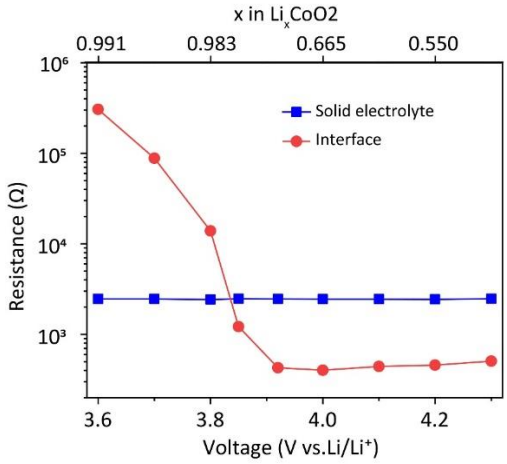

Figure 4.7 LPO bulk resistance and interfacial resistances extracted by fitting the data from Figure 4.6.

This evolution of the thin film battery interfacial resistance is reversible with decreasing battery voltage (Figure 4.8).

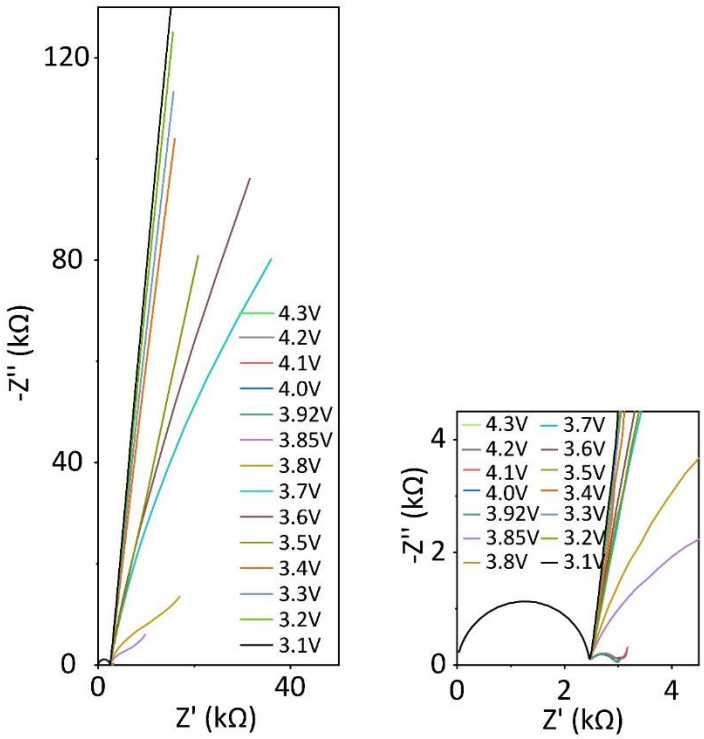

Figure 4.8 Nyquist plots of a thin film battery which is being discharged from 4.3 V to 3.1 V. **a** Whole frequency region. Magnification of the Nyquist plots in the high- and mid-frequency range in **a**.

The evolution of a space charge layer resistance in a battery can be acquired by comparing the difference between the measured overall interfacial resistance and the theoretical calculated LPO|LCO interfacial charge transfer resistance. At the LPO|LCO interface the following reversible intercalation reaction in the LCO electrode takes place:

$$(1-x)Li^+ + (1-x)e^- + Li_xCoO_2 \overset{reversible}{\Longleftrightarrow} LiCoO_2 \quad (1)$$

Where x has a value between 0 and 1. The reaction rate of Li ion insertion (r_i) and Li ions extraction (r_e) from LCO host can be expressed by[36-38]:

$$r_i = k_i c_{max}(1-x)[Li^+] \quad (2)$$

$$r_e = k_e c_{max} x \quad (3)$$

k_i is the insertion reaction rate constant, k_e is the extraction reaction rate constant, c_{max} is the maximum Li ions insertion concentration in LCO and $[Li^+]$ is the bulk Li ions concentration in LPO.

At a formal potential E^0, k_i^0 and k_e^0 are determined by the reaction activation energy according to the Arrhenius equation:

$$k_i^0 = A_i exp(-G_i^0/RT) \quad (4)$$

$$k_e^0 = A_e \exp(-G_e^0/RT) \quad (5)$$

A_i and A_e are prefactors for Li ion insertion and extraction reaction, respectively. G_i^0 and G_e^0 are the activation energies for Li ion insertion and extraction reaction.

We use Frumkin's isotherm for describing Li ion insertion into and extraction from LCO. Frumkin's isotherm considers the interaction between Li ions and the LCO host[39]. Then we define the change of molar intercalation energy as $\Delta\mathrm{G}$, which results from Li ion insertion into LCO. When a potential E is applied to the electrode, the activation energy of Li ion insertion (G_i^E) and extraction reaction (G_e^E) can be written as:

$$G_i^E = G_i^0 - \alpha(FE + \Delta\mathrm{G}) \quad (6)$$

$$G_e^E = G_e^0 + [(1-\alpha)(FE + \Delta\mathrm{G})] \quad (7)$$

α is the transfer coefficient and F is Faraday constant.

Then k_i the insertion reaction rate constant and k_e the extraction reaction rate constant change to:

$$k_i = k_i^0 \exp[\frac{-\alpha(FE+\Delta G)}{RT}] \quad (8)$$

$$k_e = k_e^0 \exp[\frac{(1-\alpha)(FE+\Delta G)}{RT}] \quad (9)$$

From equation 2, 3, 8 and 9, we can calculate the total reaction faraday current as:

$$i = FAc_{max}(1-x)k_i^0 \exp\left[\frac{-\alpha(FE+\Delta G)}{RT}\right][Li^+] - F\ c_{max}xk_e^0 \exp[\frac{(1-\alpha)(FE+\Delta G)}{RT}] \quad (10)$$

In equilibrium state, $E = E_e$ total current i is 0, the exchange current i_0 can be written as:

$$i_0 = FAc_{max}(1-x)k_i^0 \exp\left[\frac{-\alpha(FE_e+\Delta G)}{RT}\right][Li^+] = FAc_{max}xk_e^0 \exp[\frac{(1-\alpha)(FE_e+\Delta G)}{RT}] \quad (11)$$

Then

$$i_0 = FAc_{max}[Li^+]^{1-\alpha}(k_i^0)^{1-\alpha}(k_e^0)^{\alpha}(1-x)^{1-\alpha}x^{\alpha} \quad (12)$$

Here, we define the standard reaction rate constant as k_0 at standard potential E_0,

$$k_0 = k_i^0 \exp\left[\frac{-\alpha(FE_0+\Delta G)}{RT}\right] = k_e^0 \exp[\frac{(1-\alpha)(FE_0+\Delta G)}{RT}] \quad (13)$$

$$k_i^0 = k_0 \exp\left[\frac{\alpha(FE_0+\Delta G)}{RT}\right] \quad (14)$$

$$k_e^0 = k_0 \exp\left[\frac{(\alpha-1)(FE_0+\Delta G)}{RT}\right] \quad (15)$$

When we substitute equation 14 and 15 into equation 12,

$$i_0 = FAc_{max}[Li^+]^{1-\alpha}k_0(1-x)^{1-\alpha}x^{\alpha} \quad (16)$$

From the definition of charge transfer resistance,

$$R_{ct} = \frac{RT}{Fi_0} \quad (17)$$

Substituting i_0 in equation 17 with equation 16,

$$R_{ct} = \frac{RT}{F^2 A c_{\max}[Li^+]^{\alpha} k_i^0 (1-x)^{\alpha} x^{\alpha}} exp[\frac{\alpha(FE+\Delta G)}{RT}] \quad (18)$$

For the change of molar intercalation activation energy ΔG, which is related concentration of intercalated Li ions in LCO, can be written as:

$$\Delta G = a + gx \quad (19)$$

Where a is a constant related with interaction between a intercalated Li ion and a host LCO lattice near it, g is the interaction between two adjacent intercalated Li ions[3].

Since Li ions insertion and extraction from LCO is a reversible process, transfer coefficient α=0.5, which is also verified by experiment (ref). Then R_{ct} can be expressed as:

$$R_{ct} = \frac{RT}{F^2 A c_{\max}[Li^+]^{0.5} k_i^0 (1-x)^{0.5} x^{0.5}} exp[\frac{0.5(FE+a+gx)}{RT}] \quad (20)$$

According to M. D. Levi's report, $\frac{g}{RT}$ is around 4.0 in LCO. This means the molar intercalation activation energy increase with Li ion concentration in LCO[7]. Thus, the less Li ion concentration in LCO, the easier for Li ions to intercalate into, which is also follow the results that Li ion diffusivity increases with Li ions concentration decreases in LCO[8].

To further simplify equation 20, we use n to replace all the constant part $\frac{RT}{F^2 A c_{\max}[Li^+]^{0.5} k_i^0} exp[\frac{0.5(FE+a+)}{RT}]$, thus we get:

$$R_{ct} = n \frac{e^{2x}}{(1-x)^{0.5} x^{0.5}} \quad (21)$$

Here, n is constant related to the Faraday constant, gas constant, temperature, surface area of the electrode, maximum Li-ion insertion concentration in LCO, bulk Li-ion concentration in LPO, standard Li-ions insertion reaction rate constant and standard electrode potential under equilibrium. Using equation 21, we plotted x in Li_xCoO_2 vs. R_{ct} (Figure 4.9). In the range of x = 1 to 0.5, R_{ct} monotonically decreases with increasing x. Furthermore, the plot shows that R_{ct} at the LPO|LCO interface has a minimum value at x ≈ 0.191. This finding significantly deviates from our in-situ EIS results that indicates a minimum interfacial resistance at x ≈ 0.665 for the Li|LPO|LCO thin film battery. We attribute the difference between the experimental measured and the theoretical interfacial charge transfer resistance to the

presence of a space charge layer in Li|LPO|LCO thin film battery. This space charge layer is not static but changes dynamically with voltage or lithiation degree in LCO. However, the following questions remain: Can the space charge layers contribution at the Li|LPO and LPO|LCO interfaces be separated? Which charges are responsible for the charge layer? Do the space charge layers depend on the charging state change? Does the space charge layers evolve in strength and polarization direction? Can the space charge layer resistance be calculated? In order to answer those questions, we apply two advanced techniques operando KPFM and operando NRA, which are not common in battery research.

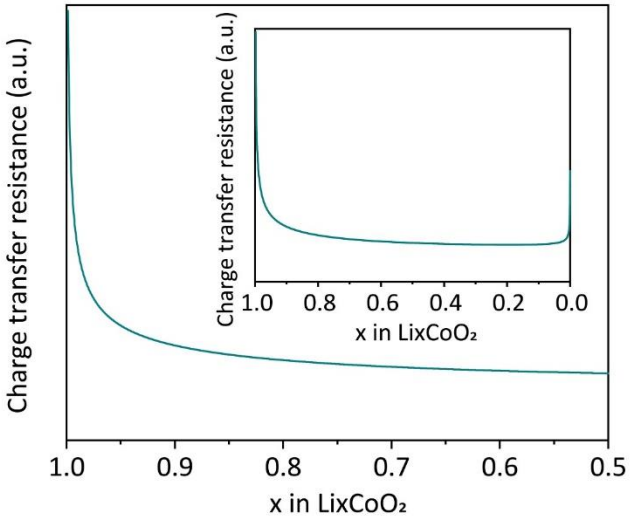

Figure 4.9 Calculation of the LPO|LCO interfacial charge transfer resistance in dependence of the Li ion concentration in LCO.

4.3 KPFM measurements of a thin battery cross-section

KPFM allows mapping the sample's contact potential difference (CPD) with an nm lateral resolution[42-44]. Here we use operando KPFM to investigate the internal potential distribution in a thin film battery at different SOC. For operando KPFM measurements, we firstly broke thin film batteries in two halves to expose the cross-section of battery. Broken surfaces are too rough for KPFM owing to signal crosstalk between topography and CPD[45-47]. Therefore, we used argon-ion milling to polish the exposed cross-section (Figure 4.10a). We performed KPFM measurements on the polished cross-section, while at the same time, a potentiostat is connected to the battery to charge it to different SOC (Figure 4.10b).

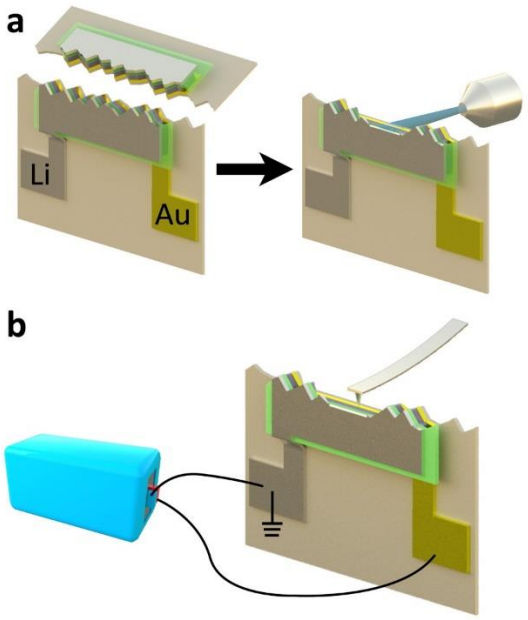

Figure 4.10 a Schematic diagram of breaking and polishing a Li|LPO|LCO thin film battery to form a cross-section. **b** Schematic diagram of operando KPFM on a polished thin film battery cross-section.

Scanning electron microscopy (SEM) results on polished cross-section reveals that interfaces in thin film battery are sharp and straight (Figure 4.11a). The corresponding elemental distribution acquired from energy dispersive X-ray analysis (EDX) mapping confirms that polishing did not lead to mutual contamination or deposition between different layers on polished cross-section (Figure 4.11b).

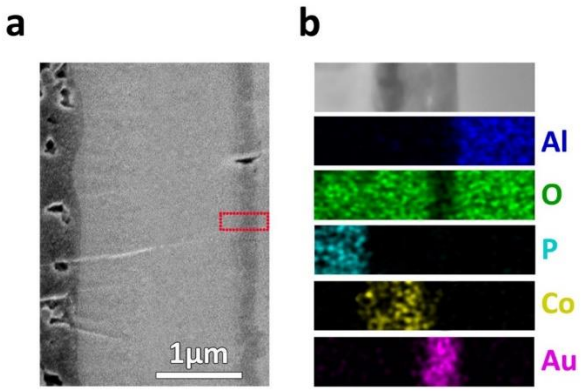

Figure 4.11 a SEM of the polished cross-section. **b** EDX map of the region marked with a red square in **a**.

More important, polishing does not damage the thin film batteries because the peaks in CV curve do not change after polishing (Figure 4.12a). Furthermore, interfacial resistance evolution with battery voltage change keeps the same as unpolished ones (Figures 4.12b and 4.12c).

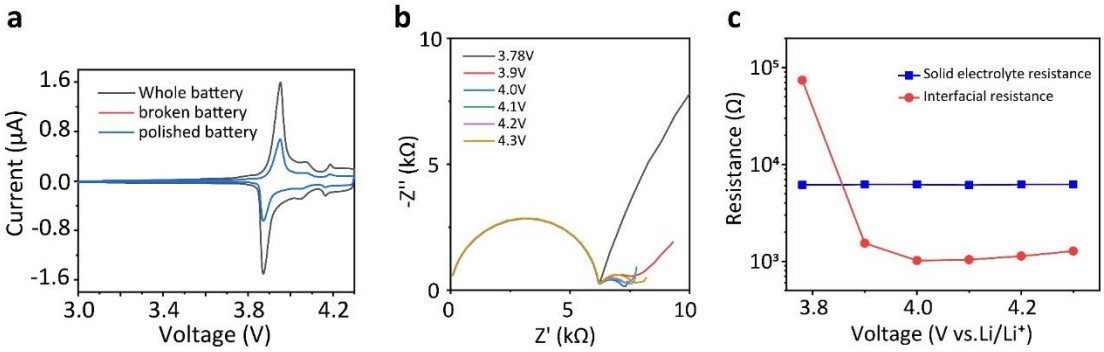

Figure 4.12 a Comparison of CV curves of the same thin film battery before breaking the battery (black line), after breaking in two halves (red line) and after polishing (blue line) at 0.1 mV/s scan speed. CV curves overlaps after breaking (red line) and after polishing (blue line). **b** Nyquist plots of a thin film battery, which is one piece of a battery which was broken in two halves and was polished by Ar ion milling, at different voltages. **c** The fitting solid electrolyte bulk resistance and interfacial resistance of polished battery from **b**.

The topography mapping (Figure 4.13a) and the corresponding phase mapping (Figure 4.13b) of the polished cross-section acquired from KPFM measurements also clearly display different layers. As expected, the thickness of LPO layer and LCO layer are 2500 nm and 200 nm, respectively. After polishing, the surface roughness of each layer is <3 nm.

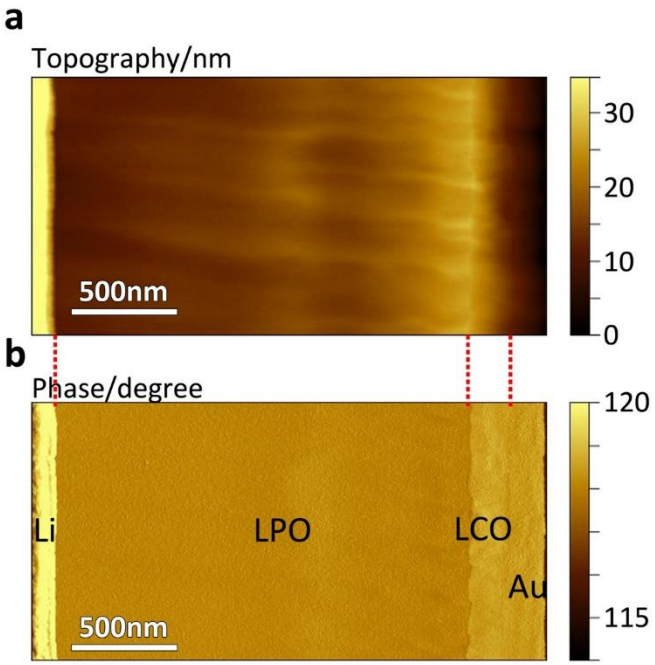

Figure 4.13 a Topography and **b** phase map of the polished Li|LPO|LCO thin film battery cross-section.

Next, we performed operando KPFM measurements. The CPD maps of the whole battery cross-section at 3.0 V and 4.3 V show CPD changes at the LCO and the Au layer (Figures 4.14a and 4.14b). Additional measurements along the whole battery cross-section in the voltage range from 3.0 V to 4.3 V in steps of 0.1 V confirm this conclusion (Figure 4.14c). In particular, the CPD value of Li negative electrode remains constant at ≈ 2.55 V. Li is a metal and is connected to ground in our measurements. Thus the measured CPD value equals to the work function difference between the Pt-Ir coated tip ($\Phi_{Pt|Ir} \approx 5 - 5.93\ V$) and the one of Li ($\Phi_{Li} \approx 2.9\ V$). In addition, the CPD of the LPO layer remains constant at ≈ 2.85 V. Differently, the CPD values of LCO and Au layer continuously change with battery voltage.

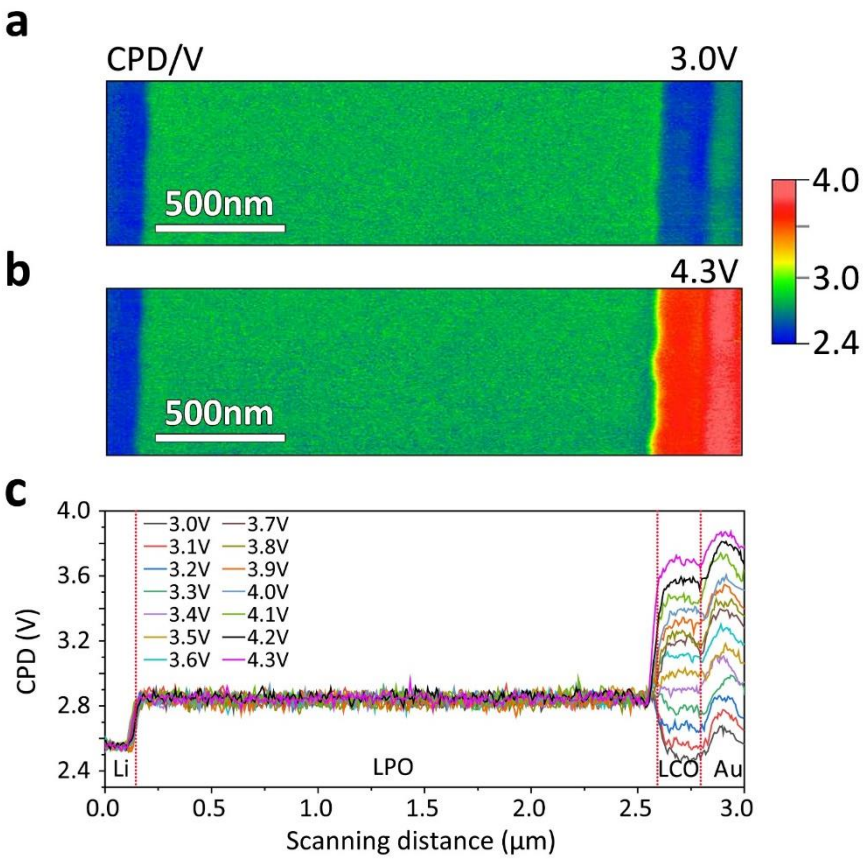

Figure 4.14 a and **b** CPD maps of the polished Li|LPO|LCO thin film battery cross-section at 3.0 V and 4.3 V battery voltages, respectively. **c** Corresponding line profiles of the CPD at 14 different voltages.

The constant CPD value of the Li and LPO layer reveal that the Galvani potential φ of both layers are fixed in the entire voltage operating range of the battery[48]. In combination with the above finding that the interface space charge layer resistance is negligible in a Li|LPO|Li_xAu cell, we conclude that no space charge layer at the Li|LPO interface forms for a Li|LPO|LCO thin film battery in the entire voltage operating range of the battery. Thus, the space charge layer resistance in the Li|LPO|LCO thin film battery is only related to the space charge layer at the LPO|LCO interface. In order to trace these changes at the LPO layer with higher resolution, we decreased the scan size of the KPFM measurements to 500 nm and only measured the LPO|LCO interface.

4.4 KPFM measurement at the LPO|LCO interface

The high-resolution KPFM measurements consolidate a constant CPD value of the LPO layer. The CPD value of LCO continuously increases with battery voltage, which is represented by the change from a blue to a red color in Figure 4.15a. The corresponding CPD profiles across the LPO and the LCO layer are plotted in Figure 4.15b. Such an evolution of measured CPD with battery voltage is fully reversible and is present even after 80 charging-discharging cycles. Thus, the evolution is caused by mobile charges and we can exclude parasitic effects such as interface reactions at the cross-section surface.

The CPD profiles indicate a transition region between the LPO and the LCO layer with a width of around 50 nm (marked with white background in Figure 4.15b). There is a difference in polishing rate of LPO and LCO. Thus, a characteristic kink in the topography was created at the transition from LPO to LCO (height signal in Figure 4.15b). This kink and different material properties of LPO and LCO lead to a phase change of the resonating cantilever (phase signal in Figure 4.15b). We conclude that the width of the space charge layer must be smaller than 50 nm at the LPO|LCO interface, considering a lateral resolution of KPFM of tens of nanometers.

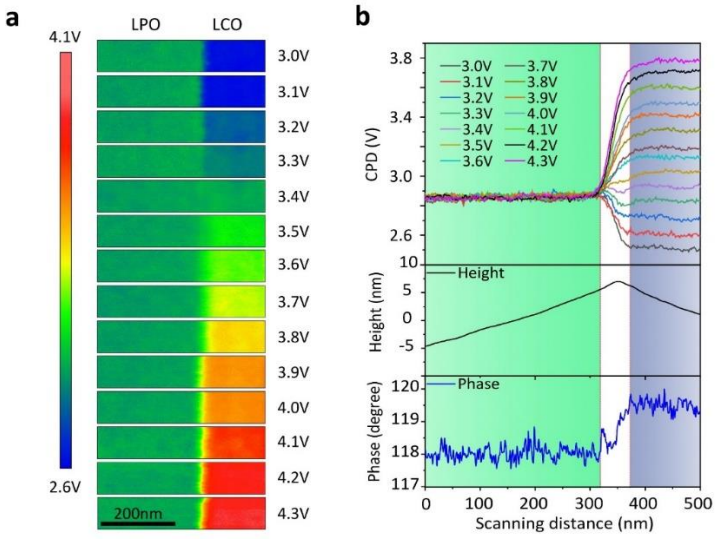

Figure 4.15 a CPD maps of the LPO and LCO layer at different battery voltages. **b** CPD line profiles at different battery voltages and the corresponding height and phase line profiles across the LPO and LCO layer.

In our KPFM measurements, the cantilever is electrically connected to the Li negative electrode which is connected to ground but not LPO or LCO. In this case the measured CPD on LPO or LCO is related to the Volta potential ψ of the LPO or LCO[48]. Thus, the measured CPD change (ΔCPD) corresponds to the Volta potential change $\Delta\psi$, which is composed of changes in the work function ($\Delta\Phi$) and changes in the electrochemical potential of electrons ($\Delta\tilde{\mu}_e$):

$$\Delta CPD = \Delta\psi = \frac{\Delta\Phi + \Delta\tilde{\mu}_e}{e} \quad (22)$$

We quantitatively analyze the ΔCPD on the LPO and the LCO layer at different battery voltages (Figure 4.16). The CPD change of the LPO layer (ΔCPD_{LPO}) remains constant 0 V. Then, the work function change of LPO ($\Delta\Phi_{LPO}$) and the electrochemical potential change of electrons ($\Delta\tilde{\mu}_{e,LPO}$) are both 0 V. In contrast, the CPD change of the LCO layer (ΔCPD_{LCO}) is directly proportional to the changes in the battery voltage with a slope of 1. Thus, ΔCPD_{LCO} is equal to the electrochemical potential change of electrons in LCO ($\Delta\tilde{\mu}_{e,LCO}$) and the work function change of LCO ($\Delta\Phi_{LCO}$) is 0 at any battery voltage.

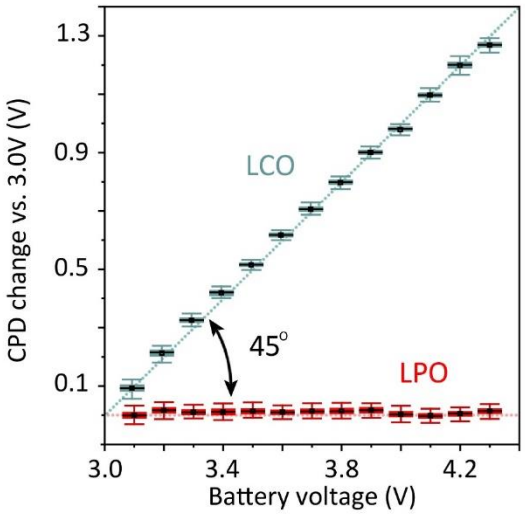

Figure 4.16 CPD mean values calculated from all the pixels on the LCO and LPO layer surface at different battery voltages. In this analysis we exclude the LPO|LCO transition region.

We confirmed a constant work function of LCO (Φ_{LCO}) with KFPM measurements on a simply broken LCO surface without argon ion milling. Only breaking a thin film battery results in a

rough surface of the cross-section, which complicates finding the interface between the LPO and the LCO layer (Figures 4.17a – b). More important, a rough surface decreases the KPFM resolution (Figures 4.17c – e). The KPFM measurement on rough surfaces show that, we can distinguish the LPO and the LCO layer from CPD values. However, the width of the transition region increases to around 100 – 150 nm. For polished cross-sections we measured a width of 50 nm (Figure 4.17f). We emphasize that unpolished LPO and LCO surfaces of a cross section show the same CPD values as polished surfaces for the same battery voltage, which also means a constant Φ_{LCO} on a unpolished LCO surface. This indicates that argon ion milling does not bring additional damage on LPO and LCO surface.

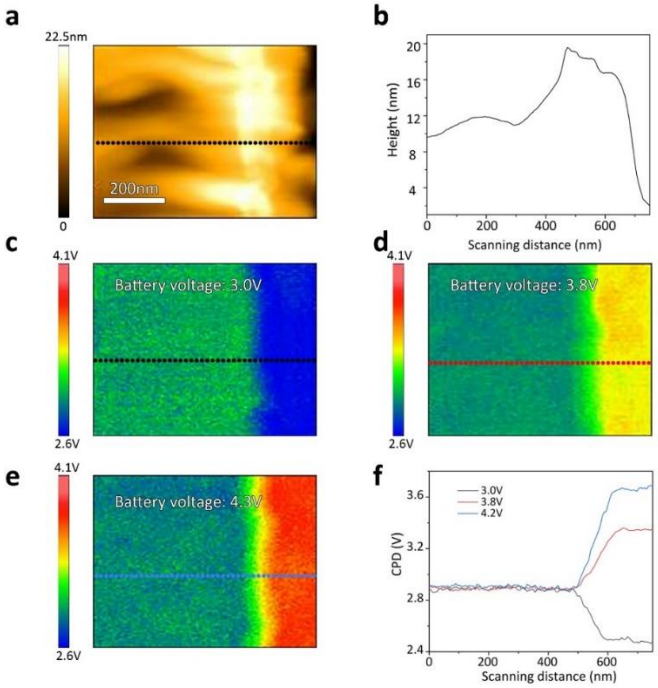

Figure 4.17 a Topography of a thin film battery cross-section, which was prepared by breaking only. The surface is much rougher compared to an ion polished surface. The surface that is imaged by KPFM includes the LPO and the LCO layer. **b** Topography line profile along dark dotted line in **a**. **c-e** Measured CPD maps of the same surface in **a** at a battery voltage of 3.0 V, 3.8 V and 4.3 V respectively. **f** CPD line profiles along dash lines in **c-e**.

We further verified the conclusion of constant $\Delta\Phi_{LCO}$ by connecting the LCO to ground and performing KPFM measurements at different battery voltages. Now, both, the LCO and Au layer are connected to ground and the counter electrode and Li is connected to the working

electrode of the potentiostat (Figure 4.18a). The LCO is a good electron conductor and the electrochemical potential of electrons in LCO and Au are fixed. Now, all the measured CPD changes on the LCO and Au layer result from work function changes. In this configuration, we measured a constant CPD of LCO for battery voltages ranging from 3.0 V to 4.3 V (Figure 4.18b). Results indicate a constant Φ_{LCO} with battery voltage. Interestingly, a constant Φ_{LCO} was also observed as well by Elliot J. Fuller et al. in a recent KPFM experiment[49].

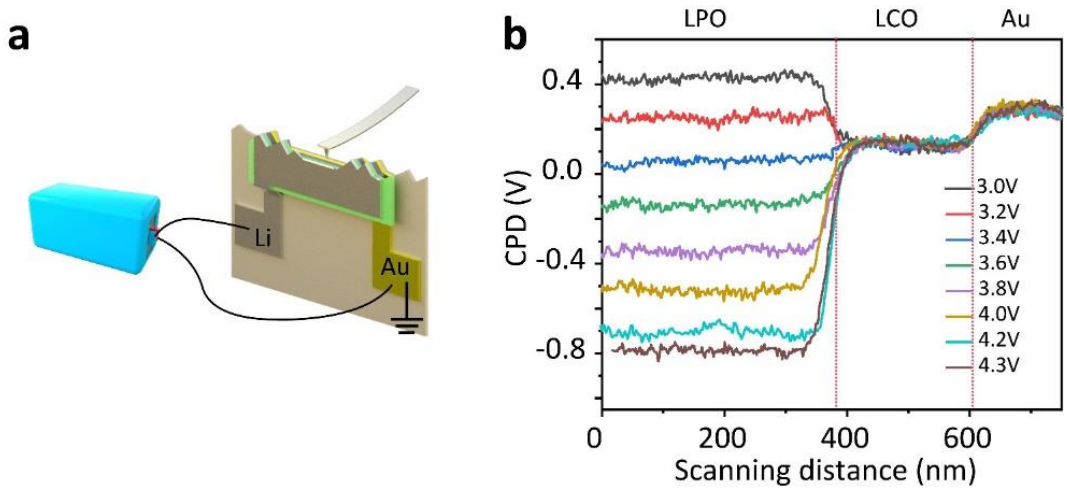

Figure 4.18 a Schematic drawing of the KPFM measurement on the cross-section of a thin film battery. The Li electrode is connected to the working electrode and the Au layer is connected to the counter electrode of the potentiostat and ground. **b** CPD line profiles recorded along the cross-section of the thin film battery with electrical connection shown in **a**.

At voltages <3.85 V, Li ions almost cannot extract from LCO resulting in a constant Φ_{LCO}. However, at voltages >3.85 V, Li ions begin to extract from LCO and Φ_{LCO} should not be constant any more. Our DFT calculations show an increase Φ_{LCO} with battery voltage increase when voltages >3.8 V (Figure 4.19).

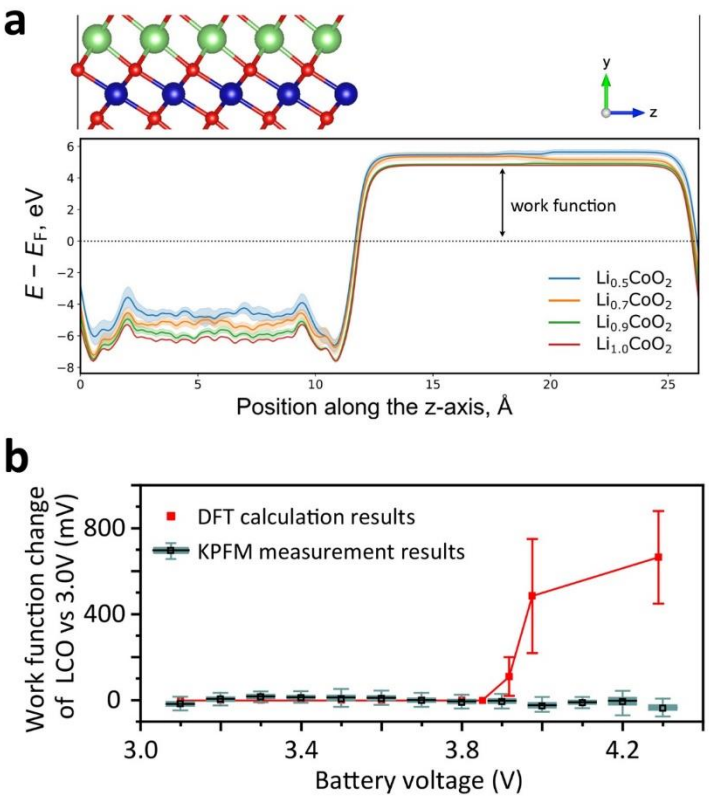

Figure 4.19 a (Top) The illustration of the (100) surface of Li_xCoO_2 with a 15 Å thick vacuum slab. In the simulations Li atoms are randomly removed directly from both surface and bulk LCO. (Bottom) The averaged potential energy (subtracted by the Fermi energy) of Li_xCoO_2 as a function of the z position. The work function is obtained from the difference between the vacuum potential energy and the Fermi energy. **b** Comparison of work function changes of the LCO layer, which are acquired from DFT calculations and KPFM measurements respectively.

In order to understand the reason of work function evolution difference with battery voltage between KPFM and DFT calculation, we performed further DFT calculations by comparing Φ_{LCO} change under the situation of Li ions only extracting from LCO bulk part and the situation of Li ions only extracting from LCO very surface layer. Results show that if LI ions only extract from LCO bulk part, Φ_{LCO} is constant and does not change with x in Li_xCoO_2 (Figure 4.20a). However, if Li ions extract from LCO surface layer, Φ_{LCO} increases compared with the situation that Li ions only extract from LCO bulk part (Figure 4.20b). Thus we conclude that Li ions do not extract from the very surface of the LCO even battery voltage is over 3.85

V (Figure 4.20c). Possibly, the energetic barrier for Li ion extraction from the surface is much higher compared to bulk LCO because of the effect such as surface dipole[50].

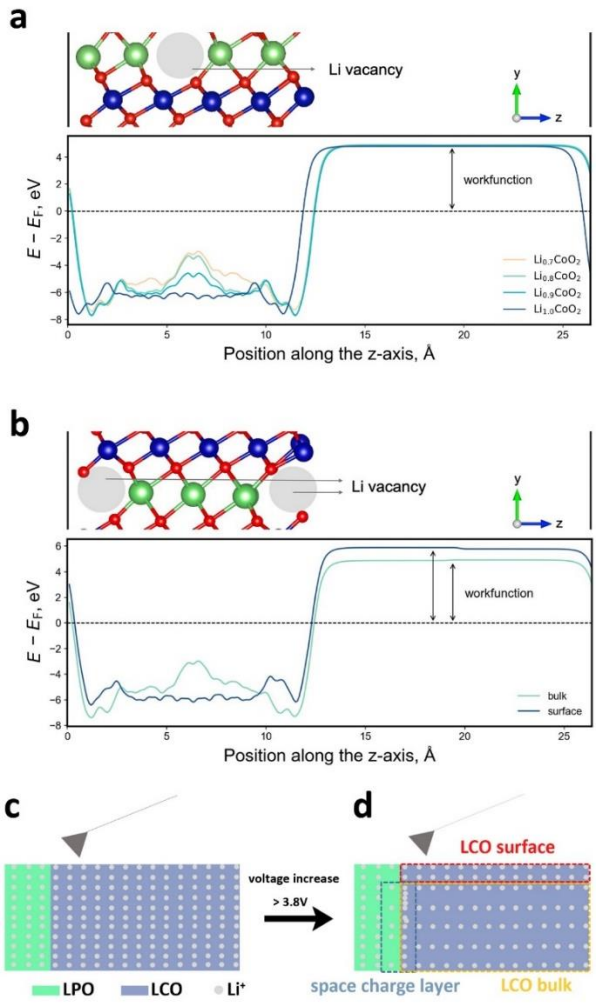

Figure 4.20 a (Top) The illustration of the (100) surface of Li_xCoO_2 with a 15 Å thick vacuum slab, where Li atoms are only removed from LLZO bulk part but not surface. (Bottom) The averaged potential energy (subtracted by the Fermi energy) of Li_xCoO_2 as a function of the z position. **b** (Top) The illustration of the (100) surface of $Li_{0.7}CoO_2$ with 15 Å vacuum slab, where Li atoms are removed from both sides of the LLZO surfaces but not bulk part. (Bottom) The comparison of averaged potential energy (subtracted by the Fermi energy) of $Li_{0.7}CoO_2$ as a function of the z position under situation of Li ions only being removed from LLZO bulk part and LLZO surface. **c-d** Sketch of a KPFM measurements at LPO|LCO interface for a discharged battery, i.e. voltage > 3.8 V. Li ions does not extract from the very surface layer of LCO as bulk LCO.

In conclusion, for battery voltages ranging from 3.0 V to 3.85 V, the measured Volta potential changes in LCO $\Delta\psi_{LCO}$ equal Galvani potential changes $\Delta\varphi_{LCO}$, because both the surface potential χ_{LCO} and the chemical potential of electrons $\mu_{e,LCO}$ remains almost constant due to the almost constant Φ_{LCO} (Figure 4.21). As a result, we can speculate that φ_{LCO} increases with battery voltage. For battery voltages ranging from 3.85 V to 4.3 V, $\Delta\varphi_{LCO}$ is the sum of $\Delta\psi_{LCO}$ and $\Delta\chi_{LCO}$ (Figure 4.21). However, $\Delta\chi_{LCO}$ cannot be decided because of no delithiation on LCO very surface as bulk LCO part. Therefore, the KPFM measurement in the voltage range of 3.85 V to 4.3 V does not allow us to quantify the increase in Galvani potential of LCO (φ_{LCO}), which is the key factor for a space charge layer at the LPO|LCO interface.

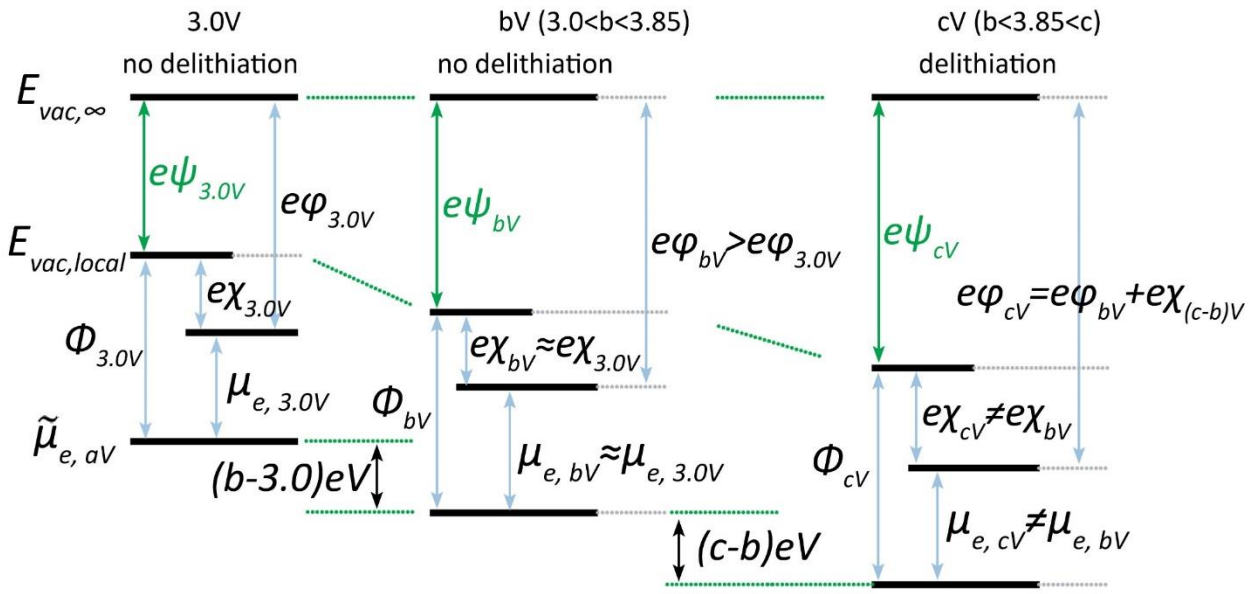

Figure 4.21 Schematic energy diagram of the Volta potential (ψ), surface potential (χ), Galvani potential (φ), work function (Φ) and electrochemical potential (μ̃) of the LCO layer. e_1: at a battery voltage of 3 V, which is taken as reference. e_2: at a battery voltage of b V (3.0<b<3.8), where no delitiation takes place. e_3: at a battery voltage of c V (b<3.8<c), where delitiation takes place.

In the voltage range from 3.0 V to 3.85 V, we define the Galvani potential measured at 3.0 V as a reference ($\varphi_{@3V}$). Then the difference, $\varphi_{LPO} - \varphi_{@3V}$, becomes 0 in bulk LPO, while $\varphi_{LCO} - \varphi_{@3V}$ continuously increases with battery voltage in bulk LCO (Figure 4.22a). This

increase in φ_{LCO} results from an increasing in-built electric field at LPO|LCO interface (Figure 4.22b). From increasing in-built electric field with battery voltage increase, we can decide that, compared with 3.0 V reference state, negative charges gradually accumulate at LPO side close to interface with battery voltage increase while positive charges gradually accumulate at LCO side close to interface (Figure 4.22c).

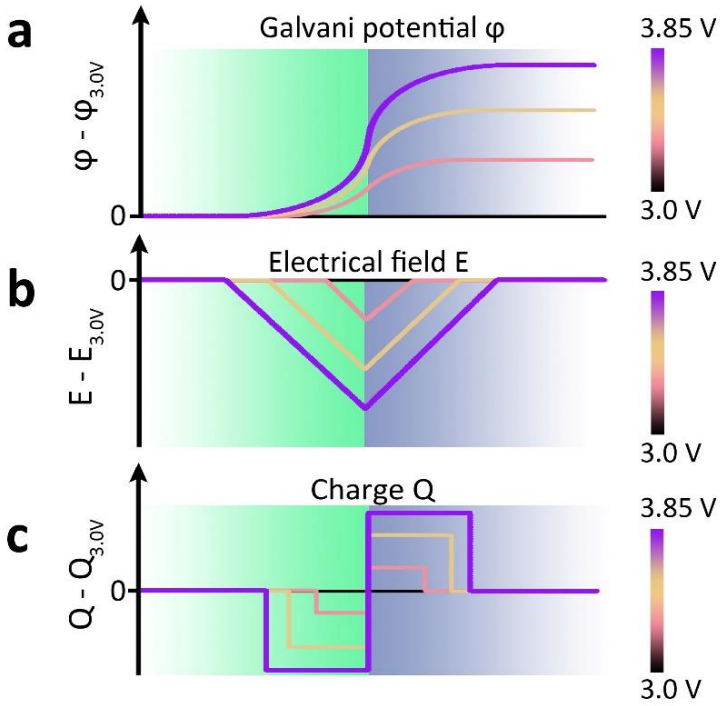

Figure 4.22 Schematic diagrams of **a** the Galvani potential change, **b** the electrical field change and **c** the charge number change at the LPO/LCO interface. All changes relative to a reference voltage of 3.0 V. This schematic is valid for a battery voltage range of 3.0 V – 3.85 V, i.e. where no delitiation takes place.

In 3.0 V to 3.85 V voltage range, Li ions are widely recognized hardly can extract from bulk LCO. Electrons and holes as discussed above that cannot across both Li|LPO and LPO|LCO interfaces. However, we still can observe battery shows very little capacity from charge-discharge curve in Figure 4.5. This results from Li ions in LPO moving to Li electrode surface and being reduced into metallic Li when battery is charged in this voltage range. However, this process is limited because LCO cannot provides enough Li ions move from LCO to LPO side. As a results, Li ions concentration in LPO close to LPO|LCO interface continuously

decrease and leaves Li vacancies with negative charge[21]. To maintain local charge neutrality, limited defects in LCO such as grain boundaries can provide and conduct Li ions in LCO to LPO|LCO interface. In another words, Li ions concentration gradually increases in LCO side close to interface with Li vacancies concentration increase in LPO side close to interface. Both of those Li ions and vacancies change leads in-built electric field change at LPO|LCO interface, which finally increases φ_{LCO} with charging time increase. This conclusion can even be expanded to the voltage range from 2.0 V to 3.0 V with also no Li-ions extracting or inserting into LCO, even though it is not the usual battery working voltage range, because we can observe the CPD value on LCO layer equally increases with battery voltage increase (Figure 4.23).

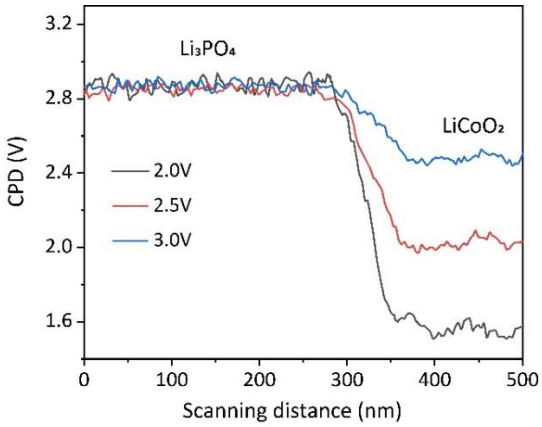

Figure 4.23 CPD line profiles across the LPO|LCO interface at battery voltages of 2.0 V, 2.5 V and 3.0 V, respectively.

To further study space charge layer evolution in 3.85 V to 4.3 V battery voltage range and verify our interpretation of KPFM results in the voltage range from 3.0 V to 3.85 V, we used operando NRA to directly measure the Li concentration evolution at the LPO|LCO interface.

4.5 NRA analysis and theoretical space charge layer calculation

Recently, we developed an *operando* technique using a nuclear reaction analysis (NRA) to probe the depth profile of Li content in thin film batteries with high spatial resolution (Figure 4.24). NRA is based on a H^+ ion beam which is irradiated from the substrate side into the thin film battery. Then H^+ ions react with Li and generate α-particle radiation. The counts and the

energy of α-particles reflect the relative Li density at a specific sample depth. This technique has depth resolution of ~50 nm.

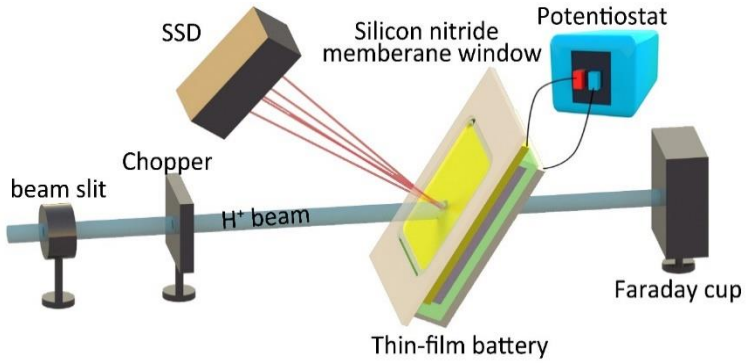

Figure 4.24 Schematic diagram of the operando NRA experiment of a thin film battery.

Figure 4.25 shows the NRA spectra of the thin film battery taken at the voltage of 3.0 V vs. Li/Li^+. We used a multilayer model to fit the experimental NRA spectra. The simulation takes into account the Li content signals in the Li layer (grey), LPO layer (green) and LCO layer (purple) in the thin film battery, respectively.

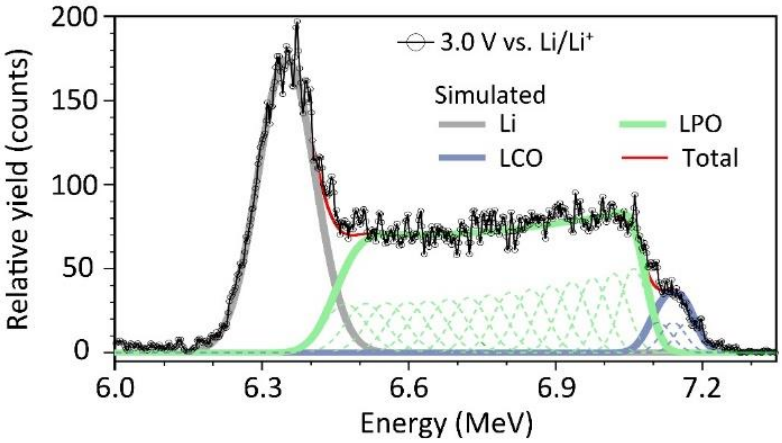

Figure 4.25 NRA signal versus H^+ ion beam energy at 3.0 V. An increasing H^+ ion beam energy leads to a signal from a deeper volume of the battery. The fits of the components, Li, LCO and LPO are provided.

Then we compared NRA results under different battery voltages. Our analysis of the Li content in the LPO at the LPO|LCO interface at different battery voltage indicates no significant difference of the Li content. All Li-content data are within the error range of the measurement, i.e. the change in Li content in LPO is below the NRA detection sensitivity (Figure 4.26a).

However, in the LCO layer, the fitting results show that the overall signal of Li content significantly decreased to ~60 % by charging the battery from 3.0 to 4.3 V vs. Li/Li^+ (Figure 4.26a). The changes of the Li content in the LCO layer with increasing battery voltage (Figure 4.26b) are in good agreement with the results calculated from charge-discharge curve and Möller et al.'s results acquired from particle induced gamma-ray emission analysis (PIGE) [51]. More interestingly, we measured that the peak center of the Li content profile in LCO shifts to towards the LPO|LCO interface upon increasing the battery voltage from 3.0 V to 4.3 V. In order to analyze the peak center position of the Li content more accurately, we fitted three Gaussian curves to the NRA signal of Li in LCO layer (Figure 4.26c). One Gaussian fit corresponds to the Li content in LCO layer close to LPO|LCO interface ($\Upsilon_{LCO,interface}$) while the other two correspond to the Li content in LCO layer far from LPO|LCO interface ($\Upsilon_{LCO,bulk}$). We normalized the ratio $\Upsilon_{LCO,interface}/\Upsilon_{LCO,bulk}$ as 1 at 3.0 V, which continuously increases with battery voltage to ~2.5 at 4.3 V (Figure 4.26c). If we take that Li ion is only kind of charge can transfer across LPO|LCO interface into consideration, this analysis shows that the relative interfacial Li ions concentration in LCO close to LPO|LCO interface region increases with battery voltage in range from 3.0 V to 4.3 V compared with LPO part far from LPO|LCO interface. At the same time, the relative interfacial Li ions (Li vacancies) concentration in LPO side close to interface decreases (increases) with voltage increase.

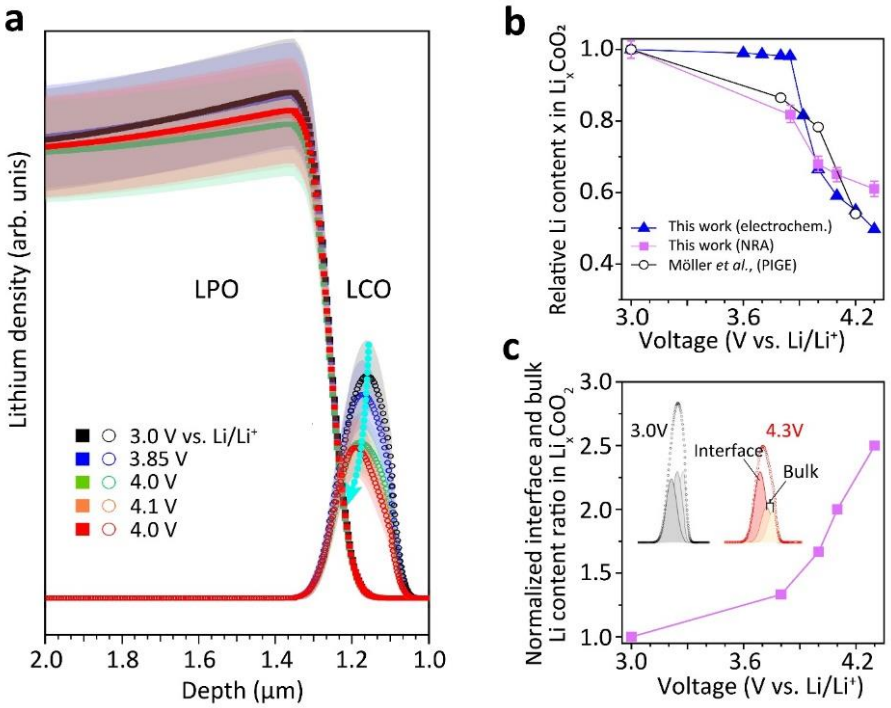

Figure 4.26 a The Li content obtained from the fits at the LPO|LCO interface at different battery voltages. **b** Comparison of LCO bulk Li content change with battery voltage acquired from our NRA results, electrochemical test and reported from PIGE technique[51]. **c** Normalized Li content ratio evolution with battery voltage between in LCO close to LPO|LCO interface and in LCO far from LPO|LCO interface. The ratio at voltage 3.0 V is the reference used for normalization.

From operando NRA results, firstly we can verify that in 3.0 V to 3.85 V voltage range, the evolution of space charge layer in LPO|LCO interface is same as we measured with operando KPFM. Secondly, we prove that space charge layer evolution with battery voltage increase in 3.85 V to 4.3 V voltage range continues the evolution trend with battery voltage in the voltage range of 3.0 V to 3.85 V. In another words, φ_{LCO} increases relative to φ_{LPO} with increasing battery voltage in the whole battery working voltage window.

Different with 3.0 V to 3.85 V voltage range, Li ions can across LPO|LCO interface when battery is charged to over 3.85 V. This means at any voltage over 3.85 V electrochemical potential of Li ions in both LPO and LCO layer are constant and equals with each other under equilibrium state. Since Li ions have been proved the only charge can transfer across LPO|LCO

interface, we can simulate Li concentration distribution at LPO|LCO interface under different battery voltage after 3.85 V based on the model provided by Niek J.J. de Klerk et al[52] and assuming that the equilibrium potential of LPO vs Li/Li^+ is 0.7 V[33]. This simulation mode uses a solid solution model which obeys mass conservation to describe the relationship between Li ion chemical potential and the distance to interface. Li ions chemical is decided by Li ions concentration. The basic parameters for simulations are list in Table 4.1.

Table 4.1 Material parameters for the LPO/LCO interfacial space charge layer calculation

Property	LPO	LCO[52]
C_{max} (Li/nm^3)	76.28	31.6
C_0 (Li/nm^3)	38.14	Depends on voltage
Voltage (vs. Li/Li^+)	0.7, 1.4, 2.1, 2.8, 3.5	3.92, 4.0, 4.1, 4.2, 4.3
ε (relative to ε_0)	5.6	12.9
Ω (eV)	0[52]	0.026
E_M (eV/Li)	5.27[53]	7.00

When battery voltage is over 3.85 V, we simulated space charge layer in LPO|LCO interface at 3.92 V, 4.0 V, 4.1 V, 4.2 V and 4.3 V. The simulations show in LPO|LCO interfacial space charge layer, with voltage increase, Li ions concentration in LPO side gradually decreases while Li ions concentration in LCO side gradually increases (Figure 4.27). The thickness of the simulated space charge layer increases from 0.36 nm to 0.44 nm (inset of Figure 4.27). The conclusion is very consistent with our operando NRA results.

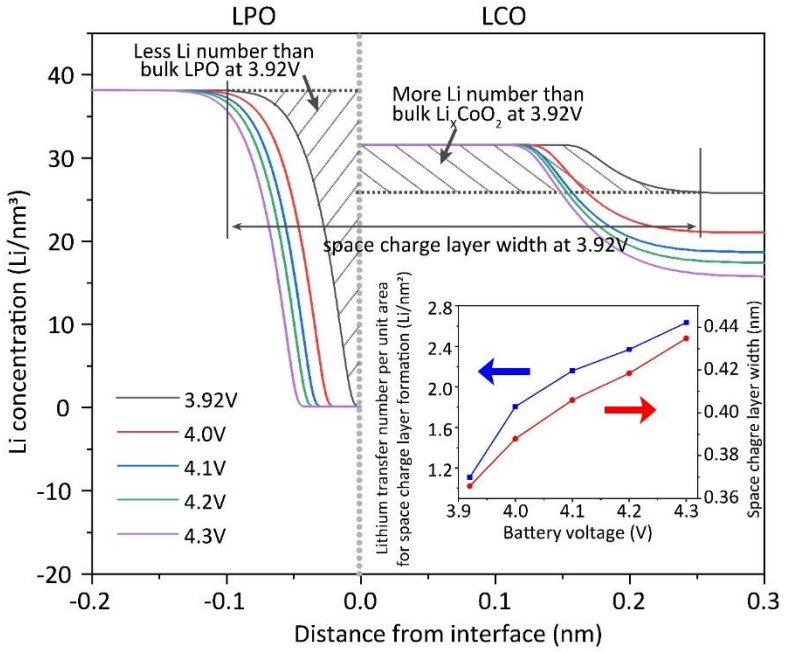

Figure 4.27 Simulation of Li ions concentration profile evolution of space charge layer at LPO|LCO interface with battery voltage. Insert figure shows the evolution of the number of Li ions from LPO to LCO for space charge layer formation and width of space charge layer at LPO|LCO interface with battery voltage change.

4.6 Space charge layer resistance

Based on the above measurements, we are able to clarify the evolution of the space charge layer in our model thin film battery. We depict a simple model (Figure 4.28). The initial state, after preparation of the battery corresponds to a battery voltage of around 2 V. At this state a space charge forms at the LPO|LCO interface by accumulation of Li ions at the LPO side and Li vacancies at the LCO side (Figure 4.28a_1). With increasing battery voltage, the amount of Li ions in LPO close to the interface decreases while Li ions accumulate at the LCO side. Therefore, the space charge layer resistance decreases with increasing battery voltage. Space charge layer is thought of bringing additional barrier for Li ions moving across because of Li depletion existence in solid electrolyte side or electrode side[9,10]. Combining with the above results of continuously space charge layer evolution with battery voltage and the evolution trend, we can decide that space charge layer resistance can decrease to zero, which corresponds to the vanish of space charge layer. At this stage ($V_{no\ SCL}$) all accumulated charges

in LPO and LCO side close to LPO|LCO interface disappear (Figure 4.28a_2). With further increasing battery voltage a space charge layer appears again. Now, Li ions begin to accumulate from the LCO side while at the LPO side, Li vacancies are created (Figure 4.28a_3). At the same time the space charge layer resistance increase again. With even further increasing the battery voltage the space charge layer further increases (Figure 4.28a_4). During the whole voltage range of space charge layer evolution, the direction of the polarization at the interfaces reverses its direction at $V_{no\ SCL}$. Because both operando KPFM and NRA shows the relatively evolution of space charge layer compared with a reference state, $V_{no\ SCL}$ cannot be decided with them. $V_{no\ SCL}$ is important on quantitatively calculating additional resistance from space charge layer.

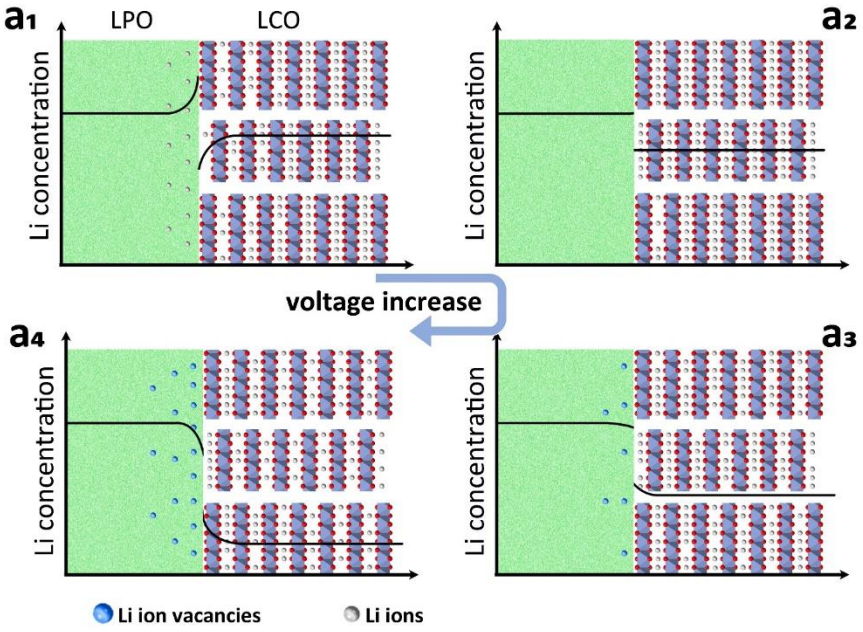

Figure 4.28 a_1 - a_4 Schematics of Li ions and Li vacancies evolution in LPO|LCO interfacial space charge layer with battery voltage increase.

By comparing the difference between experimental LPO|LCO interfacial resistance (Figure 4.7) and theoretical LPO|LCO interfacial charge transfer resistance (Figure 4.9) at different voltage we estimate $V_{no\ SCL}$. A battery voltage of 4.2 V vs Li/Li^+ corresponds to around $Li_{0.55}CoO_2$[34,35,51,54]. Based on this reference, we can calculate the Li content x in Li_xCoO_2 at different battery voltage from our charging-discharge curve (Figure 4.5a). For all different Li content x in Li_xCoO_2 we are able to calculate the LCO|LPO interfacial charge transfer

resistances in dependence of battery voltage with equation 21. The calculated LCO|LPO interfacial charge transfer resistances are shown in Table 4.2.

Table 4.2 LCO|LPO interfacial charge transfer resistance change with thin film battery voltage

Battery voltage	3.6V	3.7V	3.8V	3.85V	3.92V	4.0V	4.1V	4.2V	4.3V
Charge transfer resistance	72.79n	62.32n	54.58n	52.99n	13.19n	8.00n	6.63n	6.04n	5.41n

In our model thin film battery, physical defects and interfacial side reaction can be ignored. Thus the difference between the experimentally measured interfacial resistance and the theoretical interfacial charge transfer resistance mainly results from a space charge layer resistance K in LPO|LCO interface. This space charge resistance changes with battery voltage. We attribute different space charge resistance values K_1, K_2, …, K_9 to the space charge layer resistance at 3.6V, 3.7V, 3.8V, 3.85V, 3.92V, 4.0V, 4.1V, 4.2V and 4.3V, respectively (Table 4.3).

Table 4.3 LCO/LPO interfacial resistance change with thin film battery voltage change

Battery voltage	**LPO/LCO Interfacial resistance (Ω)**
3.6V	$305693.30 = 72.79n + k_1$
3.7V	$88000.60 = 62.32n + k_2$
3.8V	$13900.20 = 54.58n + k_3$
3.85V	$1218.01 = 52.99n + k_4$
3.92V	$427.96 = 13.19n + k_5$
4.0V	$402.91 = 8.00n + k_6$
4.1V	$442.43 = 6.63n + k_7$
4.2V	$457.04 = 6.04n + k_8$
4.3V	$508.10 = 5.41n + k_9$

The data of our SXPS, operando KPFM and operando NRA indicates Li-ion vacancies in LCO close to the LPO|LCO interface while Li ions accumulate in LPO when the battery voltage is around 2.0 V. With increasing battery voltage, the Li ions depletion decreases in LCO close to LPO|LCO interface while the number of accumulated Li ions in LPO side decreases at the same time. Since space charge layer is thought to bring additional barrier for Li ions transfer results from Li depletion layer in solid electrolyte or electrode[10,21]. Therefore, with Li ions depletion in LCO decreasing, space charge layer resistance should decrease with battery voltage increase.

We measured that the smallest interfacial resistance corresponds to a battery voltage of 4.0 V while the theoretical charge transfer resistance monotonically decreases (Figures 4.7 and 4.9). Therefore, we can conclude that space charge layer resistance increase with battery voltage increase at least battery voltage is larger than 4.0 V. Combining the space charge layer evolution, we can conclude that when battery voltage is larger than 4.0 V, space charge layer in LPO|LCO forms from Li ions depleting in LPO side while Li ions accumulating in LCO side. And the depletion (accumulation) degree in LPO (LCO) increases with battery voltage increase. In this voltage range, space charge layer resistance increase with battery voltage increase results from depletion increases in LPO side.

The above analysis proves between the battery voltage range of 2.0 V to 4.0 V, there must be a voltage that space charge layer disappears in LPO|LCO interface. And the corresponding space charge layer resistance is 0. In order to better narrow down the battery voltage where the space charge layer disappears, we first assume that a vanishing space charge layer resistance corresponds to 4.0V, 3.92V, 3.85V, 3.8V, 3.7V and 3.6V (K_6, K_5, K_4, K_3, K_2 and K_1 equals to 0 respectively). Then I calculated all the K_1 - K_9 respectively under different conditions. For example, we set 4.0 V is the voltage space charge layer disappears, then K6 is 0. From K6, we can calculate other K_1 – K_5 and K_7 – K_9. If 4.0 V is the voltage, then from K_1 to K_5, the value should be monotonically decrease. While from K_7 to K_9, the value should be monotonically increase. All the K_1 - K_9 should be larger than 0. Therefore based on the above calculation we can decide that the certain voltage should be around 3.85V or below 3.6V. For both possibility, we both can at least decide that in the voltage range of 3.85V to 4.3V, the

LPO|LCO interfacial space charge layer monotonically increasing. This means for a battery voltage larger than 3.85 V, the space charge layer at LPO|LCO interface results from Li ion depletion in LPO and Li ions accumulation in LCO. This is also consistent with our above space charge layer simulation results at battery voltage over 3.85 V (Figure 4.27).

Next, we quantitatively evaluate the role of the space charge layer for the entire interfacial resistance in a thin film battery. Below a battery voltage of 3.85 V there is no significant Li-ion charge transport. In this case, the interface resistance LCO|LPO is infinite due to the ion-blocking properties of the LCO electrode. Therefore, we only discuss the situation in the battery voltage range 3.85V - 4.3 V where Li-ions can move across LCO|LPO interface.

For LCO voltage vs. Li/Li$^+$ is G (G > 3.85V), from charge transfer resistance at LCO|LPO interface (R_{ct}) theoretical calculation we can know ratio of R_{ct} at 3.85V and G vs. Li/Li$^+$ ($K_{Rct,G}$):

$$\frac{R_{ct,stand,3.85V}\cdot n}{R_{ct,stand,G}\cdot n} = K_{Rct,G} \tag{23}$$

Where, $n = \frac{RT}{F^2 A c_{\max}[Li^+]^{0.5} k_l^0} exp[\frac{0.5(FE+a)}{RT}]$ is the constant coefficient, which may change with $c_{\max}$ - the maximum Li ions insertion concentration in LCO (more details in equation 20 and 21), and $R_{ct,stand,3.85V}$ and $R_{ct,stand,G}$ are theoretical charge transfer resistance when n =1 at 3.85V and the voltage of G vs. Li/Li$^+$ respectively.

With EIS measurements, we can compare the interfacial resistance between LCO|LPO (R_{int}) between 3.85V and G vs. Li/Li$^+$:

$$\frac{R_{int,3.85V}}{R_{int,G}} = K_{int,G} \tag{24}$$

Since interfacial resistance R_{int} includes R_{ct} and space charge layer resistance (R_{scl}), x and y are defined as the space charge layer resistance at G and 3.85V vs. Li/Li$^+$ at LCO|LPO interface respectively.

$$\frac{R_{ct,stand,3.85V}\cdot n+y}{R_{ct,stand,G}\cdot n+x} = K_{int,G} \tag{25}$$

$$y = K_{int,G}\cdot x + K_{int,G}\cdot R_{ct,stand,G}\cdot n - R_{ct,stand,3.85V}\cdot n \tag{26}$$

Based on our conclusion from KPFM and NRA results, the space charge layer resistance in LCO|LPO continuously increases with voltage in the voltage range of 3.85V – 4.3V. Therefore, y must be smaller than x. Furthermore, the x value of the intersection of y = x and the function in equation 26 is the maximum R_{scl} at LCO|LPO interface at voltage G while the x value of the intersection point between function in equation 26 and x-axis is the minimum R_{scl} at LCO|LPO interface at voltage (Figure 4.29).

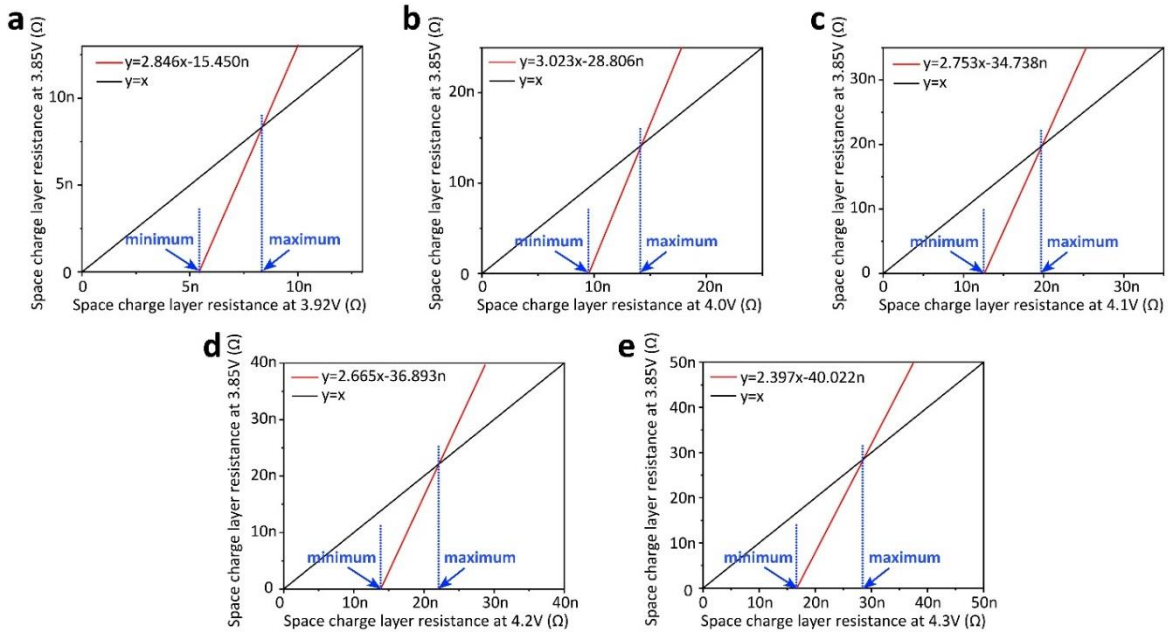

Figure 4.29 Cartesian Plots of y=x and equation S31 under different battery voltage (a) 3.92V, (b) 4.0V, (c) 4.1V, (d) 4.2V and (e) 4.3V.

Based on Figure 4.29, we can decide the maximum and minimum space charge layer resistance in LCO|LPO interface as shown in Table 4.4.

Table 4.4 The summary of maximum R_{scl} and minimum R_{scl} at LCO|LPO interface in our thin film battery under different battery voltage.

Voltage (V)	3.92	4.0	4.1	4.2	4.3
$\boldsymbol{R_{scl,max}}$ **(Ω)**	8.37n	14.24n	19.82n	22.16n	28.65n
$\boldsymbol{R_{scl,min}}$ **(Ω)**	5.43n	9.53n	12.62n	13.84n	16.70n

To calculate the exact R_{scl} in LCO|LPO interface and its proportion in the whole LCO/LPO interfacial resistance under different battery voltage, we can bring data in Table 4.4 into the following equations to calculate the exact maximum and minimum R_{scl} and their corresponding proportion in the whole interfacial resistance under different battery voltage at LCO|LPO interface:

$$Exact\ \ R_{scl,max,G} = R_{int,G}\ \cdot\ \frac{R_{scl,max}}{R_{ct,stand,G}\cdot n\ +\ R_{scl,max}} \quad (27)$$

$$Exact\ \ R_{scl,min,G} = R_{int,G}\ \cdot\ \frac{R_{scl,min}}{R_{ct,stand,G}\cdot n\ +\ R_{scl,min}} \quad (28)$$

$$Proportion\ of\ Maximum\ R_{scl,G} in\ the\ whole\ R_{int,G} = \frac{R_{scl,max}}{R_{ct,stand,G}\cdot u\ +\ R_{scl,max}}\% \quad (29)$$

$$Proportion\ of\ Minimum\ R_{scl,G} in\ the\ whole\ R_{int,G} = \frac{R_{scl,min}}{R_{ct,stand,G}\cdot u\ +\ R_{scl,max}}\% \quad (30)$$

After taking the area of thin film battery active layer into consideration (0.0924 cm^2), we can calculate the exact maximum and minimum R_{scl} under different voltage at LCO|LPO interface with standard unit of Ω cm^2 (Tables 5.5 and 5.6).

Table 4.5 Summary of the exact maximum and minimum R_{scl} under different voltage at LCO/LPO interface

Voltage (V)	3.92	4.0	4.1	4.2	4.3
$\boldsymbol{R_{scl,max}}$ **(Ω cm^2)**	13.35	22.08	29.11	31.77	38.29
$\boldsymbol{R_{scl,min}}$ **(Ω cm^2)**	9.82	18.39	25.01	27.67	33.82

Table 4.6 Summary of the proportion of maximum and minimum R_{scl} in the whole R_{int} under different voltage at LCO|LPO interface

Voltage (V)	3.92	4.0	4.1	4.2	4.3
$\boldsymbol{R_{scl,max}}$ **proportion**	33.76%	59.31%	71.21%	75.23%	81.56%
$\boldsymbol{R_{scl,min}}$ **proportion**	24.84%	49.40%	61.18%	65.52%	72.04%

The above results show that the space charge layer resistance continuously increases from around 11.5 - 15.4 Ω cm^2 at 3.92 V to around 35.5 -39.5 Ω cm^2 at 4.3 V (Figure 4.30a). In addition, we calculated the proportion of the space charge layer resistance which increases from 29.2% – 38.8% at 3.92 V to around 75.5% – 84.1% at 4.3 V (Figure 4.30b).

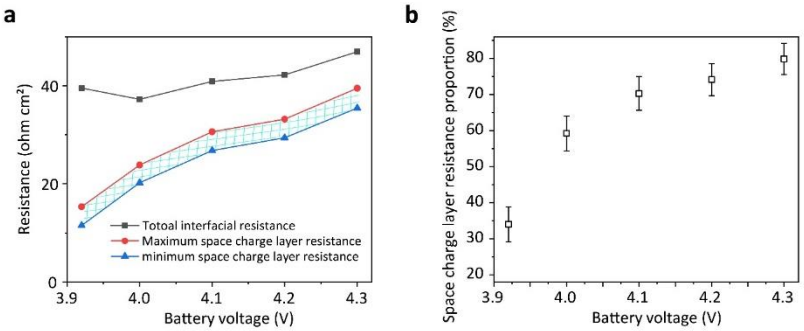

Figure 4.30 a Space charge layer resistance calculation at different voltage range. **b** Proportion of space charge layer resistance in the whole interfacial resistance at different battery voltage.

4.7 Summary and outlook

We investigated a representative all solid-state thin film battery made of Li|LPO|LCO. The thin film battery exhibits no interfacial physical defects and no chemical side reactions at interfaces. We develop that space charge layers only play a role at the LPO|LCO interface. This finding was enabled by combining different advanced characterization technologies including in-situ EIS, operando KPFM and operando NRA. The magnitude of the space charge layer changes with battery voltage. We show that the space charge layer emanates from Li ion redistribution in LPO and LCO. With increasing battery voltage, the amount of Li vacancies in LPO close to interface increases compared to bulk LPO. Simultaneously, Li ions accumulate in LCO close to interface. We quantitatively calculated the space charge layer resistance, in the voltage range where LCO does not work as an ion-blocking electrode (3.85 - 4.3 V). The space charge layer resistance reaches a maximum value 33.82 – 38.29 Ω cm^2 at a battery voltage of 4.3 V. This space charge layer resistance accounts for about 75.5% – 84.1% of the total interface resistance.

Our research is groundbreaking for the next generation ASSBs design in two ways: Firstly, we directly clarified the role of space charge layer in the whole solid-state battery. Space charge layers account for up to 80% of the entire battery internal resistance in the operating window of the battery up to 4.3 V. Therefore, we cannot ignore the role of a space charge layer role in high voltage working window any more especially for high voltage battery which even work over 5 V. Secondly but more importantly, we developed up to now non-common operando techniques, KPFM and NRA, to study solid state battery devices. The combination of both techniques allows locating and quantifying the role of space charge layers in solid state battery. In the future, except the interfaces between electrode and oxide solid electrolyte, those combined techniques can also be used to observation others kinds of solid electrolyte-based interface, such as sulfide or halide, which are not thermodynamic stable with electrode to form interlayer. The interlayer evolution and quantitatively evaluating the effect space charge layers at interlayer related interfaces can be further studied. Understanding interface is the key for helping us to develop strategies to further improve the performance of ASSBs.

4.8 Experiment

Thin film preparation and electrochemical characterization

All thin-film depositions and sample transfers were conducted without air exposure in order to not contaminate surfaces and interfaces. First, Au as current collector (200 nm thickness) was plated on a substrate by DC magnetron sputtering (argon pressure of 0.74 Pa and DC power of 20 W to the 2.54 cm (1 inch) target. Then a LCO layer (200 nm thickness) as the positive electrode was deposited on the Au layer by pulsed laser deposition (PLD) at a substrate temperature of 600 °C, an oxygen partial pressure of 0.67 Pa, a repetition rate of 10 Hz and a laser fluency of 1.2 Jcm^{-2}. Next, a layer of LPO as solid electrolyte (2.5 µm thickness) and a Li-metal as negative electrode (2 µm thickness) were subsequently deposited at room temperature. For the operando KPFM, we used a 0.2-mm-thick Al_2O_3 (0001) single crystalline substrate (Shinkosha corp.). The backside of these Al_2O_3 substrates were scratched by hand prior thin-film depositions. Such a scratch enabled a controlled fracture line for the preparation of the cross section by sample breaking. For the operando ion beam

measurements, we used a chemically etched Silicon substrate with a 1 µm-thick Si_3N_4 window (NTT advanced technology corp.). The test cell Li|LPO|Au was prepared in the same way with the only difference that a LCO layer was not deposited. We applied a positive voltage to the Li layer to dissolve Li and deposit it on the Au layer. There Li_xAu alloy forms and we obtain a cell stricter which corresponds to Li|LPO| Li_xAu.

All fabricated thin film batteries were sealed in a vacuum vessel and transferred to an Argon-filled glovebox (Mega 3, GS) where sample preparation and electrochemical characterization were conducted (H_2O< 0.1 ppm and O_2< 0.1 ppm). All electrochemical characterizations of thin film batteries, including cyclic voltammetry (CV), constant current charging-discharge and electrochemical impendence spectroscopy (EIS), were performed in the glovebox with a potentiostat (SP150, Biologic) at the room temperature.

Argon ion milling polishing

For KPFM experiments, we broke the thin film battery in two halves along the scratch, which we made in the backside of the Al_2O_3 substrate. One half of the battery was fixed in a cross-section milling holder. Next, the sealed the milling holder and transferred it into the argon ion milling chamber (IM4000, Hitachi). Then we polished the cross-section of thin film battery by argon ion milling in a pulsed mode. An acceleration voltage of 2 V was applied to generate an argon ion beam for 40 s each 2 minutes. The corresponding ion current was around 450 µA. While polishing, the rotating stage was set to a speed of 30 rpm/minute. The whole polishing process took around 24 hours. After argon ion milling, the sealed milling holder including the polished battery was transferred back to the glovebox. All further sample handling and preparation steps were done in the argon-gas filled glove box (GS, Germany).

KPFM measurements

Inside the glove box, we placed the polished battery in a homemade PEEK holder which allows us to connect the battery to a potentiostat (SP150, Biologic), while doing KPFM on the polished cross-section of the thin film battery. KPFM were performed with a scanning force microscope (MFP-3D Asylum Research, Oxford Instrument) connected to an additional Lock-in amplifier (HF2LI 50 MHz, Zurich Instrument). We used heterodyne frequency modulated

(FM) KPFM to acquire a high lateral and potential resolution[55]. For KPFM we used PtIr-coated cantilevers, which have a nominal spring constant of 2 N/m and a nominal resonance frequency of 75 kHz (SCM-PIT-V2, Bruker, USA). All KPFM measurements were done in the argon filled glovebox in order to prevent degradation of metal Li negative electrode and contamination of the polished part of the of the thin film battery. For operando KPFM test, we connected a potentiostat to the thin film battery to charge and discharge the battery to different state of charge (SOC). The Li negative electrode acts as counter electrode and is grounded. The Au acts as the current collector and is connected to the working electrode.

SEM and EDS measurements

A field-emission SEM (Hitachi U900) was used to image the morphology of the polished thin film battery cross-section. An additional energy-dispersive spectrometer (EDS) (Oxford Instruments) enabled the characterization of surface element distribution on the polished battery cross-section. In order to avoid contamination of the polished surface and chemical reactions with air, an air protection transfer box filled with argon gas was used to transfer the battery from the glovebox into the SEM chamber.

NRA measurements

We used nuclear reaction analysis (NRA) and Rutherford backscattering (RBS) techniques for operando compositional depth profiling. The depth resolution near the LPO|LCO interface is ~50 nm. Thin-film batteries were fixed in a sealed electrochemical cell in the glovebox and evacuated to a pressure < 5×10^{-4} Pa. Then the electrochemical cell was transferred to the vacuum chamber of the ion-beam line (vacuum < 1×10^{-4} Pa at the 1 MV Tandem Accelerator, Univ. Tsukuba, Tsukuba, Japan). For the measurements, we used 1 MeV H^+ beams for the NRA and RBS.

The raw NRA spectra (count *vs.* energy) were converted to a depth spectrum (counts vs. depth) using reaction cross-section. The experimental cross-section of Li is calculated from the NRA and RBS spectra of a $LiNbO_3$ single crystal. We simulated the depth spectra with Gaussian distributions allowing multiple peaks corresponding to a multilayer model. We considered the

decreasing resolution with beam penetration depth by assigning 1, 16, and 3 Gaussian distributions for Li, LPO, and LCO layer, respectively.

Synchrotron X-ray photoemission spectroscopy

The intrinsic electronic band structure of the interface between the LPO solid electrolyte and the LCO positive electrode was determined using synchrotron X-ray photoemission spectroscopy. Thin films were sealed in a vacuum suitcase and directly transferred to the synchrotron undulator beamline (BL-2A, Photon Factory, KEK, Tsukuba). The photoemission energy resolution was less than 100 meV [ref] (need check). The Fermi level was aligned using the Au 4f peak.

Space charge layer theoretical calculation

The Li ion concentration profile in LPO|LCO interfacial space charge layer was calculated based on Niek J. J. de Klerk's space charge layer model[52]. In our calculation, we assumed that 1) The evolution of a space charge layer at an interface must obey mass conservation. 2) Li ion is the only kind of charge can transfer across LPO|LCO interface. 3) All the calculations are based on equilibrium state over 3.85 V vs Li/Li^+ when Li ions can extract from LCO. (All space charge model parameters are listed in Supplementary Table 2).

LCO work function calculation

Computations were performed using density function theory (DFT) with the Perdew–Burke–Ernzerhof (PBE) functional[56], as implemented in the Vienna Ab-initio Simulation Package (VASP) [57]. The valence electron wave functions were expanded in plane-wave basis sets with a 400 eV cutoff and the projector augmented wave (PAW) method was used to describe the core-electron interactions[58]. A 14 × 5 × 1 k-point grid was sampled using the Monkhorst–Pack scheme for each computation. In addition, the effect of the dipole moment on the potential was corrected using the LDIPOL keyword in VASP.

The (100) surface of $LiCoO_2$ was created from the supercell (with $Li_{30}Co_{30}O_{60}$ as the unit cell) of the experimental crystal structure with a 15 Å vacuum slab[59]. To create the Li_xCoO_2 structures, we gradually removed the Li from the interior layer (bulk environment). All as-

created structures were fully optimized until the residual forces on the constituent atoms became less than 0.02 eV $Å^{-1}$, while keeping the lattice parameters fixed.

To calculate the work function, the electrostatic potentials $V(x, y, z)$ on a dense grid were first computed using VASP. Then $V(x, y, z)$ of the same z positions were averaged (i.e., averaged over xy planes), leading to $E(z)$. The work function can then be calculated using:

$$\mathrm{WF} = E - E_{\mathrm{F}} \tag{30}$$

where E is the averaged electrostatic potential energy in vacuum and E_{F} is the Fermi energy of the Li_xCoO_2 structure.

4.9 Statement of contribution

Rüdiger Berger, Taro Hitosugi, Chao Zhu and Shigeru Kobayashi conceived the idea. Chao Zhu carried out the Ar ion milling polishing and KPFM experiments. Shigeru Kobayashi prepared thin film battery and performed NRA measurements. Kun-Han Lin did DFT calculations. Chao Zhu and Shigeru Kobayashi performed all other data collection and analysis. Chao Zhu and Shigeru Kobayashi wrote the manuscript. Hans-Jürgen Butt, Rüdiger Berger, Taro Hitosugi and Ryota Shimizu provided expertise, electrochemical input, feedback and revised the manuscript.

4.10 Reference

1 Janek, J. & Zeier, W. G. A solid future for battery development. *Nat. Energy* **1**, 1-4 (2016).

2 Manthiram, A., Yu, X. & Wang, S. Lithium battery chemistries enabled by solid-state electrolytes. *Nat. Rev. Mater.* **2**, 1-16 (2017).

3 Kim, K. J., Balaish, M., Wadaguchi, M., Kong, L. & Rupp, J. L. Solid-state Li–metal batteries: challenges and horizons of oxide and sulfide solid electrolytes and their interfaces. *Adv. Energy Mater.* **11**, 2002689 (2021).

4 Krauskopf, T., Richter, F. H., Zeier, W. G. & Janek, J. r. Physicochemical concepts of the lithium metal anode in solid-state batteries. *Chem. Rev.* **120**, 7745-7794 (2020).

5 Xiao, Y. *et al.* Understanding interface stability in solid-state batteries. *Nat. Rev. Mater.* **5**, 105-126 (2020).

6 Banerjee, A., Wang, X., Fang, C., Wu, E. A. & Meng, Y. S. Interfaces and interphases in all-solid-state batteries with inorganic solid electrolytes. *Chem. Rev.* **120**, 6878-6933 (2020).

7 Tan, D. H., Banerjee, A., Chen, Z. & Meng, Y. S. From nanoscale interface characterization to sustainable energy storage using all-solid-state batteries. *Nat. Nanotechnol.* **15**, 170-180 (2020).

8 Lou, S. *et al.* Interface issues and challenges in all-solid-state batteries: lithium, sodium, and beyond. *Adv. Mater.* **33**, 2000721 (2021).

9 Shen, Y. *et al.* Unlocking the energy capabilities of lithium metal electrode with solid-state electrolytes. *Joule* **2**, 1674-1689 (2018).

10 Cheng, Z. *et al.* Revealing the impact of space-charge layers on the Li-ion transport in all-solid-state batteries. *Joule* **4**, 1311-1323 (2020).

11 Katzenmeier, L., Helmer, S., Braxmeier, S., Knobbe, E. & Bandarenka, A. S. Properties of the Space Charge Layers Formed in Li-Ion Conducting Glass Ceramics. *ACS Appl. Mater. Interfaces* **13**, 5853-5860 (2021).

12 Swift, M. W. & Qi, Y. First-principles prediction of potentials and space-charge layers in all-solid-state batteries. *Phys. Rev. Lett.* **122**, 167701 (2019).

13 Swift, M. W., Swift, J. W. & Qi, Y. Modeling the electrical double layer at solid-state electrochemical interfaces. *Nat. Comput. Sci.* **1**, 212-220 (2021).

14 Wang, L. *et al.* In-situ visualization of the space-charge-layer effect on interfacial lithium-ion transport in all-solid-state batteries. *Nat. Commun.* **11**, 1-9 (2020).

15 Yamamoto, K. *et al.* Dynamic visualization of the electric potential in an all-solid-state rechargeable lithium battery. *Angew. Chem.* **49**, 4414-4417 (2010).

16 Haruyama, J., Sodeyama, K., Han, L., Takada, K. & Tateyama, Y. Space–charge layer effect at interface between oxide cathode and sulfide electrolyte in all-solid-state lithium-ion battery. *Chem. Mater.* **26**, 4248-4255 (2014).

17 Maier, J. Ionic conduction in space charge regions. *Prog. Solid State Chem.* **23**, 171-263 (1995).

18 Maier, J. Physical chemistry of ionic materials: ions and electrons in solids. *John Wiley & Sons* (2004).

19 Nomura, Y. *et al.* Direct observation of a Li-ionic space-charge layer formed at an electrode/solid-electrolyte interface. *Angew. Chem.* **131**, 5346-5350 (2019).

20 Fingerle, M., Buchheit, R., Sicolo, S., Albe, K. & Hausbrand, R. Reaction and space charge layer formation at the $LiCoO_2$–LiPON interface: insights on defect formation and ion energy level alignment by a combined surface science–simulation approach. *Chem. Mater.* **29**, 7675-7685 (2017).

21 Takada, K., Ohno, T., Ohta, N., Ohnishi, T. & Tanaka, Y. Positive and negative aspects of interfaces in solid-state batteries. *ACS Energy Lett.* **3**, 98-103 (2017).

22 Haruta, M. *et al.* Negligible "negative space-charge layer effects" at oxide-electrolyte/electrode interfaces of thin-film batteries. *Nano Lett.* **15**, 1498-1502 (2015).

23 Ohnishi, T. & Takada, K. Sputter-Deposited Amorphous Li_3PO_4 Solid Electrolyte Films. *ACS Omega* **7**, 21199-21206 (2022).

24 Koerver, R. *et al.* Capacity fade in solid-state batteries: interphase formation and chemomechanical processes in nickel-rich layered oxide cathodes and lithium thiophosphate solid electrolytes. *Chem. Mater.* **29**, 5574-5582 (2017).

25 Kobayashi, S. *et al.* Drastic Reduction of the Solid Electrolyte–Electrode Interface Resistance via Annealing in Battery Form. *ACS Applied Materials & Interfaces* **14**, 2703-2710 (2022).

26 Nishio, K. *et al.* Immense Reduction in Interfacial Resistance between Sulfide Electrolyte and Positive Electrode. *ACS Applied Materials & Interfaces* **14**, 34620-34626 (2022).

27 Pan, R., Rau, D., Moryson, Y., Sann, J. & Janek, J. r. Reversible Capacity Loss of $LiCoO_2$ Thin Film Electrodes. *ACS Appl. Energy Mater.* **3**, 6065-6071 (2020).

28 Shiraki, S. *et al.* Atomically well-ordered structure at solid electrolyte and electrode interface reduces the interfacial resistance. *ACS Applied Materials & Interfaces* **10**, 41732-41737 (2018).

29 Kawasoko, H., Shiraki, S., Suzuki, T., Shimizu, R. & Hitosugi, T. Extremely low resistance of Li_3PO_4 electrolyte/$Li(Ni_{0.5}Mn_{1.5})O_4$ electrode interfaces. *ACS Appl. Mater. Interfaces* **10**, 27498-27502 (2018).

30 Schwöbel, A., Jaegermann, W. & Hausbrand, R. Interfacial energy level alignment and energy level diagrams for all-solid Li-ion cells: Impact of Li-ion transfer and double layer formation. *Solid State Ion.* **288**, 224-228 (2016).

31 Hikima, K. *et al.* Operando analysis of electronic band structure in an all-solid-state thin-film battery. *Commun. Chem.* **5**, 52 (2022).

32 Kuwata, N., Iwagami, N., Tanji, Y., Matsuda, Y. & Kawamura, J. Characterization of thin-film lithium batteries with stable thin-film Li_3PO_4 solid electrolytes fabricated by ArF excimer laser deposition. *J. Electrochem. Soc.* **157**, A521 (2010).

33 Sugiyama, I. *et al.* A nonvolatile memory device with very low power consumption based on the switching of a standard electrode potential. *APL Mater.* **5**, 046105 (2017).

34 Ohnishi, T., Mitsuishi, K. & Takada, K. In Situ X-ray Diffraction of $LiCoO_2$ in Thin-Film Batteries under High-Voltage Charging. *ACS Appl. Energy Mater.* **4**, 14372-14379 (2021).

35 Ohzuku, T. & Ueda, A. Solid-state redox reactions of $LiCoO_2$ (R3m) for 4 volt secondary lithium cells. *J. Electrochem. Soc.* **141**, 2972 (1994).

36 Yongfang, L. & Haoquing, W. Theoretical treatment of kinetics of intercalation electrode reaction. *Electrochim. Acta* **34**, 157-159 (1989).

37 Holzapfel, M. *et al.* First lithiation and charge/discharge cycles of graphite materials, investigated by electrochemical impedance spectroscopy. *J. Electrochem. Soc.* **546**, 41-50 (2003).

38 Zhuang, Q. *et al.* $LiCoO_2$ electrode/electrolyte interface of Li-ion batteries investigated by electrochemical impedance spectroscopy. *Sci. China, Ser. B: Chem.* **50**, 776-783 (2007).

39 Levi, M. & Aurbach, D. Frumkin intercalation isotherm—a tool for the description of lithium insertion into host materials: a review. *Electrochim. Acta* **45**, 167-185 (1999).

40 Levi, M. D. *et al.* Solid-state electrochemical kinetics of Li-Ion intercalation into $Li_{1-x}CoO_2$: simultaneous application of electroanalytical techniques SSCV, PITT, and EIS. *J. Electrochem. Soc.***146**, 1279 (1999).

41 Hasegawa, G. *et al.* Tracer diffusion coefficients of Li+ ions in c-axis oriented Li_xCoO_2 thin films measured by secondary ion mass spectrometry. *Phys. Chem. Chem. Phys.* **23**, 2438-2448 (2021).

42 Melitz, W., Shen, J., Kummel, A. C. & Lee, S. Kelvin probe force microscopy and its application. *Surf. Sci. Rep.* **66**, 1-27 (2011).

43 Weber, S. A. L. *et al.* How the formation of interfacial charge causes hysteresis in perovskite solar cells. *Energy Environ. Sci.* **11**, 2404-2413 (2018).

44 Zerweck, U., Loppacher, C., Otto, T., Grafström, S. & Eng, L. M. Accuracy and resolution limits of Kelvin probe force microscopy. *Phys. Rev. B* **71**, 125424 (2005).

45 Bergmann, V. W. *et al.* Real-space observation of unbalanced charge distribution inside a perovskite-sensitized solar cell. *Nat. Commun.* **5**, 1-9 (2014).

46 Masuda, H., Ishida, N., Ogata, Y., Ito, D. & Fujita, D. Internal potential mapping of charged solid-state-lithium ion batteries using in situ Kelvin probe force microscopy. *Nanoscale* **9**, 893-898 (2017).

47 Barbet, S. *et al.* Cross-talk artefacts in Kelvin probe force microscopy imaging: a comprehensive study. *J. Appl. Phys.* **115**, 144313 (2014).

48 Örnek, C., Leygraf, C. & Pan, J. On the Volta potential measured by SKPFM–fundamental and practical aspects with relevance to corrosion science. *Corros. Eng. Sci. Technol.* **54**, 185-198 (2019).

49 Fuller, E. J. *et al.* Spatially resolved potential and Li-ion distributions reveal performance-limiting regions in solid-state batteries. *ACS Energy Lett.* **6**, 3944-3951 (2021).

50 Gao, B., Jalem, R., Ma, Y. & Tateyama, Y. Li^+ transport mechanism at the heterogeneous cathode/solid electrolyte interface in an all-solid-state battery via the first-principles structure prediction scheme. *Chem. Mater.* **32**, 85-96 (2019).

51 Möller, S. *et al.* Absolute Local Quantification of Li as Function of State-of-Charge in All-Solid-State Li Batteries via 2D MeV Ion-Beam Analysis. *Batteries* **7**, 41 (2021).

52 de Klerk, N. J. & Wagemaker, M. Space-charge layers in all-solid-state batteries; important or negligible? *ACS Appl. Energy Mater.* **1**, 5609-5618 (2018).

53 Sumita, M., Tanaka, Y., Ikeda, M. & Ohno, T. Theoretical insight into charging process in a Li_3PO_4 (100)/$LiFePO_4$ (010) coherent interface system. *Solid State Ion.* **285**, 59-65 (2016).

54 Dahéron, L. *et al.* Electron transfer mechanisms upon lithium deintercalation from $LiCoO_2$ to CoO_2 investigated by XPS. *Chem. Mater.* **20**, 583-590 (2008).

55 Axt, A., Hermes, I. M., Bergmann, V. W., Tausendpfund, N. & Weber, S. A. L. Know your full potential: Quantitative Kelvin probe force microscopy on nanoscale electrical devices. *Beilstein J. Nanotechnol.* **9**, 1809-1819 (2018).

56 Perdew, J. P., Burke, K. & Ernzerhof, M. Generalized gradient approximation made simple. *Phys. Rev. Lett.* **77**, 3865 (1996).

57 Kresse, G. & Furthmüller, J. Efficient iterative schemes for ab initio total-energy calculations using a plane-wave basis set. *Phys. Rev. B* **54**, 11169 (1996).

58 Kresse, G. & Joubert, D. From ultrasoft pseudopotentials to the projector augmented-wave method. *Phys. Rev. B* **59**, 1758 (1999).

59 Lin, Q. Q. a. Li, KE Gray and JF Mitchell. *Cryst. Growth Des.* **12**, 1232-1238 (2012).

Chapter 5 Conclusion and outlook

This thesis is mainly about using advanced operando Kelvin probe force microscopy (KPFM) to study interfaces in all-solid-state batteries. These interfaces are widely recognized as one of the key factors affecting all-solid-state batteries' performance. Understanding the role of certain interfaces on Li ion transfer and electrochemical reactions can guide us to properly design and improve interfaces in all-solid-state batteries. As opposed to other technologies, operando KPFM is a non-destructive characterization technique with high spatial resolution. It provides us a chance to directly observe and evaluate interfaces' effects according to tracking measured contact potential difference (CPD) at interfaces and adjacent regions.

Before using KPFM to study batteries' internal interfaces, I first studied and clarified that the measured CPD changes with KPFM on mixed-ionic-electronic conductor (MIEC), resulting from Galvani potential changes, which was not clear until now. Because solid electrolytes in all-solid-state batteries are typical kinds of MIEC with high ionic conductivity and low electrical conductivity, this study can help us more precisely understand the role of different internal interfaces in batteries under battery working conditions.

Then I used operando KPFM combined with time-resolved electrostatic force microscopy (tr-EFM) and electron beam irradiation to provoke metallic lithium nucleation on a garnet-type based solid electrolyte $Li_{6.25}Al_{0.25}La_3Zr_2O_{12}$ (LLZO). I showed that the measured CPD drops along grain boundaries close to the negative lithium electrode under battery working conditions. That is as a result of the formation of a space charge layer at the grain boundaries, because of grain boundaries' electron trapping ability. Due to the special electron conduction properties, LLZO grain boundaries easily have higher overpotential for lithium ion reduction to form lithium dendrites. This finding tells us that improving the electron conduction properties at grain boundaries is one of the keys to prevent the penetration of lithium dendrites into the LLZO solid electrolyte.

Lastly, I also used operando KPFM combined with in-situ electrochemical impedance spectroscopy (EIS) and operando nuclear reaction analysis (NRA) to study space charge layers

in thin films of all-solid-state batteries, where metallic lithium is used as a negative electrode, Li_3PO_4 (LPO) as a solid electrolyte and $LiCoO_2$ (LCO) as a positive electrode. I find that a space charge layer only exists at the LPO|LCO interface, which changes with battery voltage. In the working window 3.0 V to 4.3 V, as voltage increases, the space charge layer in LPO|LCO evolves with more lithium depletion at the LPO side, close to the interface, while more lithium-ion accumulates at the LCO side, close to the interface. The whole width of the space charge layer is on the scale of just several nm. Furthermore, we calculate that the space charge layer has its highest resistance at 4.3 V, which is around 33.82 – 38.29 Ω cm^2 and accounts for about 75.5% – 84.1% of the total interface resistance. This study clearly and completely shows the special distribution and evolution of space charge layers in all-solid-state batteries. More importantly, the quantitative calculation of space charge layer resistance can help us better evaluate and understand the role space charge layer in all-solid-state batteries.

Generally, my studies show the potential of KPFM related technologies used to study batteries' internal interfaces. With the help of measured potential distribution in batteries by KPFM, we have the chance to study the effect of different internal interfaces in batteries. The application of KPFM in batteries promotes related research in the battery field. However, we must point out the disadvantages.

1) KPFM is the technology that only characterizes the layer at the very surface of different layers in batteries. Due to the existence of surface polarization, the surface layer is not always the same as in the bulk. Therefore, it is important to consider the difference between measured the surface layer and bulk into consideration when we analyze KPFM measurements.

2) KPFM can be used to characterize the electrical potential change of different layers in a battery. The electrical potential normally results from movement of ions or electrons. However, KPFM cannot separate electrical potential change due to electrons or ions. This often leads to misinterpretation of KPFM results. Therefore, to use KPFM correctly and effectively, combining KPFM measurements with other characterization technologies, such as classical electrochemical methods, tr-EFM, NRA and so on, is advised.

Publication list

[1] **Chao Zhu**, Till Fuchs, Stefan Weber, Felix. H. Richter, Gunnar Glaser, Franjo Weber, Hans-Jürgen Butt, Jürgen Janek and Rüdiger Berger. Understanding the evolution of lithium dendrites at $Li_{6.25}Al_{0.25}La_3Zr_2O_{12}$ grain boundaries via operando microscopy techniques (Nature Communications **14**, 1300 (2023))

[2] **Chao Zhu**, Shigeru Kobayashi, Yuki Sugisawa, Natsuko Kishi, Miho Kitamura, Koji Horiba, Hiroshi Kumigashira, Hans-Jürgen Butt, Taro Hitosugi, Rüdiger Berger. Quantification of Dynamic Space Charge Layer Evolution in All-Solid-State Batteries (submitted)

[3] Franjo Weber‡, **Chao Zhu‡**, Till Fuchs, Felix H. Richter, Jürgen Janek, Rüdiger Berger. Evaluation of the Kelvin Probe Force Microscopy Signal for Systems in Electrochemical non-Equilibrium State (in preparation) (Co-first author)

[4] Matthias Endersa, **Chao Zhu**, Maximilian Klebera, Georg Derscheida, Rüdiger Berger, Hans-Dieter Bauera, Birgit Scheppata. Effects of surface morphology changes on FTIR-ATR spectroscopy with compacted Sodium Alanate ($NaAlH_4$) during cycling (International Journal of Hydrogen Energy **48**, 709-722 (2023))

[5] Tianle Zheng‡, Bingyin Zhu‡, Jianwei Xiong‡, Xiaotang Shi, **Chao Zhu**, Shanshan Ying, Guangjiu Pan, Tonghui Xu, Hongbin Zhao, Rüdiger Berger, Ya-Jun Cheng, Yonggao Xia, Peter Müller-Buschbaum. When Audience Takes Stage: Pseudo-Localized-High-Concentration Electrolyte with Lithium Nitrate as the Only Salt for Lithium Metal Batteries (submitted)